QUANTUM MONTE CARLO STUDY OF ELECTRONIC CORRELATION EFFECTS IN SUPERCONDUCTORS

A Dissertation submitted to the

Division of Research and Advanced Studies
of the University of Cincinnati

in partial fulfillment of the
requirements for the degree of

DOCTOR OF PHILOSOPHY

in the Department of Physics
of the College of Arts and Science

1996

by

Woonki Chung

M.S., Sogang University, Seoul, Korea, 1988
B.S., Sogang University, Seoul, Korea, 1986

Committee Chair: Prof. Mark Jarrell

Abstract

We study quantum effects due to electronic correlations in two different superconducting systems. For each problem, we employ a different type of Quantum Monte Carlo (QMC) method which provides non-perturbative solutions.

First, we study the thermodynamic properties of a two-dimensional periodic array of fully frustrated quantum Josephson junctions which is a model of granular superconductors. Here we take account of the quantum effects arising from the charging energy of a superconducting grain. We use a hybrid QMC algorithm to prevent the system from getting trapped in a local energy minimum which usually occurs for a frustrated system.

For dilute magnetic alloy superconductors, we study dramatic and non-perturbative effects due to the correlations between the magnetic impurity and the superconducting host. We present a systematic study using a combination of a self-consistent QMC method, Maximum Entropy Method and a formally exact analytic continuation method.

Acknowledgments

First of all, I would like to thank my advisor, Prof. Mark Jarrell, for his continuous support, encouragement and guidance in all aspects of my study. His endless enthusiasm and distinguished insights into physics have greatly helped me to expand my academic horizons, and have always been deeply appreciated. I will fondly remember my daily meetings with Mark, where he shared his academic expertise and experience with me. I am also grateful to Mrs. Jarrell for her support and words of encouragement, especially during my difficult times.

Thanks go to Profs. Michael Ma, David Mast and Peter Suranyi for serving as members of my committee. I appreciate their helpful suggestions, constructive criticism and reading draft of the manuscript.

I am grateful to Dr. John Mikalopas for sharing his academic expertise with me during my first project. I credit much of the work in Chapter 2 of this thesis to him. He also helped me learn UNIX and FORTRAN.

I am also grateful to my previous office-mate and colleague, Hossein Akhlaghpour, for his interest, useful discussions and suggestions. He especially helped me a lot understand the Maximum Entropy Method. He also provided me many useful codes.

Prof. Jim Freericks of Georgetown University provided me his notes and critical suggestions on my research. His idea and suggestions about the formally exact analytic continuation method in Chapter 3 of this thesis were of great help, and I deeply appreciate it.

I would like to thank Profs. Bernie Goodman, Frank Pinski and Fu-Chun Zhang for their interest and encouragement throughout the course of my study. They have always helped me kindly and offered useful suggestions.

I would also like to thank David Will, computer Systems Administrator in the Physics Department. His willingness to help people, his kindness as well as his good knowledge about computer systems have always been deeply appreciated.

I would then like to express my appreciation to members of Physics Department Office, in particular Peg Frantz and Lynne McEneny. They have always been cheerful and efficient in their help with various administrative and financial procedures.

This work was generously supported by the Office of Naval Research (ONR N00014-92-J-1686 and N00014-95-1-0883) and the Ohio Supercomputing Center.

Finally, special thanks to my mother and all of my family members for their support, love, and confidence in me.

Contents

List of Figures

List of Tables

Chapter 1

Introduction

Superconductivity has always been of great interest for long time due to its remarkable properties such as zero resistivity, perfect diamagnetism, *etc.* Naturally many theoretical and experimental efforts have been made to understand the underlying physics. At present, one believes that conventional superconductors [1, 2] are well understood both theoretically and experimentally; i.e., the superconductivity is accompanied by macroscopic order parameter which arises from the coherent pairing of Landau quasiparticles with time-reversal symmetry. However, there are also interesting superconducting systems where quantum effects due to electronic correlations play an important role in the superconducting phase. Such quantum effects from the electronic correlations may give rise to unusual and complicated phenomena.

In this thesis, we study the quantum effects due to electronic correlations in two different superconducting systems using a different type of Quantum Monte Carlo (QMC) method for each problem. One problem is a model of granular superconductors, where the grain size is so small that we should take account of the quantum effects arising from the charging energy of the electrons. Another is a dilute magnetic alloy superconductor, where the correlations between the magnetic impurity and the superconducting host give rise to dramatic and non-trivial effects.

In general, it is difficult to solve such systems of electronic correlations analytically. Thus most theoretical approaches involve approximate methods. However, for instance, perturbative approaches for a given problem usually fail in some parameter regimes — in many cases physically interesting regimes. With the rapid development of the computers, QMC method has been employed and developed for many different problems, and it provides nonperturbative solutions, which are exact within controllable systematic and statistic errors. Even if there are other nonperturbative methods (e.g., Numerical Renormalization Group Method, Bethe Ansatz, *etc*) for a given problem, it is usually hard to get dynamics and thermodynamic properties. Since QMC method provides the dynamic response functions, we can more extensively compare the theoretical predictions with experimental results along with other theoretical methods. In the following sections, we use different kinds of OMC method in two superconducting systems.

In Chapter 2, we study the thermodynamic properties of a two-dimensional periodic array of fully frustrated quantum Josephson junctions. Here the problem is two-fold. Classical Josephson junction arrays are characterized by a superconducting phase difference between grains with Josephson coupling energy. When the grain size becomes small, however, the charging energy of a superconducting grain is no longer negligible compared to the Josephson energy. Thus the number of electrons transferring across the junction, which is a conjugate variable to the phase difference, must be quantum-mechanically taken account of. Meanwhile, since a frustrated system usually has many energy minima, the system can easily get trapped in a local minimum. This is especially true for a typical diffusive QMC simulation in which the field variables evolve locally. To remove this difficulty, we use a hybrid QMC algorithm [3, 4, 5] so that the field variables are allowed to evolve globally. As a result we systematically study various thermodynamic properties of the system, and discuss the controversial problem from the previous theories such as "a quantum-induced low-temperature first-order transition" [6, 7, 8, 9, 10].

In Chapter 3, we consider a dilute magnetic alloy superconductor. Here the magnetic moment on the impurity couples antiferromagnetically to conduction electrons, and breaks the time-reversal symmetry of the conduction electrons. Thus even a small amount of the magnetic impurities can destroy the superconducting state. This effect is associated with the "Kondo effect" [11], which is another important quantum effect. It occurs from the screening of the impurity magnetic moments by the conduction electrons, and the superconductivity can also quench the Kondo effect. Thus this is a non-trivial and non-perturbative problem, and it is highly desired to have an exact and systematic study. Here we present a novel method using a combination of a self-consistent QMC method [12], Maximum Entropy Method (MEM) [13], and a formally exact analytic continuation method [14]. Then we systematically study the "gap states" in the superconducting gap induced by the magnetic impurities.

Details of the hybrid QMC algorithm and the formalism necessary for the Chapter 2 are given in Appendices A and B. Also for the Chapter 3, we present a derivation of Eliashberg equations [15] and the QMC algorithm in Nambu formalism [16], and summary of the MEM in Appendices C, D and E respectively.

Chapter 2

A Systematic Hybrid Quantum Monte Carlo Study of the Fully Frustrated Quantum Josephson Junction Array

J. Mikalopas, M. Jarrell, F. J. Pinski and Woonki Chung

2.1 Introduction

Many model calculations have been performed for granular superconductors coupled by Josephson tunnel barriers. Early on, Anderson [17], Abeles [18] and Simanek [6] implied that the electrostatic charging energy and thus the capacitance associated with ultra-small metal grains could have a profound effect on the superconducting properties of the aggregate. Perhaps the most dramatic such effect was reported by Jacobs *et al.*[8, 9, 10]. A first-order transition at low temperatures was seen in their simulations of quantum Josephson junction arrays. They claim that this transition was one from the usual superconducting state to a novel zero-resistance coherent state dominated by zero point quantum fluctuations referred to this as a "quantum induced transition" (QUIT). This effect was found using diffusive Monte Carlo calculations and was indicated by a maximum in the specific heat and a non-monotonic behavior in the helicity modulus.

Here we report a series of calculations that provide evidence that the QUIT that was observed was a metastable state resulting from spatial domain boundaries which are also observed in classical arrays. We focus on the metastable states in the fully-frustrated model, rather than in the equilibrium critical behavior of the model [19, 20], since the QUIT was reported to be far more pronounced when a transverse magnetic field was applied. We did not see the QUIT and attribute the previous evidence for the QUIT to limitations of the diffusive Monte-Carlo algorithm employed in the work by Jacobs *et al.* In their algorithm, configurations were generated by making local changes to the previous configuration or by using a nonlocal diffusive update that rotated either an entire column of spins in the imaginary time direction or an entire plane of spins at a particular time-slice. Subsequent to their studies, substantial advances have been made in algorithms and computers. In our simulations, we employ a hybrid Monte-Carlo algorithm [3, 4, 5] in which the field variables are allowed to evolve *globally* under a set of Hamilton-Jacobi equations. By such a sampling procedure, the hybrid Monte-Carlo removes the strong correlations that can exist between consecutive configurations in a diffusive Monte-Carlo algorithm.

In the next section, Section 2.2, we will discuss the formalism applied, motivation, and sketch the structure of the Hybrid Monte Carlo Algorithm applied. In Section 3.5, we present our results, and in Section 2.4 we make our conclusions. Details of the Hybrid Monte Carlo Algorithm are presented in Appendix. A, and the formalism necessary for the Section 2.2.1 is detailed in Appendix. B.

2.2 Formalism and Method

Following Jacobs *et al.*, we model a granular material with ultra-small grains with a periodic array of Josephson junctions with finite capacitance. The topology of the array is taken to be a two-dimensional square lattice with periodic boundary conditions. All the Josephson junctions have an identical temperature-independent coupling constants and only the diagonal contribution of the capacitance matrix is included in the electrostatic energy. Other calculations have included off-diagonal contributions to the charging energy.[21, 22]

The corresponding Hamiltonian has the form

$$H = \sum_{\langle i,j \rangle} \epsilon_C n_{i,j}^2 + \epsilon_J \{2 - \cos(\phi_{i+1,j} - \phi_{i,j} - \psi_{i,i+1}) - \cos(\phi_{i,j+1} - \phi_{i,j} - \psi_{j,j+1})\}. \quad (2.1)$$

The sum is over the neighboring sites, indexed by an i and j, of a two-dimensional square lattice. Each $\phi_{i,j}$ is the phase of the Ginzburg-Landau superconducting order parameter associated with each grain, and $\phi_{i,j+1} - \phi_{i,j} - \psi_{j,j+1}$ is the gauge-invariant phase difference across a Josephson junction composed of nearest-neighbor grains. The $n_{i,j}$ measure the charge imbalance on a grain. The operators $\phi_{i,j}$ and $n_{i,j}$ are canonically conjugate and satisfy the commutation relations $[n_{i,j}, \phi_{i',j'}] = -\imath\delta_{i,j;i',j'}$. The Josephson coupling energy associated with each junction is ϵ_J, and ϵ_C is the electrostatic charging energy associated with each grain. We choose our unit of energy such that $\epsilon_J = 1$. The link integrals $\psi_{i,i+1}$ are proportional to the line integrals of the magnetic vector potential $\mathbf{A}$ between nearest-neighbor sites

$$\psi_{i,i+1} = (2\pi/\Phi_o) \int_i^{i+1} \mathbf{A} \cdot d\mathbf{l}, \quad (2.2)$$

where Φ_o is the fundamental quantum of flux. The uniform frustration parameter f, which identifies the number of flux quanta per plaquette, is equal to the sum around an elementary plaquette of the link integrals divided by 2π, that is $2\pi f = \sum_p \psi$. The zero applied external field and fully frustrated cases correspond to $f = 0$ and $f = 1/2$ respectively. We will restrict ourselves to the fully frustrated case, $f = 1/2$.

2.2.1 Motivation

One of the motivating factors was to study how quantum effects could modify the classical dynamics of Josephson Junction arrays. To this end, we considered a simple calculation using the the array shown on the left of Fig. 2.1. Here we have two types of superconducting grains. The larger grains are considered as classical, that is, their capacitance is so large that it may be considered infinite. These large grains alternate with smaller ones. In the small grains the charging energy is of the same order as the inter-grain Josephson coupling energy and thus this quantum effect will be important.

First, consider the action of this array when, as usual, the inter-site capacitance is neglected. We may renormalize this action, by integrating out the degrees of freedom associated with the quantum grain, and obtain a renormalized purely classical action. We note that this procedure is exact in that it does not approximate the partition function, or the thermodynamics of this system of junctions.

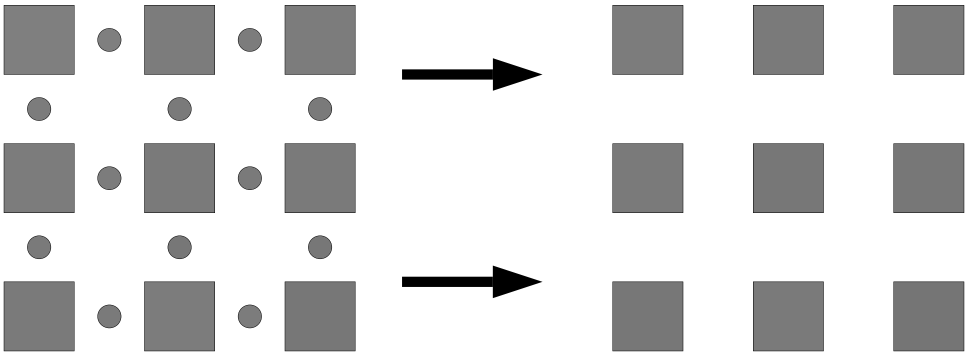

Figure 2.1: *Quasiclassical Josephson Junction Array (left) and the array after renormalization of the smaller grains (right). The smaller grains are considered quantum, in that their charging energy* $\epsilon_C = e^2/2C$ *is of the same order of magnitude as the intersite Josephson coupling* E_J*. However, the larger grains are considered classical, so that their capacitance is considered infinite. In the renormalization procedure, we integrate out the degrees of freedom associated with the smaller grains. The resulting interaction, between two remaining classical grains, is plotted in Fig. 2.2.*

To derive our renormalized classical action, we considered a system consisting of a single small quantum grain whose two nearest neighbors are large classical grains. In order to integrate out the the degrees of freedom associated with the quantum grain we consider only a part of the action and therefore out numerical task is tractable. Our numerical integration can be verified by a tedious analytical integration. Details of the renormalization procedure are presented in Appendix B.

We have calculated the renormalized classical action between two classical grains in which the intervening quantum grain has been integrated out and in Fig. 2.2 we plot this action for various values of ϵ_C. Clearly, the resulting intergrain action is well represented by the cosine function, indicating that the renormalized classical action is very similar to the usual classical action. In this case, the primary effect of the

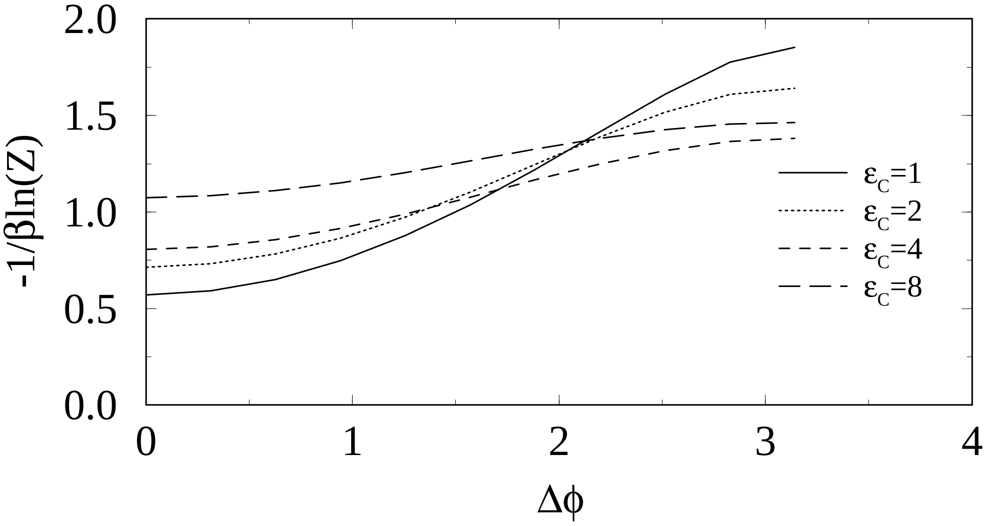

Figure 2.2: *The renormalized classical action obtained by integrating out an intervening quantum grain between two larger classical grains.*

capacitance is a reduction in the strength of the interaction between the classical grains, which is proportional to the curvature of the renormalized classical action at $\Delta\phi = 0$. As a consequence the transition temperature is reduced but the qualitative thermodynamic features are unmodified. Thus, to see if the capacitance can qualitatively change the thermodynamic properties of the system one must understand the collective excitations of the system, which only a simulation of a fully quantum lattice model can expose.

2.2.2 Simulation

The thermodynamic properties associated with H, Eq. 1, are calculated by using a quantum Monte-Carlo algorithm. The formalism is based on Feynman's imaginary-time representation of the corresponding quantum partition function, $Z = \int D\phi e^{-S\{\phi\}}$. $S\{\phi\}$ is the action associated with the scalar field ϕ,

$$
\begin{aligned}
S\{\phi\} = \sum_{i,j} \int_0^\beta d\tau \quad & [\frac{1}{\epsilon_C}\left(\frac{\partial \phi_{i,j}(\tau)}{\partial \tau}\right)^2 \\
& + \epsilon_J\{2 \quad - \cos(\phi_{i+1,j}(\tau) - \phi_{i,j}(\tau) - \psi_{i,i+1}(\tau)) \\
& \qquad\qquad - \cos(\phi_{i,j+1}(\tau) - \phi_{i,j}(\tau) - \psi_{j,j+1}(\tau))\}],
\end{aligned} \tag{2.3}
$$

where τ is the imaginary-time variable.

In a conventional Monte-Carlo procedure, the expectation value of a physical quantity $\langle A \rangle$ is evaluated by generating a sequence of configurations of the scalar fields $\{\phi_m\}$, with probability $P\{\phi_m\}$. In the Metropolis procedure, the most natural choice for the probability is made, that is $P\{\phi_m\} \propto e^{-S\{\phi_m\}}$. With this choice the computation of the expectation values reduces to the arithmetic average $\langle A \rangle \approx (1/M)\sum_{m=1}^{M} A\{\phi_m\}$. As commonly employed, the sampling of fields $\{\phi_m\}$ is diffusive. New configurations are usually generated by proposing only local, random changes to the field variables of the present configuration. The proposed configuration $\{\phi'_m\}$ is then accepted or rejected with probability $minimum(1, e^{\delta S})$ where $\delta S \equiv S\{\phi'_m\} - S\{\phi_m\}$. Strong correlations can exist between consecutive configurations of the field variables in a diffusive Monte-Carlo algorithm. For example, the sampling can become trapped in the vicinity of a local minimum of the action and therefore confine the sampling to a overly-limited region of phase space.

The hybrid Monte-Carlo method[3, 4] was developed to alleviate this problem[5] while retaining the property of detailed balance. This method is described in detail in App. A, and so will just be sketched here. In the hybrid method, a fictitious-momentum π is assigned to each of the variables ϕ. The dynamics of this pseudo-system are described by the pseudo-Hamiltonian, $H_p\{\pi(t), \phi(t)\} = \pi^2(t)/2 + S\{\phi(t)\}$, and the corresponding Hamilton-Jacobi equations of motion. A pseudo-partition function, $Z_p = \int D\pi \int D\phi e^{-\beta H_p\{\pi(t),\phi(t)\}}$, is associated with this pseudo-Hamiltonian. Because the integrand for each of the fictitious-momenta is Gaussian, the integral over these fictitious-momenta is easily performed to yield $Z_p = (2\pi\mu)^{(V/2)} Z$. Since the pseudo-partition function differs from the true partition function only by a multiplicative constant, the expectation values of the physical observables will be identical for both the true and pseudo-system.

The Hamilton-Jacobi equations of motion of the pseudo-Hamiltonian are evolved for a pseudo-time $t = N_t \Delta_t$ to generate a new configuration of the field variables. The resulting configuration is then accepted or rejected with a Monte Carlo step. The final configuration is often essentially independent of the initial configuration, hence the hybrid algorithm is more efficient than standard Monte Carlo algorithms. Our simulations were performed primarily on a CRAY Y/EL computer, and utilized approximately 350 hours of central processor (CPU) time, which is equivalent to about 60 hours of CRAY Y-MP CPU time. For these results we used 32 bins, each of 10^4 Monte-Carlo steps, for each temperature. We disregarded the first two bins. Typically $N_t \approx 10$. The error bars are determined from the standard deviation of the measurements over the bins divided by the square-root of the number of bins minus one.

2.2.3 Measurements

We measured several quantities to learn about the superconductivity of this system. We regard the helicity modulus Υ as the most important since it directly proportional to the superfluid density; and measures the response of the array to a long-wavelength twist along a spatial direction. In our simulations, the twist is taken along the x axis and the Landau gauge $\mathbf{A} = Bx\hat{\mathbf{y}}$ is chosen for the vector potential. The B is the applied external magnetic field. The discretized expression for the helicity modulus[10] is

$$\begin{aligned}\Upsilon = \frac{1}{N^2 N_\tau} \quad & [\langle \sum_{i,j,n} \cos(\phi_{i+1,j,n} - \phi_{i,j,n}) \rangle \\ & - \Delta_\tau \epsilon_J \{ \langle [\sum_{i,j,n} \sin(\phi_{i+1,j,n} - \phi_{i,j,n})]^2 \rangle \\ & + \langle \sum_{i,j,n} \sin(\phi_{i+1,j,n} - \phi_{i,j,n}) \rangle^2 \}] \,. \qquad (2.4)\end{aligned}$$

We also calculated the internal energy per site, $E = -\partial(\ln Z)/\partial\beta$. The discretized expression for the internal energy per site[10] is [24]

$$
\begin{aligned}
E = \frac{1}{2\Delta_\tau} + \frac{1}{N^2 N_\tau} \quad [\quad & \epsilon_J \langle \textstyle\sum_{i,j,n} \{2 \quad - \cos(\phi_{i+1,j,n} - \phi_{i,j,n}) \\
& \qquad\qquad\qquad - \cos(\phi_{i,j+1,n} - \phi_{i,j,n})\}\rangle] \\
& - \frac{1}{\Delta_\tau^2 \epsilon_C} \langle \sum_{i,j,n} \{1 - \cos(\phi_{i,j,n+1} - \phi_{i,j,n})\}\rangle].
\end{aligned}
\tag{2.5}
$$

In order to learn about the transport in the array, we measured both the current-current susceptibility in the x-direction, $\Lambda_{xx}(\mathbf{q}, i\omega_n)$, as well as the plaquette-current-current susceptibility, $\chi(\mathbf{q}, \mathbf{T})$. The sine of the gauge-invariant phase difference across a Josephson junction is proportional to a supercurrent flowing through the junction. Thus, $\Lambda_{xx}(\mathbf{q}, \tau)$ may be written as a function of the gauge-invariant current travelling across a junction in the x-direction

$$
J_{x,ij} = \sin(\phi_{i+1,j}(\tau) - \phi_{i,j}(\tau) - \psi_{i,i+1}), \tag{2.6}
$$

resulting in

$$
\begin{aligned}
\Lambda_{xx}(\mathbf{q}, i\omega_n) = & \frac{T}{N} \sum_{i,j;i',j'} \exp[\iota \mathbf{q} \cdot (\mathbf{R}_{i,j} - \mathbf{R}_{i',j'})] \\
& \times \int_0^\beta d\tau \int_0^\beta d\tau' (\langle J_{x,i,j}(\tau) J_{x,i',j'}(\tau + \tau')\rangle - \langle J_{x,i,j}(\tau)\rangle\langle J_{x,i',j'}(\tau')\rangle) e^{i\omega_n \tau}.
\end{aligned}
\tag{2.7}
$$

The plaquette-current-current susceptibility, $\chi(\mathbf{q},\mathbf{T})$ may be written as a function of the gauge-invariant current flowing around a plaquette, $\Theta_{i,j}(\tau)$,

$$\begin{aligned}\Theta_{i,j}(\tau) &= \sin(\phi_{i+1,j}(\tau)-\phi_{i,j}(\tau)-\psi_{i,i+1})\\ &+\sin(\phi_{i+1,j+1}(\tau)-\phi_{i+1,j}(\tau)-\psi_{j,j+1})\\ &+\sin(\phi_{i,j+1}(\tau)-\phi_{i+1,j+1}(\tau)-\psi_{i+1,i})\\ &+\sin(\phi_{i,j}(\tau)-\phi_{i,j+1}(\tau)-\psi_{j+1,j}).\end{aligned} \tag{2.8}$$

Thus, $\Theta_{i,j}(\tau)$ is proportional to the supercurrent flowing around the nearest-neighbor plaquette of junctions with lower-left corner i,j. The plaquette-current susceptibility, is then

$$\begin{aligned}\chi(\mathbf{q},\mathbf{T}) = \frac{\mathbf{T}}{\mathbf{N^2}}\sum_{\mathbf{i,j;i',j'}}\exp[\iota\mathbf{q}\cdot(\mathbf{R_{i,j}}-\mathbf{R_{i',j'}})]\\ \times\int_0^\beta d\tau\int_0^\beta d\tau'(\langle\Theta_{i,j}(\tau)\Theta_{i',j'}(\tau+\tau')\rangle-\langle\Theta_{i,j}(\tau)\rangle\langle\Theta_{i',j'}(\tau')\rangle)\,.\end{aligned} \tag{2.9}$$

2.3 Results

2.3.1 Thermodynamics

First, we summarize some of our results concerning the QUIT reported[8, 9, 10] by Jacobs *et al.* Consider one of their simulations on an $N\times N\times N_\tau$ lattice with

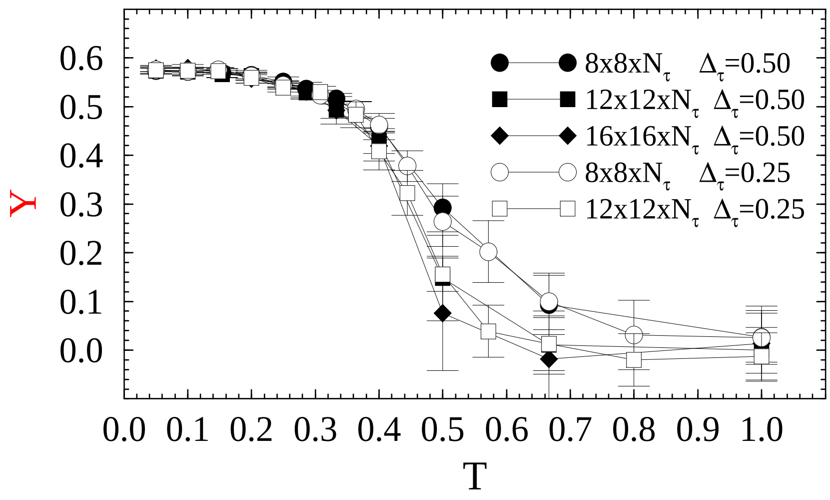

Figure 2.3: *The helicity modulus, Υ, as a function of T for $f = 1/2$ and $\epsilon_C = 0.3$ for three spatial lattice sizes ($N = 8$, 12, 16) and two values of Δ_τ. Not evident in Υ is a discontinuity, at $T < T_c \approx 0.45$, that would indicate a phase transition at low temperatures from the usual superconducting state.*

$N = 8$ and $N_\tau = 30$ with $\epsilon_J = 1.0$, $\epsilon_C = 0.3$. Their evidence for the QUIT was a discontinuity in the helicity modulus, $\Delta\Upsilon$, typical of a first-order phase transition. Unlike a reentrant transition, where $\Upsilon \to 0$ as $T \to 0$, the value of the helicity modulus Υ had a finite value as $T \to 0$. The discontinuity in the helicity modulus, $\Delta\Upsilon$, was far more pronounced for the fully frustrated system ($f = 1/2$) than for the unfrustrated system ($f = 0$). For $f = 0$, they found $\Delta\Upsilon \approx 0.03$ at $T \approx 0.03$, and for $f = 1/2$, $\Delta\Upsilon \approx 0.15$ at $T \approx 0.15$. Thus, to keep our calculations manageable we concentrated entirely on the system with $f = 1/2$.

Our principal result is shown in Fig. 2.3, where we plot the helicity modulus Υ for different system sizes and values of $\Delta\tau$. To facilitate comparison, we chose the most commonly used parameters in Jacobs *et al.* We find that the maximum slope

$\frac{d\Upsilon}{dT}$ increases with system size, as expected for a superconducting transition. We estimate the superconducting transition temperature, $T_c \approx 0.45$, in agreement with [6]. Not evident in Υ is any discontinuity that would indicate a phase transition at low temperatures from the usual superconducting state. In particular for $T < 0.15$, where the QUIT was previously reported, Υ is smooth. We show, in Fig. 2.4, the computed values for the internal energy E for the same sets of parameters. Again, this function is smooth; not evident is a discontinuity that would indicate a phase transition at low temperatures from the usual superconducting state.

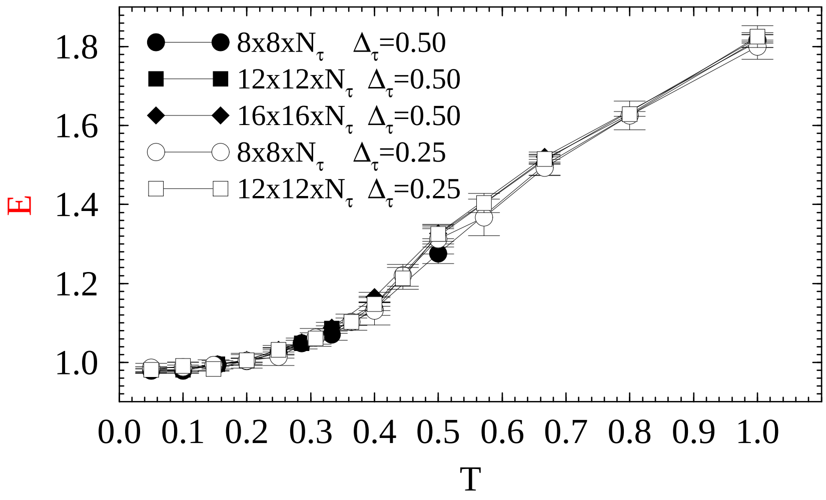

Figure 2.4: *Internal Energy vs. T when $\epsilon_C = 0.3$ and $f = 1/2$.*

To learn about the ground-state properties of the systems and to search for the possibility of other energy scales which might emerge as $T \to 0$, we performed the current-extrapolation procedure of Scalapino, White and Zhang[25]. This method sets a criteria to determine if the ground state of a system is a metal, insulator or superconductor, by looking at the asymptotic form of the current-current susceptibility in the x-direction, $\Lambda_{xx}(\mathbf{q}, i\omega_n)$. Specifically, the superfluid density, D_s is given by

$$\frac{D_s}{e^2\pi} = \langle -k_x \rangle - \Lambda_{xx}(q_x = 0, q_y \to 0, i\omega_n = 0)\,, \tag{2.10}$$

and the Drude weight, D, is given by

$$\frac{D}{e^2\pi} = \langle -k_x \rangle - \Lambda_{xx}(\mathbf{q} = 0, i\omega_n \to 0)\,. \tag{2.11}$$

Here, $\langle -k_x \rangle$ is the kinetic energy per site, divided by the number of lattice dimensions. The results of the extrapolations, $i\omega_n \to 0$ and $q_y \to 0$ are shown in Figs. 5a and 5b, respectively Clearly, both D and D_s are finite, indicating that the criteria for a superfluid ground state has been met.

Finally, to search for any possible reentrant transition which may exist for larger values of ϵ_C, we performed several addition simulations. As shown in Fig. 2.6, where the helicity modulus from these simulations is plotted, increasing ϵ_C does reduce the transition temperature. Consistent with the results shown in Fig. 2.5b, for the superfluid density, we find that the transition vanishes for $\epsilon_C/\epsilon_J = 1$. However we did not find any indication of re-entrance, or a discontinuity, for any value of ϵ_C that we simulated.

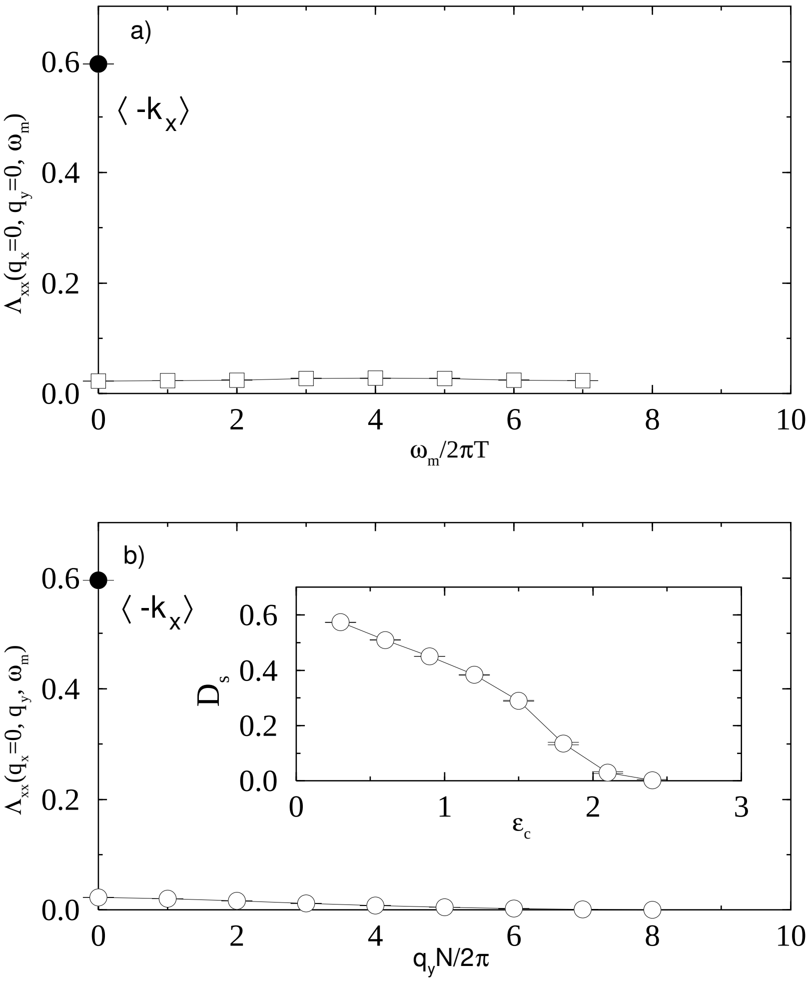

Figure 2.5: *Extrapolation of the current-current susceptibility in the x-direction, $\Lambda_{xx}(\mathbf{q}, i\omega_n)$ when $\epsilon_C = 0.3$, $\beta = 30$ and $\Delta\tau = 0.5$ for an 8×8 lattice. In both (a) and (b), the filled symbols represents $\rangle - k_x\langle$, the kinetic energy per site divided by the lattice dimensionality. As shown in (a), the Drude weight, given by $\frac{D}{e^2\pi} = \langle -k_x\rangle - \Lambda_{xx}(\mathbf{q} = 0, i\omega_n \to 0)$, is finite. As shown in (b), the superfluid density $\frac{D_s}{e^2\pi} = \langle -k_x\rangle - \Lambda_{xx}(q_x = 0, q_y \to 0, i\omega_n = 0)$ is also finite. Thus, we conclude that the ground state of this quantum Josephson Junction array is a superfluid. The inset to (b) shows the evolution of the superfluid density as a function of ϵ_C.*

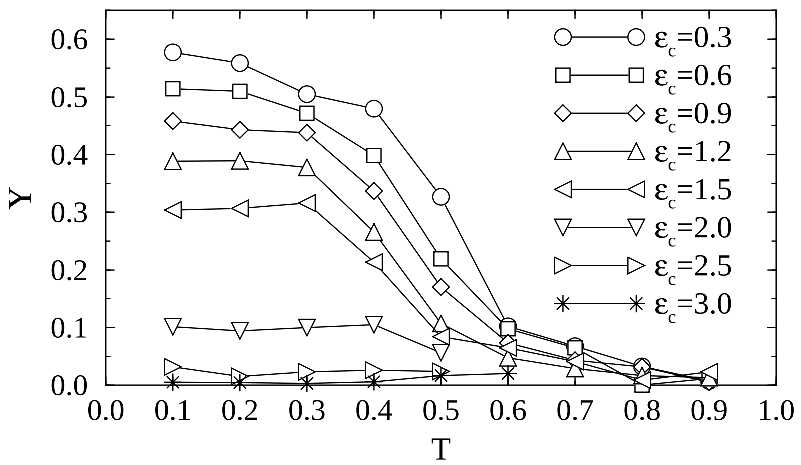

Figure 2.6: *The helicity modulus, Υ, as a function of T for $f = 1/2$, $N = 8$ and $\Delta_{tau} = 0.25$ and various values of ϵ_C. Not evident in Υ is a discontinuity, at $T < T_c$, that would indicate a phase transition at low temperatures from the usual superconducting state.*

2.3.2 Spatial Phase Boundaries in the Current Flow

Thus, we believe that the discontinuity in the helicity modulus and internal energy found by Jacobs *et al.* was caused by metastable states that appear very long lived with diffusive Monte Carlo algorithms rather than any possible first order jump to another superfluid state, or the re-entrance of the normal state. The discontinuities found were due to simulations becoming trapped in a local minimum of the action $S\{\phi\}$. We determined that these local minimum correspond to metastable configurations that have spatial domain boundaries and are also observed in classical arrays. A diffusive Monte-Carlo algorithm does not readily accommodate the coherent change of phases needed to evolve away from such a minimum in an efficient manner.

To determine the origins of the QUIT metastability, we set $\epsilon_C = 0$ and investigated the fully-frustrated (f=1/2) two-dimensional classical model. Here also, we encountered metastable configurations. Contributions from these metastable configurations lead to a decrease in the helicity modulus. If the simulation remains trapped in these states, then the helicity modulus would show a fictitious decrease. In a properly ergodic simulation, these metastable configurations are seldomly sampled since they correspond to a relatively large excitation energy.

One of these metastable configurations is shown in Fig. 2.7 on the right, whereas the appropriate classical ground state is shown on the left. Here the black (white) squares correspond to a clockwise (counter-clockwise) current flowing around the plaquette. The magnitude of the plaquette current $\Theta_{i,j}$, is indicated by the greyscale. The ground state is a black-white chessboard pattern. Comparing the two results, it is clear that the metastable configuration contains domain boundaries characterized by the exchange of the black and white sublattices. In this example, the domain boundaries are separated by four lattice spacings using a diffusive algorithm, a simulation will not readily eliminate such extended defects since many sites are involved.

To determine if similar metastable configurations exist in the quantum model, we considered one of the configurations characteristic of the proposed QUIT state from the original work of Jacobs *et al.* For this configuration, we found domain boundaries in the spatial plane for each time slice similar to that found in the classical simulation.

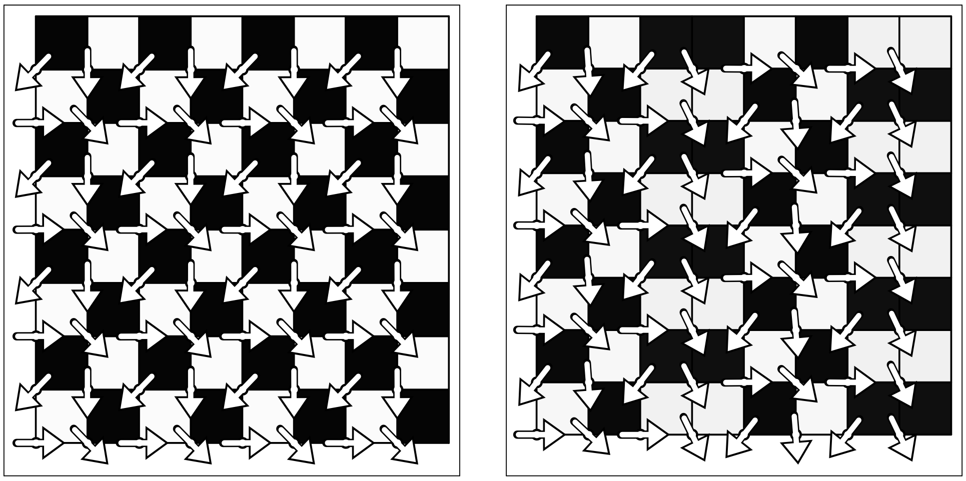

Figure 2.7: *A low-temperature highly probable equilibrium (left) and a metastable (right) configuration of the fully frustrated ($f = 1/2$) classical two-dimensional Josephson Junction array. Shown are the $\phi_{i,j}$ fields and the density plot of the gauge-invariant plaquette current, $\Theta_{i,j}$. Note the periodic boundary conditions, and the two vertical domain boundaries in the right figure.*

This is illustrated in Fig. 2.8, where we present two imaginary-time-averaged spatial configurations. The right one is representative of the QUIT state. The left of a low-temperature highly probable (LTHP) configuration, which is characterized by small fluctuations of a ground-state configuration.

In a LTHP configuration, we find the order of the currents in the spatial planes for each time slice τ to be very similar to that in the ground state of the classical two-dimensional Josephson Junction array. Thus the QUIT state is characterized by the existence of extended defects similar to those found in the classical system.

If we started with a configuration obtained from Jacobs *et al.*, that was representative of the QUIT state, then our simulations evolved into the usual superconducting

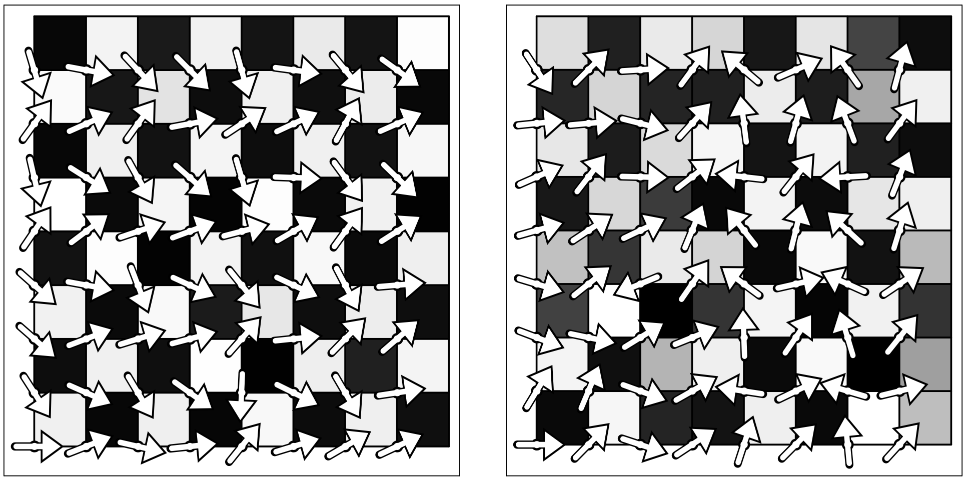

Figure 2.8: *A representative configuration at* $T = 0.12$ *(left) and the QUIT (right) configuration (from Jacobs et al. simulations) for the fully frustrated* ($f = 1/2$) *quantum two-dimensional JJA. The* τ *averaged* ϕ *variables are displayed on top of the density plot of the* τ *averaged gauge-invariant quantity* $\Theta_{i,j}(\tau)$*. Note the periodic boundary conditions.*

state. We found that our simulations became trapped in various local minima only when the path through phase space was short, i.e., either the number of pseudo-time steps N_t or the the total number of Monte-Carlo steps were small. The QUIT state was never robust with respect to an increase in the number of pseudo-time steps N_t, or an increase in the total number of Monte-Carlo steps. Simulations were also performed where the N_t and the Δ_t were chosen randomly from within finite bounds. These also did not get trapped in the QUIT configuration.

Of course, the thermodynamic properties of the system are not characterized by a few configurations such as those discussed above. Therefore, to gain quantitative insight into the effect of these configurations on the thermodynamic properties, we investigated the average plaquette-current susceptibility as shown in Fig. 2.9. Here the different peaks correspond to predominance of certain configurations. For example, the largest peak at the center of the graph corresponds to an ordering in the chessboard pattern illustrated in Fig. 2.8 (left). As we increase the system size (not shown), this peak appears to scale with system size, perhaps indicating an Ising-like transition [19, 20]. These results show that in the spatial plane, the ordering of the currents (or phases) is similar to the classical array. The plaquette-current susceptibility peaks at roughly the transition temperature T_c, for each system size simulated. The two closest secondary peaks correspond to the metastable configurations similar to that pictured in Fig. 2.8 (right), and the counterpart of this configuration rotated by $\pi/2$. Unlike the central peak, these do not scale with the system size, and hence are not indicators of low temperature order. The presence of several peaks reinforces our claim that the hybrid Monte-Carlo algorithm samples large, well-separated, regions of phase space.

2.4 Conclusion

We presented results from a quantum Monte-Carlo simulation of a two-dimensional periodic array of ultra-small fully frustrated Josephson junctions. The model includes both the Josephson energy due to the weak coupling of the grains and the electrostatic energy due to the charging of the grains. In our simulations, we employ a hybrid

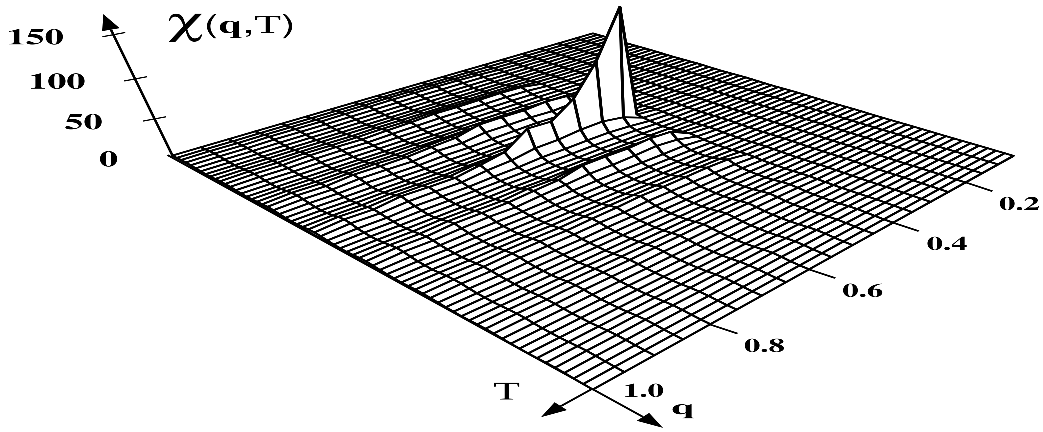

Figure 2.9: *The average plaquette current susceptibility (defined by Eq. (10)) for* $\epsilon_C = 0.3$*,* $f = 1/2$*,* $N = 8$ *and* $\Delta_\tau = 0.5$*. For these parameters, the critical transition is* $T_c \approx 0.45$*.The* $\mathbf{q}$*-vector corresponds to sequential horizontal sections of the Brillouin zone, centered at* $\mathbf{k} = (\mathbf{0}, \mathbf{0})$*. That is, the* q *is determined by sweeping* q_x *and* q_x *from* 0 *to* 2π*, with* q_x *swept faster. The dominant* $\chi(\mathbf{q}, \mathbf{T})$ *has* $\mathbf{q} = (\pi, \pi)$ *corresponding to the emergence of the chessboard pattern shown in Fig. 2.8(left); whereas, the smaller adjacent peaks correspond to the QUIT configuration Fig. 2.8(right)*

Monte-Carlo algorithm which eliminates most of the correlation between consecutive configurations of the field variables.

We do not find a previously reported first-order phase transition at low temperatures. Our results indicate that the behavior of these arrays is qualitatively similar to that of classical arrays. The quantum effects modify features but do not introduce additional phenomena. In particular, we find a variety of metastable configurations corresponding to spatial domain boundaries that are also present in classical arrays. We attribute the misidentification of the QUIT in previous work to the simulation becoming trapped in metastable states near local minima of the action $S\{\phi\}$. We cannot rule out the possibility that a QUIT occurs at lower temperatures than those simulated by us. However, we conclude that if there is a QUIT, it occurs at a very low temperature ($T_{QUIT} < 0.05\epsilon_J$, when $\epsilon_C = 0.3$). Another possibility is that the QUIT state has a correlation length much larger than the lattice sizes studied here or by Jacobs *et al*, and would only be observed for much larger arrays. Another possibility is that the QUIT could occur for a more realistic model which included off-diagonal contributions to the capacitance. Finally, the metastable configurations found by Jacobs *et al*, and identified here may be relevant to some real systems. Since, as we have shown, these metastable configurations result from spatial (not temporal) features, they therefore may be stabilized by using experimental procedures such as lattice defects.

We would like to acknowledge useful conversations with J. V. José, D. Stroud and P. Suranyi. We would especially like to thank J. E. Gubernatis for helpful conversations concerning the hybrid method and the authors of reference [10] for supplying the QUIT configuration. This work was supported by NSF (ASC-9109001) and ONR (N00014-92-J-1686). We also acknowledge the use of computing resources provided by the Ohio Supercomputer Center.

Chapter 3

Gap States in Dilute Magnetic Alloy Superconductors

Woonki Chung and Mark Jarrell

3.1 Introduction

According to Anderson's theorem, charge impurities do not have a significant effect, but magnetic impurities can have a dramatic effect, on the properties of the conventional superconductors. The reason is that the nonmagnetic charge impurities simply move the Fermi energy of the host, but the magnetic impurities can break the time-reversal symmetry of the coherent pairing of the conduction electrons. Since the superconducting state, characterized by a transition temperature T_{c0}, is formed by the coherent pairing of electrons with time-reversal symmetry, even a small amount of magnetic impurities can break the pairs and form states within the superconducting gap. Here the pair-breaking is associated with the *Kondo effect* characterized by a Kondo temperature T_0.

The superconductivity can also quench the Kondo effect. Therefore the problem of magnetic impurities in superconductors involves non-trivial and non-perturbative competition of two distinct physical phenomena; i.e., Kondo effect *vs.* superconductivity (or T_0 *vs.* T_{c0}). In this thesis, we present a systematic study for the problem using a combination of a self-consistent Quantum Monte Carlo (QMC) method [12], Maximum Entropy Method (MEM) [13], and a formally exact analytic continuation method [14].

We briefly review the Kondo effect and the superconductivity in the following. In Section 3.2, we summarize the previous experimental and theoretical results. In

Sections 3.3 and 3.4, the model and formalism we used for the problem are discussed including a formally exact analytic continuation method [13]. In Section 3.5 we present our results. In Appendices C, D and E, we also provide a derivation of Eliashberg [15] equations and the QMC algorithm in Nambu [16] formalism, and summary of the MEM, which are necessary for this problem.

3.1.1 Kondo Dilute Magnetic Alloy

Experimentally it has been observed that magnetic impurities in metals cause anomalous behavior in the transport properties. One example is the observation of a resistance minimum at finite temperature. In metals, the resistivity due to phonons monotonically decreases with temperature and vanishes at low temperature, whereas the resistivity from nonmagnetic impurity scattering is independent of temperature. The experimental results [26] for the resistivity $\rho(T)$ of various Mo-Nb alloys containing Fe impurity are shown in Fig. 3.1. Comparing the minimum value of the resistivity in Fig. 3.1 with the corresponding magnetic moments of Fe in Fig. 3.2 [27], one can clearly see the correlation between the resistance minimum anomaly and the magnetic impurities.

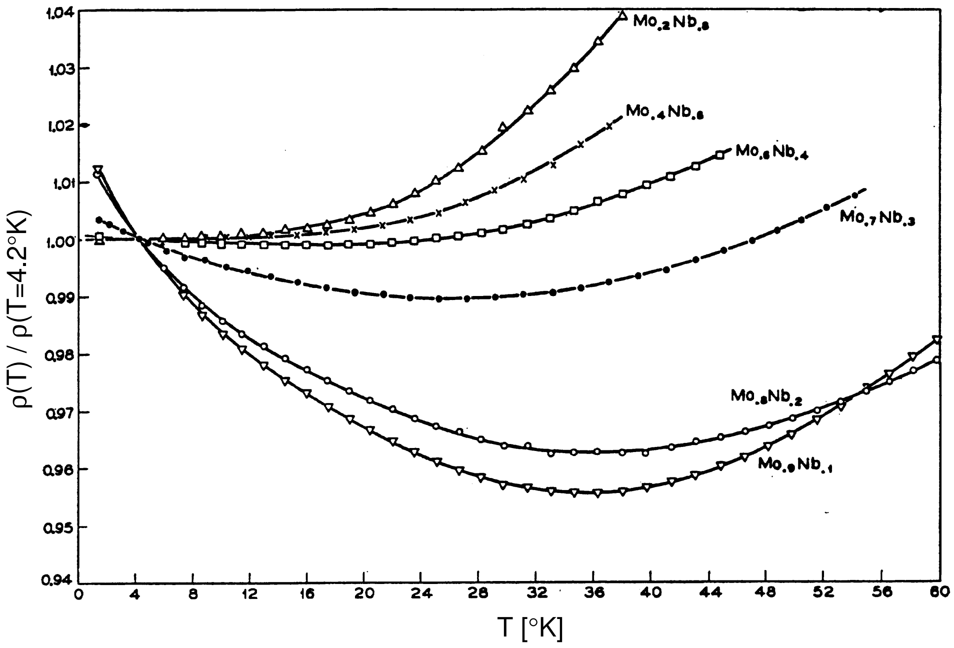

Figure 3.1: *Resistivity ρ vs. temperature T for various Mo-Nb alloys containing 1% Fe [26]. ρ is normalized at $T = 4.2\,^\circ K$.*

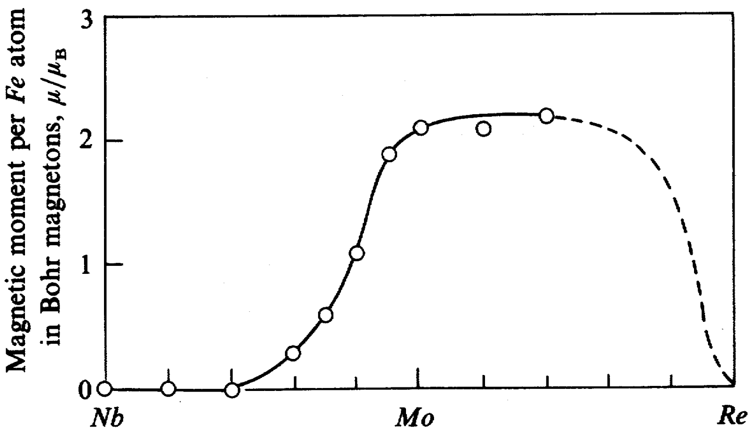

Figure 3.2: *Magnetic moment μ of Fe in various Mo-Nb and Mo-Re alloys as a function of alloy composition [27].*

Kondo Model Kondo [28] explained the resistance minimum using third order perturbation theory in the exchange interaction J based on the following Hamiltonian:

$$H = \sum_{\vec{k},\sigma} \epsilon_{\vec{k}} c^{\dagger}_{\vec{k},\sigma} c_{\vec{k},\sigma} - J \vec{s} \bullet \vec{S} \,, \tag{3.1}$$

where $c^{\dagger}_{\vec{k},\sigma}$ ($c_{\vec{k},\sigma}$) is a creation (annihilation) operator for a conduction electron in a continuum momentum space $\vec{k}$ with energy $\epsilon_{\vec{k}}$ and spin σ, $\vec{S}$ is the local spin operator, and $\vec{s}$ is the conduction electron spin operator. Here the relevant physics is associated with the spin-flip terms in which the spins of the conduction and localized electron flip each other; i.e., the corresponding spin-flip part of the Hamiltonian has the form

$$H_{spin-flip} = J \sum_{\vec{k},\vec{k}'} \left[c^{\dagger}_{\vec{k},\uparrow} c_{\vec{k}',\downarrow} S^{(-)} + c^{\dagger}_{\vec{k},\downarrow} c_{\vec{k}',\uparrow} S^{(+)} \right] \,, \tag{3.2}$$

where $S^{(\pm)}$ raise or lower the local spin. Third order perturbation of this interaction gives a $\ln T$ contribution to the resistivity, thus it explains the observed resistance minimum. The $\ln T$ term in this approach, however, diverges as $T \to 0$. In Fig. 3.3 the experimental results [29] for Ce impurities in LaB_6 show that the resistivity eventually saturates as $T \to 0$.

Summing the leading order logarithmic terms as a extension of the perturbation approach [30], the result leads to a divergence at a finite temperature T_K, so called

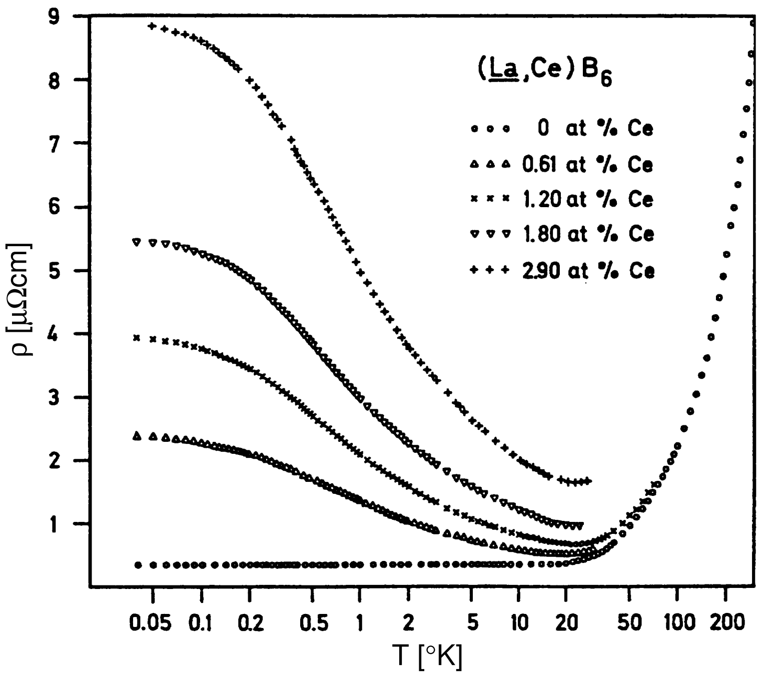

Figure 3.3: *Resistivity of* LaB_6 *and* $(\underline{La}, Ce)B_6$ *[29].*

Kondo temperature defined by

$$T_K \approx D \exp\left(-\frac{1}{2|J|N_0}\right), \tag{3.3}$$

where D is the electronic bandwidth and N_0 is the electronic density of states at the Fermi energy. These perturbation theories are correct at *high temperature* ($T \gg T_K$), but they clearly fail when extended to the region $T \leq T_K$.

To address this problem, a self-consistent approach in the high-temperature perturbation theory was introduced by Nagaoka [31] and Suhl [32], whose solutions are no longer singular at $T = T_K$ and hence can be extended down to $T = 0$. Solving the

Nagaoka-Suhl equations, Hamann [33] obtained an expression for the resistivity:

$$\rho(T) = \frac{\rho(T=0)}{2}\left[1 - \frac{\ln(T/T_K)}{\left\{[\ln(T/T_K)]^2 + \pi^2 S(S+1)\right\}^2}\right] . \tag{3.4}$$

Although this provides qualitative description of the resistivity for all temperatures, it is quantitatively correct only at high temperature ($T \gg T_K$).

The reason for this failure is that when $T \ll T_K$ the impurity state is very different from when $T \gg T_K$. At low temperature ($T \ll T_K$), the local spin becomes frozen out forming a collective state (singlet for $S = \frac{1}{2}$) with the conduction band. It is associated with a binding energy ($\sim T_K$) which should be overcome for a spin-flip process. Thus the Kondo effect saturates as $T \to 0$. Since Yosida [34] first considered this collective state, the Kondo impurity system at low temperature ($T \ll T_K$) has been well described as a local *Fermi liquid* [35].

The first nonperturbative approach for the $S = \frac{1}{2}$ Kondo problem, which is valid for all temperatures, was the Numerical Renormalization Group (NRG) method of Wilson [36]. At low temperature a many-body singlet ground state is formed with effective exchange coupling which is infinite at $T = 0$. Thus the magnetic impurity susceptibility χ_{imp} is finite as $T \to 0$ and is given by

$$\chi_{\text{imp}}(T=0) = \frac{1}{T_0} \tag{3.5}$$

with [37]

$$\frac{T_K}{T_0} = \left(\frac{2}{\pi}\right)^2 . \tag{3.6}$$

Here T_0 may be defined as a Kondo temperature and it is related to T_K, which is defined in the high-temperature perturbation theory, with the *Wilson number* $(2/\pi)^2$.

Anderson Model While the Kondo model in the form of Hamiltonian Eq. (3.1) describes the interaction between the localized and conduction electron, it is assumed that there is already a magnetic moment on the impurity associated with a spin S. Meanwhile, the Anderson model [38], which is another model for the interaction of a localized electron with a conduction band, provides the more interesting and richer physics including the formation of the magnetic moment. The Hamiltonian for the Anderson model has the form

$$H = \sum_{\vec{k},\sigma} \epsilon_{\vec{k}} c^\dagger_{\vec{k},\sigma} c_{\vec{k},\sigma} + \sum_{\vec{k},\sigma} V(c^\dagger_{\vec{k},\sigma} d_\sigma + d^\dagger_\sigma c_{\vec{k},\sigma}) + \sum_\sigma \epsilon_d n_{d,\sigma} + U n_{d,\uparrow} n_{d,\downarrow} \, , \tag{3.7}$$

where $d^\dagger_\sigma$ (d_σ) is a creation (annihilation) operator for an electron in an impurity state with energy ϵ_d and spin σ, and $n_{d,\sigma} = d^\dagger_\sigma d_\sigma$; V is the hybridization matrix element between the impurity state and the conduction band; and U is an on-site Coulomb repulsion between the electrons of opposite spin in the impurity state. There is an energy parameter $\Gamma = \pi N_0 V^2$ which characterizes the hybridization width in the impurity electron spectrum. The Anderson model exhibits from nonmagnetic to magnetic behavior of the impuritydepending on the given parameters. There is a canonical transformation of Schrieffer and Wolff [39] by which the Kondo model can be deduced from the Anderson model in addition to other less relevant terms.

In the particle-hole symmetric case where $\epsilon_d = -U/2$ and $n_d = 1$, the formation of the local moment depends on $U/\pi\Gamma$. In the limit $U/\pi\Gamma \gg 1$, a spin-$\frac{1}{2}$ magnetic moment on the impurity couples antiferromagnetically to the conduction electrons with an exchange interaction $J = -8\Gamma/\pi N_0 U$. Then the Kondo temperature T_0 is defined by [11]

$$T_0 = U\sqrt{\frac{\Gamma}{2U}} \exp\left(-\frac{\pi U}{8\Gamma} + \frac{\pi\Gamma}{2U}\right). \tag{3.8}$$

The NRG calculations of Krishna-murthy *et al.* [40] show the universality of the magnetic impurity susceptibility $\chi_{\rm imp}$ as a function of T/T_0 and also give Eq. (3.6) in connection with T_K.

Not only the transport properties but also dynamics and thermodynamic properties have been studied with the Kondo model and the Anderson model, and they show good agreement with the experiments. One important feature in the Kondo problem is that there is only one parameter which determines the physical properties of the system for all relevant temperatures; i.e., the Kondo temperature T_0.

3.1.2 Superconductivity

Since Bardeen, Cooper, and Schrieffer (BCS) [41] presented the model of superconductivity, it has been well known that the superconductivity in conventional superconductors arises from the coherent pairing of electrons with time-reversal symmetry [1]. The pairing between electrons with opposite momenta and opposite spins reduces the excitation density of states near the Fermi energy, and leads to the superconducting state with condensation of the pairs below the transition temperature T_{c0}. Thus this results in an energy gap $2\Delta_{00}$ in the excitation spectrum of the superconductors, which is responsible for the many properties of the superconductors.

The most direct observation of the superconducting density of states came from tunneling experiments [42]. In the tunneling of electrons between a normal metal and a superconductor, the normalized tunneling conductance $\sigma(V)$ at an applied voltage V is measured. Here $\sigma(V)$ is the ratio of the dynamical conductance dI/dV for the tunneling between the normal metal and the superconductor, to the value for the tunneling between both metals when they are in the normal state. Then $\sigma(V)$ gives a direct measurement of the superconducting density of states $N(eV)/N_0$. This can be easily seen from the calculation of the tunneling current with an applied voltage V; i.e.,

$$I \propto \int d\epsilon N(\epsilon) N_n(\epsilon + eV) f(\epsilon)[1 - f(\epsilon + eV)] , \tag{3.9}$$

where $N_n(\epsilon)$ is the density of states in the normal metal and $f(\epsilon)$ is the Fermi distribution function. Since we can neglect the variation of $N_n(\epsilon)$ within the energy gap, the dynamical conductance dI/dV is easily obtained at zero temperature

$$\lim_{T\to 0}\frac{dI}{dV} \propto \lim_{T\to 0}\int d\epsilon N(\epsilon)\frac{df(\epsilon+eV)}{dV} = N(-eV), \tag{3.10}$$

which gives directly the superconducting density of states.

Fig. 3.4 shows the experimental result [43] along with the BCS prediction for the superconducting density of states of Pb, where $Al/Al_2O_3/Pb$ junction was used. Although the BCS theory well describes the properties of many conventional su-

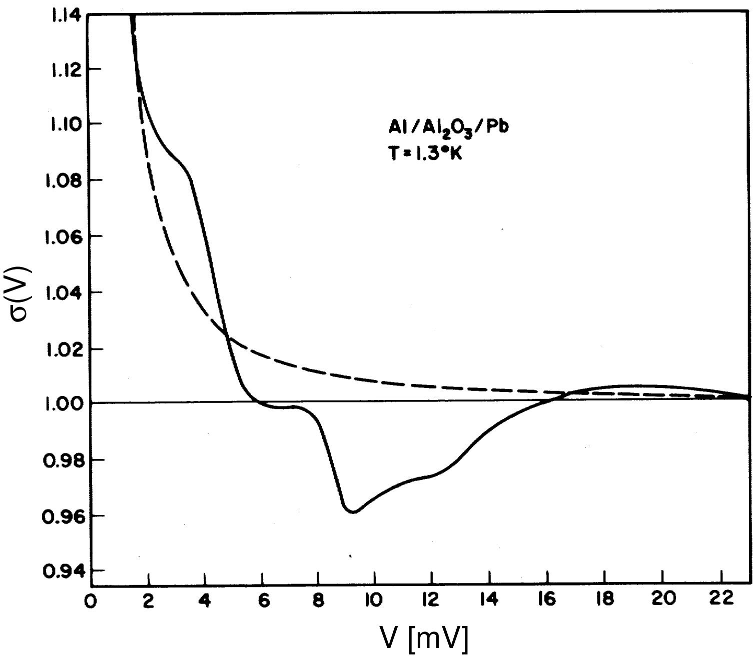

Figure 3.4: *Tunneling conductance $\sigma(V)$ vs. voltage V for* $Al/Al_2O_3/Pb$ *junction [43]. The dashed line represents the BCS prediction.*

perconductors, particularly weak-coupling (in terms of the strength of the electron-phonon interaction) superconductors such as Al, Sn, and In, there are deviations of observed properties from the BCS predictions as one can see in Fig. 3.4. Furthermore the BCS theory does not provide realistic electron-electron interaction mechanism. Since the effective electron-electron interaction induced by phonons has frequency dependence and is not a real function, we must take account of the retardation and damping effects properly. Thus the instantaneous interaction between electrons in the BCS theory is not adequate for the realistic description of superconductors, specially when the electron-phonon interaction is strong as in Pb and Hg.

The theory of superconductivity [1, 2] which includes the retardation and damping effects was provided by Eliashberg [15]. In Appendix C, we briefly review the self-consistent Eliashberg equations using the Nambu [16] formalism. Details of the definitions and derivations in the Eliashberg equations should be referred to Appendix C.

In the Nambu formalism, the self-energy $\mathbf{\Sigma}(i\omega_n)$ due to the electron-phonon interaction is evaluated within the Migdal limit [44] from Fig. C.1. This leads to the self-consistent Eliashberg equations with the gap function $\Delta(i\omega_n)$ and the renormalization function $Z(i\omega_n)$:

$$Z(i\omega_n) = 1 + \frac{\pi T}{\omega_n} \sum_{m=-\infty}^{\infty} \lambda(i\omega_n - i\omega_m) \frac{\omega_m}{\sqrt{\omega_m^2 + \Delta^2(i\omega_m)}}, \tag{3.11}$$

$$\Delta(i\omega_n)Z(i\omega_n) = \pi T \sum_{m=-\infty}^{\infty} \lambda(i\omega_n - i\omega_m)\frac{\Delta(i\omega_m)}{\sqrt{\omega_m^2 + \Delta^2(i\omega_m)}}\,, \tag{3.12}$$

where the λ-function is defined by

$$\lambda(i\omega_n) = -\int_{-\infty}^{\infty} d\omega' \frac{\alpha^2 F(\omega')}{i\omega_n - \omega'} \tag{3.13}$$

with the electron-phonon spectrum function $\alpha^2 F(\omega)$. Then the superconducting density of states $N(\omega)/N_0$ is obtained from the analytic continuations of $\Delta(i\omega_n)$ and $Z(i\omega_n)$:

$$\frac{N(\omega)}{N_0} = \mathrm{Re}\frac{\omega}{\sqrt{\omega^2 - \Delta^2(\omega)}}\,. \tag{3.14}$$

Given the electron-phonon spectrum function $\alpha^2 F(\omega)$, the superconducting transition temperature T_{c0} is also evaluated by the methods of Owen and Scalapino [45]. The instability in the particle-particle t matrix, which corresponds to the phase transition of the metal into the superconducting state, is obtained when the eigenvalue of the pairing matrix $\mathbf{M}$ becomes 1:

$$\begin{aligned} M_{nm} \;=\; & \frac{1}{\sqrt{(2n+1)(2m+1)}} \int_0^{\infty} d\nu \frac{2\alpha^2(\nu)F(\nu)}{\nu} \left\{ \frac{\nu^2}{(n-m)^2+\nu^2} \right. \\ & \left. + \frac{\nu^2}{(n+m+1)^2+\nu^2} - \left[\sum_{l=0}^{2n} \frac{\nu^2}{(n-l)^2+\nu^2}\right] \delta_{nm} \right\}\,, \end{aligned} \tag{3.15}$$

where δ_{nm} is the element of the unit matrix $\mathbf{I}$ and $\nu = \omega/2\pi T$. Thus the superconducting transition temperature T_{c0} is obtained when $\det(\mathbf{I} - \mathbf{M}) = 0$.

3.2 Previous Results

3.2.1 Experiments

Experimentally, the existence of states within the superconducting gap due to magnetic impurities has been shown from tunneling experiments [46, 47]. The gap states can be observed in measurements of the normalized tunneling conductance between a homogeneous magnetic alloy superconductor and a normal metal. Also tunneling experiments on a pure superconductor with overlayed magnetic alloys can show the same effects.Since many of the well-studied Kondo alloys have noble metal hosts such as Cu and Au which are not superconducting, the latter tunneling experiments, where the superconductivity is induced in a film of the Kondo alloys by the proximity of a pure superconductor, can be used to get a wide range of Kondo temperature and be useful for the systematic study of the gap states.

Earlier, several experiments [46] using homogeneous magnetic alloy superconductors succeeded to show the existence of the gap states but failed to show the details of the gap states due to the lack of resolution. The first systematic experimental studies to show the gap states in detail were done by Dumoulin *et al.* [47] using dilute magnetic alloys in superconducting proximity. Here we briefly review their experiments and results.

Fig. 3.5 shows a section of a typical tunneling junction used by Dumoulin *et al.*. The well-studied Kondo alloy CuX (X=Cr,Fe, Mn, or Co) film is sandwiched in between a normal metal Al and a superconducting Pb which induces superconductivity in CuX. Then the Kondo temperature T_0 of the CuX film is determined from the value

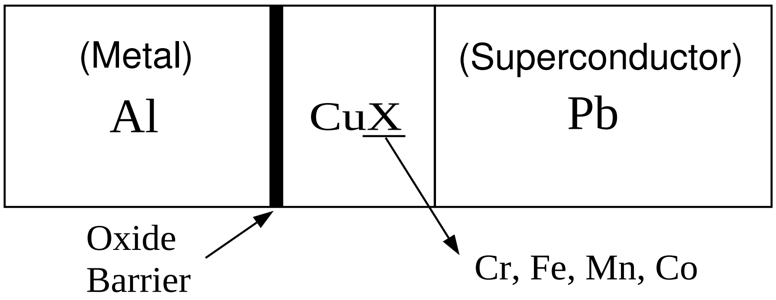

Figure 3.5: *Typical junction used for tunneling experiments by Dumoulin et al. [47]. The superconductivity is induced in the dilute magnetic alloys CuX (X=Cr,Fe, Mn, or Co) by a superconducting Pb.*

for the bulk CuX. Also Cu films in proximity with Pb are treated as equivalent BCS superconductors; i.e., determination of the gap parameter Δ_{00} in Cu-Pb systems gives the equivalent BCS superconducting critical temperature $T_{c0}^* = \Delta_{00}/1.76$. For low concentration of the magnetic impurities X in CuX-Pb systems, the gap parameter Δ_0 is approximated to Δ_{00}. Note that one can vary the critical temperature T_{c0}^* with variation of Cu film thickness d_N or Pb film thickness d_S while keeping the magnetic properties and the concentration of the impurities c constant.

The results of the tunneling experiments for a CuCr-Pb system are shown in Fig. 3.6–3.8. Fig. 3.6 shows the temperature dependence of the gap states for one CuCr-Pb junction having the following parameters: $c = 17$ ppm, $d_N = 250$ Å, $d_S = 2000$ Å, $\Delta_0 = 0.8$ mV, and $T_{c0}^* = 5.3$ K. For enough low temperatures to exhibit the localized gap states, the location of the peak δ of the gap states is determined with the maximum conductance σ_m within the gap. As the temperature increases, the thermal smearing washes out the structure of the gap states.

Fig. 3.7 shows the dependence of the height σ_m of the gap states on the concentration of the impurities. The maximum conductance σ_m within the gap is measured at $T = 0.95$ K increasing the concentration of Cr from 25 to 300 ppm, while keeping the geometrical parameters $d_N = 250$ Å and $d_S = 2000$ Å constant such that $\Delta_0 = 0.8$ mV and $T_{c0}^* = 5.3$ K are constant. The inset in Fig. 3.7 shows that σ_m varies as $\sqrt{c}$.

Also the location of the peak δ of the gap states as a function of T_0/T_{c0}^* can be studied varing d_N or d_S on the same Kondo alloy where T_{c0}^* is varied but T_0 and c are fixed. For solid lines in Fig. 3.8, $c = 17$ ppm and $T_0 \approx 1$ K are fixed for CuCr, and d_S is decreasing with fixed $d_N = 250$ Å to decrease T_{c0}^*. The dotted line is for $c = 10$ ppm, $d_N = 400$ Å, and $d_S = 2000$ Å. Then the normalized location y of the gap states is taken by $y = \delta/\Delta_0$. With increasing T_0/T_{c0}^* by decreasing T_{c0}^*, y increases for the CuCr-Pb system.

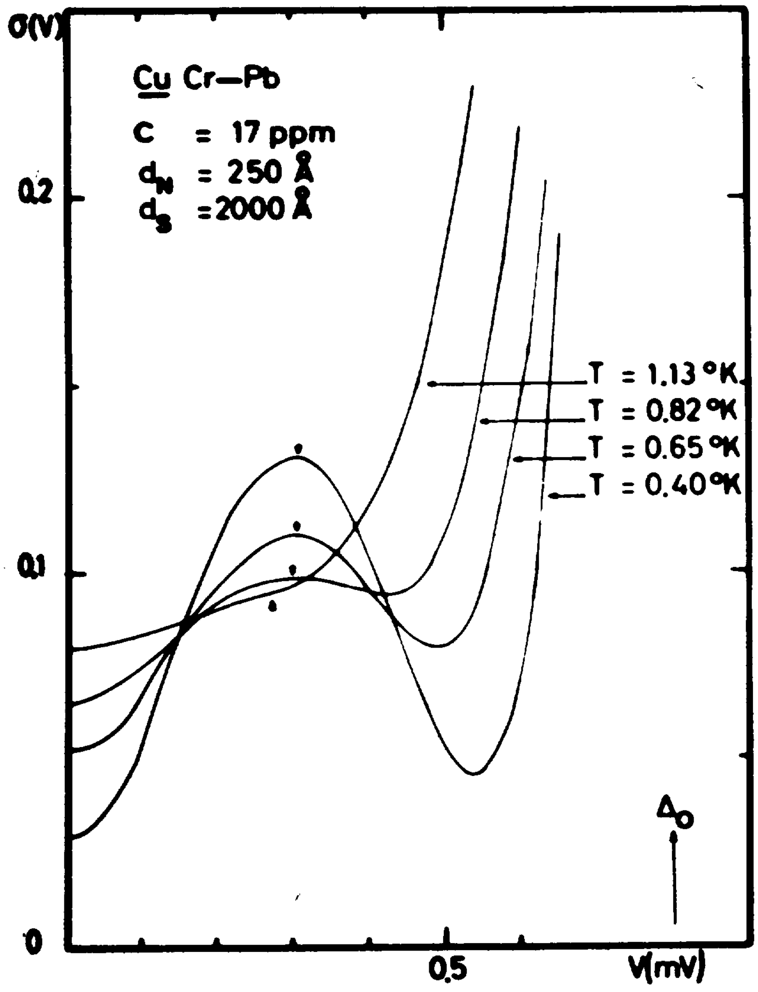

Figure 3.6: *Tunneling conductance $\sigma(V)$ for CuCr-Pb junction at different temperatures [47].*

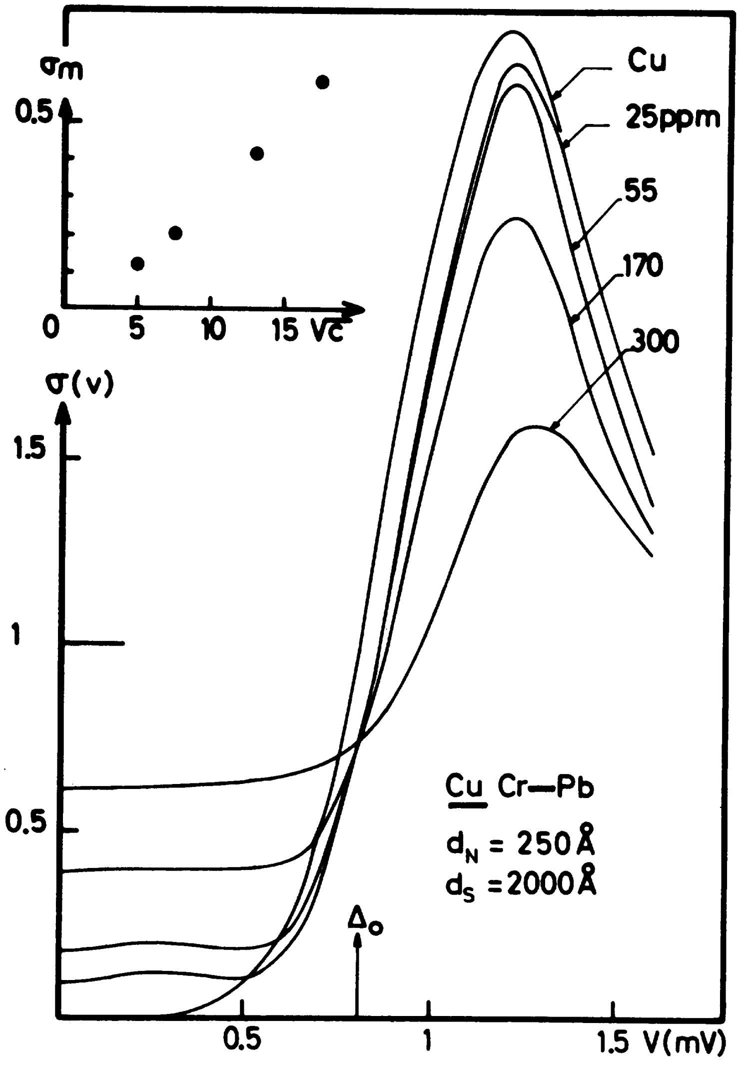

Figure 3.7: *Tunneling conductance $\sigma(V)$ for CuCr-Pb junction with various concentration c of Cr. The inset shows the maximum conductance σ_m vs. $\sqrt{c}$ [47].*

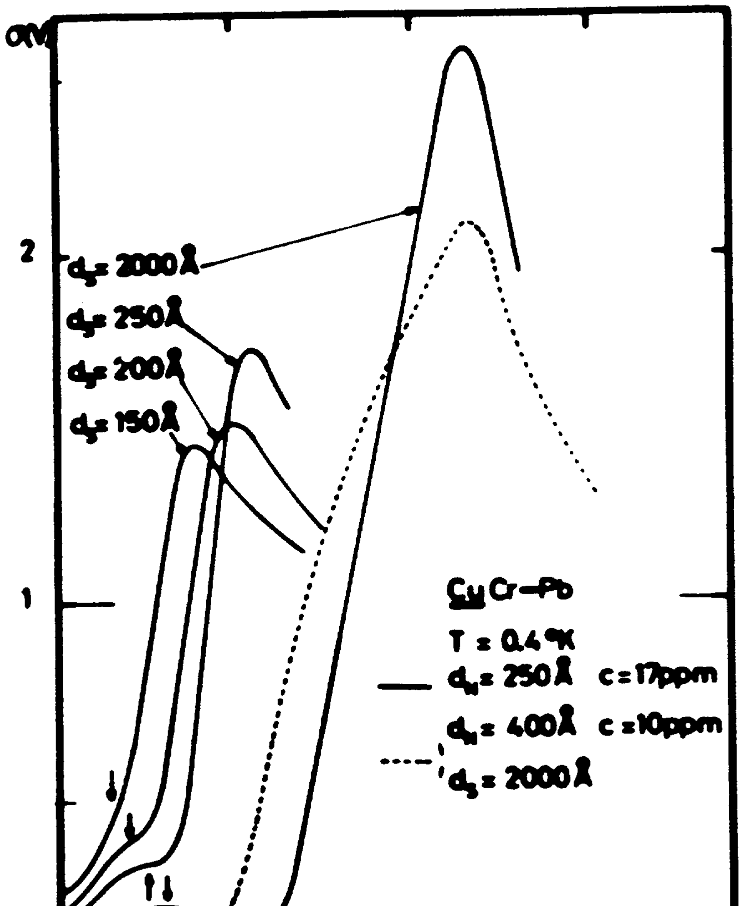

Figure 3.8: *Tunneling conductance $\sigma(V)$ for CuCr-Pb junction with variation of d_N or d_S [47].*

Tunneling experimental studies for CuFe-Pb, CuMn-Pb, and AuFe-Pb systems have been carried with similar procedures used in above CuCr-Pb system. Table 3.1 shows the results for those systems concerning the normalized location y of the gap states.

Table 3.1: *Normalized location y of the gap states for various Kondo alloys in superconducting proximity with Pb. y is given for $T^*_{c0} = 5$ K and the arrows indicate the change of y with increasing T_0/T^*_{c0} by decreasing T^*_{c0}.*

Alloy	T_0 [°K]	y	
		$T^*_{c0} = 5K$	T_0/T^*_{c0} $\uparrow$
CuMn	0.01	0.6	$\downarrow$
AuFe	0.5	0.2	$\downarrow$
CuCr	1	0.34	$\uparrow$
CuFe	30	0.85	$\uparrow$

Through these experiments they succeeded to show clearly the existence of the gap states within the superconducting gap induced by magnetic impurities. They showed that the location of the gap states is characterized by T_0/T^*_{c0} and with increasing T_0/T^*_{c0} the gap states move toward the center of the gap and move back to the gap edge (see Table 3.1). They also showed that the maximum height of the gap states is linearly proportional to $\sqrt{c}$. However, note that their quantitative analysis depends on the quasi-BCS approximation, in which the superconducting density of states induced by the proximity effect is assumed to be close to that of a BCS superconductor with

Δ_{00} and T^*_{c0}. Thus it would be desirable to have systematic tunneling experiments on homogeneous magnetic alloy superconductors.

3.2.2 Theories

Since Abrikosov and Gorkov (AG) [48] showed that the magnetic impurities in superconductors have significant effects on the superconductivity, many theoretical attempts have been made to describe the effects. Here we briefly mention a few of those previous theories emphasizing the nature of the assumption or approximation they used and the comparable results with ours.

AG [48] used a second-order Born approximation of the exchange interaction J in the superconducting state, which is valid for $J \to 0$ and $T_0 \ll T_{c0}$, and indicated that the magnetic impurities could cause *gapless superconductors*. However this approximation does not include the *Kondo effect* which arises beyond the second-order perturbations in J, and it does not produce any structure of the states within the gap.

Shiba [49], using a classical spin (which means $S \to \infty$, $J \to 0$, so JS remains finite) in superconductors, treated the interaction to higher orders than J^2 and found that the gap states could have structures distinguishable from the continuous states obtained by AG. However this model, in which the classical spin is equivalent to the local magnetic field, ignores the quantum effects of the spin and hence does not include the Kondo effect.

There has been many theoretical attempts also to take account of Kondo effect on superconductivity, but most of them are based upon perturbative approaches specialized for either $T_0 \ll T_{c0}$ (*high temperature regime*) or $T_0 \gg T_{c0}$ (*Fermi liquid regime*). For example, Zittartz, Bringer, and Müller-Hartmann (ZBM) [50] studied the problem using the Nagaoka-Suhl [31, 32] approximation which is a self-consistent high-temperature perturbation theory in the exchange interaction J. As a result, they found that the location δ of the gap states is a function of T_K/T_{c0}. Thus the normalized location of the gap states, $y = \delta/\Delta_0$, was calculated analytically for $T = T_{c0}$ limit, and it is given by

$$y = \left[\frac{\ln^2(T_K/T_c)}{\ln^2(T_K/T_c) + \pi^2 S(S+1)}\right]^{1/2}. \tag{3.16}$$

Also for $T = 0$ limit, y was calculated numerically [51], and we reproduce the results for $S = \frac{1}{2}$ in Fig. 3.9. Since the gap states are symmetric about the Fermi energy ($y = 0$), only positive energies are plotted in Fig. 3.9.

ZBM also studied the effect of the finite concentration c of the impurities using a self-consistent t-matrix approximation [50]. At low concentration of the impurities,

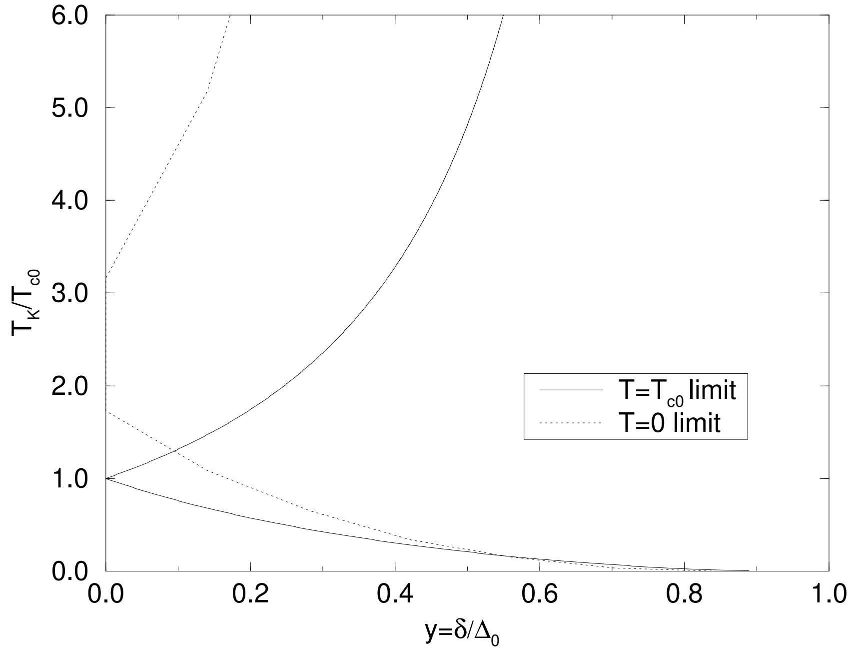

Figure 3.9: *Normalized location of gap states, $y = \delta/\Delta_0$, as a function of T_K/T_{c0} in the ZBM [50, 51] results. The solid line is for $T = T_{c0}$ limit and the dotted line for $T = 0$ limit. δ is the energy difference between the center of the gap and the peak of the gap states, and Δ_0 is the superconducting gap parameter.*

the density of states $N(\omega)/N_0$ within the gap is given by

$$\frac{N(\omega)}{N_0} = \frac{1}{2}(1-y^2)^{-3/2}\left[2c^*(1-y^2)^{3/2} - (\frac{\omega}{\Delta_0} - y)^2\right]^{1/2}, \qquad (3.17)$$

where $c^* = c/[(2\pi)^2 N_0 T_{c0}]$. Note that the width and the height of the gap states are both proportional to $\sqrt{c}$, which agrees with the experiments [47], but the integrated weight of the gap states is constant as a function of y, which is inconsistent with the experiments [47].

Although the ZBM results give some qualitative agreement with the experiments [47], there are deviations quantitatively and the ZBM approximation becomes correct only when $T_0 \ll T_{c0}$.

Later Matsuura [52] used an approximate interpolation method between $T_0 \ll T_{c0}$ and $T_0 \gg T_{c0}$ regime based on the Anderson [38] model within the BCS Hamiltonian. He found that for a single spin-$\frac{1}{2}$ impurity system the ground state (gap state) is a singlet (doublet) for $T_0 \gg T_{c0}$ while the ground state (gap state) is a doublet (singlet) for $T_0 \ll T_{c0}$. It is easy to understand why the impurity has such states in these limits. When T_0 is vanishingly small ($J = 0$) the impurity decouples from the superconducting host and has a doublet ground state. Even when T_0 is finite, but small ($T_0 \ll T_{c0}$), the superconductivity forms before the impurity can be screened by the Kondo effect, so it maintains its doublet ground state. However, in the limit where $T_0 \gg T_{c0}$, the Kondo effect completely screens the impurity before the superconducting transition temperature is reached. Thus, the impurity will have a singlet ground state in this limit.

Nonperturbative approaches have been also employed, which can cover the whole regime from $T_0 \ll T_{c0}$ to $T_0 \gg T_{c0}$. Satori *et al.* [55] applied Wilson's [36] Numerical Renormalization Group (NRG) method to the problem of a single spin-$\frac{1}{2}$ impurity in a BCS superconductor. Then the crossover behavior between a doublet and a singlet ground state is traced by changing the the exchange J relative to the pure superconducting gap parameter Δ_{00}, and they found the crossover occurs at $T_K/\Delta_{00} \simeq 0.3$. This, however, does not account for the self-consistent effect of a finite concentration of impurities or address thermodynamic properties.

As another nonperturbative approach, Jarrell *et al.* [12] introduced a self-consistent Quantum Monte Carlo (QMC) method to the dilute magnetic alloy superconductors. Then they used the Maximum Entropy Method (MEM) [13] to obtain the superconducting density of states. However, due to the complicated structure of the density of states, the MEM alone does not produce enough resolution for a systematic study for the problem.

Thus we will discuss a novel method to overcome these above limitations in this thesis. We use a combination of a self-consistent QMC method for the magnetic impurities, Eliashberg equations for the host superconductors, MEM for the analytic continuation of the impurity Green's function, and a formally exact analytic continuation method [14] for the host Green's function.

3.3 Model and Formalism

3.3.1 Impurity: Anderson Impurity

We model the magnetic impurity with a symmetric Anderson model [38] in the limit of infinite metallic bandwidth. As mentioned in Section 3.1.1, this model is characterized by an on-site Coulomb repulsion U and a hybridization width $\Gamma = \pi N_0 V^2$, where V is the hybridization matrix element and N_0 is the density of states at the Fermi energy. In the limit $U \gg \Gamma$, a spin-$\frac{1}{2}$ magnetic moment on the impurity couples antiferromagnetically to the conduction electrons with an exchange $J = -8\Gamma/\pi N_0 U$ and the Kondo temperature T_0 is defined by Eq. (3.8).

Then the Hamiltonian for a single impurity in the superconducting state may be written as

$$\begin{aligned} H &= \sum_{\vec{k},s} \epsilon_{\vec{k}} c^\dagger_{\vec{k},s} c_{\vec{k},s} + \sum_{\vec{k},s} \Delta_{\vec{k}} (c_{\vec{k},\uparrow} c_{-\vec{k},\downarrow} + c^\dagger_{-\vec{k},\downarrow} c^\dagger_{\vec{k},\uparrow}) + \sum_{\vec{k},s} V (c^\dagger_{\vec{k},s} d_s + d^\dagger_s c_{\vec{k},s}) \\ &\quad + \epsilon_d (n_{d,\uparrow} + n_{d,\downarrow}) + U n_{d,\uparrow} n_{d,\downarrow} \,, \end{aligned} \tag{3.18}$$

where $\Delta_{\vec{k}}$ is the superconducting order parameter. The difficulty in solving the Hamiltonian arises from the electron-electron interaction on the impurity site. However, this Hamiltonian can be treated nonperturbatively using the QMC algorithm of Hirsch and Fye [60]. In Appendix D, we derive the QMC algorithm applying the Hirsch-Fye method in the Nambu [16] formalism. Here we define the impurity Green's function $\mathbf{G}_d(\tau)$ in the Nambu formalism in the same way as the host Green's function $\mathbf{G}(\tau)$ in Eq. (C.3):

$$\mathbf{G}_d(\tau) = \begin{pmatrix} \langle T_\tau d_\uparrow(\tau) d_\uparrow^\dagger(0)\rangle & \langle T_\tau d_\uparrow(\tau) d_\downarrow(0)\rangle \\ \langle T_\tau d_\downarrow^\dagger(\tau) d_\uparrow^\dagger(0)\rangle & \langle T_\tau d_\downarrow^\dagger(\tau) d_\downarrow(0)\rangle \end{pmatrix}. \tag{3.19}$$

In the QMC algorithm, we transform the problem of interacting electrons to one of non-interacting electrons scattering off of a time-dependent field (or Hubbard-Stratonovich field). This QMC simulation requires as an input the initial, $U = 0$, impurity Green's function $\mathbf{G}_d^0$, which corresponds to a constant Hubbard-Stratonovich field configuration. We may determine $\mathbf{G}_d^0$ from the Dyson equation (see Fig. 3.10 (a)). Note that in Fig. 3.10 (a) $\mathbf{G}_d^0$ also requires the fully dressed Greens function $\mathbf{G}$ of the host which we will discuss in the following section. Then the QMC simulation produces the fully-dressed impurity Green's function $\mathbf{G}_d$ to all orders of U (see Fig. 3.10 (b)).

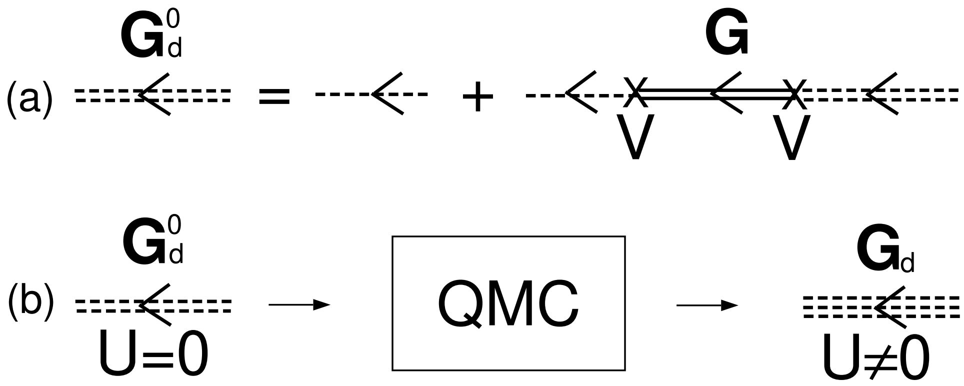

Figure 3.10: (a)*Feynman diagrams for the initial impurity Green's function* $\mathbf{G}_d^0$ *with* $U = 0$*. The single dotted line is the free-electron Green's function of the impurity; the double dotted line is the initial,* $U = 0$*, impurity Green's function* $\mathbf{G}_d^0$*; the double solid line is the host Green's function* $\mathbf{G}$*; and* X *represents the hybridization matrix element* V*.* (b) *The fully-dressed impurity Green's function* $\mathbf{G}_d$ *for* $U \neq 0$ *is produced by the QMC simulation with the initial impurity Green's function* $\mathbf{G}_d^0$ *for* $U = 0$ *as an input.*

3.3.2 Host: Strong-Coupling Superconductor

We describe the host superconductor with the self-consistent Eliashberg equations reviewed in Appendix C. It is assumed that the concentration c of the impurities embedded in the superconducting host is small and there are no correlations between them. However, it is also assumed that the distance between the impurities is much smaller than the superconducting coherence length ($\sim 10^3 \mathring{A}$), which is the physically interesting limit; e.g., for a few percent of the impurities, the distance between the impurities is the order of 10 Å. Thus taking an average over all possible positions of the impurities, we restore the momentum conservation and we can describe the effect of the impurities on the superconducting state using a standard perturbation theory. Since there are no correlations between the impurities, the contribution of the impurities to the self-energy is proportional to the concentration c.

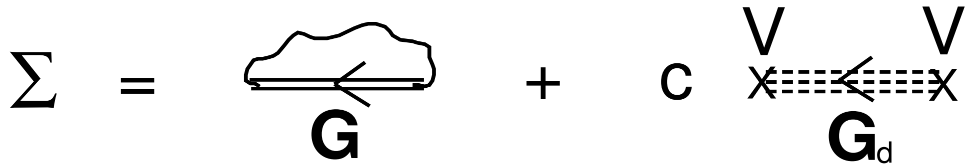

Figure 3.11: *Feynman diagrams for the self-energy* $\mathbf{\Sigma}$ *of the host due to the electron-phonon interaction and the impurities, where the wiggle line represents phonon Green's function; the double solid line is the host Green's function* $\mathbf{G}$*; c is the concentration of impurities; the triple dotted line is the fully-dressed impurity Green's function* $\mathbf{G}_d$ *to all orders of* U*; and X represents the hybridization matrix element* V*.*

Fig. 3.11 shows the diagrams for the self-energy $\mathbf{\Sigma}$ from the contribution of the electron-phonon interaction and the impurities. Then the self-energy $\mathbf{\Sigma}(i\omega_n)$ is readily evaluated using Eq. (C.10):

$$\mathbf{\Sigma}(i\omega_n) = cV^2\mathbf{G}_d(i\omega_n) + \frac{T}{N_0}\sum_{m=-\infty}^{\infty}\lambda(i\omega_n - i\omega_m)\boldsymbol{\tau}_3\mathbf{G}(i\omega_m)\boldsymbol{\tau}_3\,. \tag{3.20}$$

Therefore we obtaine the self-consistent Eliashberg equations from Eq. (3.20) in the same way as in Appendix C:

$$Z(i\omega_n) = 1 - \frac{cV^2[\mathbf{G}_d(i\omega_n)]_{11}}{i\omega_n} + \frac{\pi T}{\omega_n}\sum_{m=-\infty}^{\infty}\lambda(i\omega_n - i\omega_m)\frac{\omega_m}{\sqrt{\omega_m^2 + \Delta^2(i\omega_m)}} \tag{3.21}$$

and

$$\Delta(i\omega_n)Z(i\omega_n) = -cV^2[\mathbf{G}_d(i\omega_n)]_{12} + \pi T \sum_{m=-\infty}^{\infty} \lambda(i\omega_n - i\omega_m)\frac{\Delta(i\omega_m)}{\sqrt{\omega_m^2 + \Delta^2(i\omega_m)}}, \quad (3.22)$$

where $[\mathbf{G}_d(i\omega_n)]_{11}$ and $[\mathbf{G}_d(i\omega_n)]_{12}$ denote the diagonal and the off-diagonal part of $\mathbf{G}_d(i\omega_n)$ each.

We assume that the conduction electrons interact with the phonons with a coupling strength $\lambda(0)$ and the phonon density of states $F(\omega)$ consists of a Lorentzian-like peak centered at ω_0. With the normalization $\int_0^\infty F(\omega)d\omega = 1$, the electron-phonon spectrum function, $\alpha^2 F(\omega)$, is given by

$$\alpha^2 F(\omega) = \frac{\lambda(0)\omega_L(\omega_0^2 + \omega_L^2)}{2\pi\omega_0}\left\{\frac{1}{(\omega-\omega_0)^2 + \omega_L^2} - \frac{1}{(\omega+\omega_0)^2 + \omega_L^2}\right\}. \quad (3.23)$$

When the width $\omega_L = 0$, it represents Einstein phonon of frequency ω_0 with the coupling constant $\lambda(0)$; i.e.,

$$\alpha^2 F(\omega) = \frac{\lambda(0)\omega_0}{2}\left\{\delta(\omega-\omega_0) - \delta(\omega+\omega_0)\right\} \quad (3.24)$$

with the delta-function $\delta(\omega)$.

3.3.3 Solving the Self-Consistent Equations

Fig. 3.10 and Fig. 3.11 form a set of self-consistent equations for the problem. To solve the Eliashberg equations in Fig. 3.11, we need to find the fully-dressed impurity Green's function $\mathbf{G}_d$ which is obtained through the QMC simulation. The QMC simulation requires also the initial impurity Green's function $\mathbf{G}_d^0$ with $U = 0$. $\mathbf{G}_d^0$ also requires the fully dressed Greens function $\mathbf{G}$ of the host which is determined from the Eliashberg equations in Fig. 3.11. We iterate this set of equations until the self-consistency is satisfied.

3.4 Analytic Continuation

As shown in Fig. 3.12, solving the self-consistent set of equations, we obtain the fully-dressed impurity Green's function $\mathbf{G}_d(\tau)$ in imaginary time τ as well as the gap function $\Delta(i\omega_n)$ and the renormalization function $Z(i\omega_n)$ in Matsubara frequencies $\omega_n = (2n+1)\pi T$. Thus proper analytic continuations to real frequencies ω are required to obtain the relevant (dynamic) physical quantities such as the density of states $N(\omega)/N_0$ and the impurity spectral function $\mathbf{A}(\omega)$.

We use the Maximum Entropy Method (MEM) [13] to obtain the impurity spectral function $\mathbf{A}(\omega)$ from $\mathbf{G}_d(\tau)$ measured in the QMC simulation, and hence obtain the retarded fully-dressed impurity Green's function $\mathbf{G}_d(\omega)$. Then we use a formally

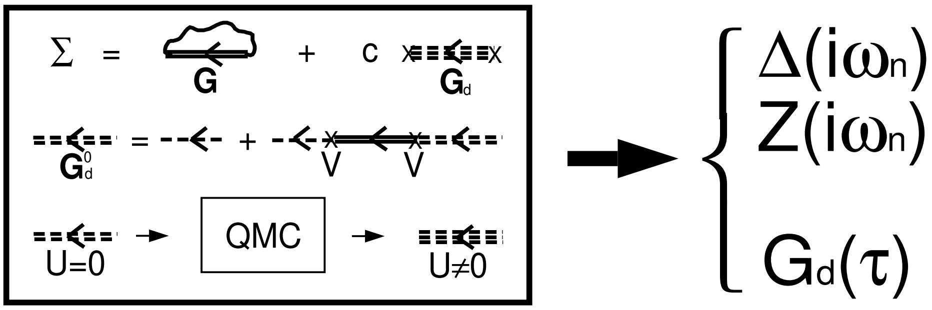

Figure 3.12: *The self-consistent set of equations in the box produces the gap function* $\Delta(i\omega_n)$ *and the renormalization function* $Z(i\omega_n)$ *in Matsubara frequencies* ω_n*, and the fully-dressed impurity Green's function* $\mathbf{G}_d(\tau)$ *in imaginary time* τ*.*

exact analytic continuation method [14] to obtain the gap function $\Delta(\omega)$ and the renormalization function $Z(\omega)$ from $\Delta(i\omega_n)$ and $Z(i\omega_n)$ with $\mathbf{G}_d(\omega)$, and therefore obtain the density of states $N(\omega)/N_0$ from Eq. (3.14).

3.4.1 Impurity Green's Function

For various impurity problems, it has been shown that the MEM [13] gives good results in the analytic continuation of the impurity Green's functions. In Appendix E, we summarize the basic idea of the MEM based on the reference [13].

In the analytic continuation problem of the impurity Green's functions, the equation is given by

$$G(\tau) = \int_{-\infty}^{\infty} d\omega K(\tau,\omega) A(\omega) \tag{3.25}$$

given the data $G(\tau)$ from the QMC simulations and the kernel $K(\tau,\omega)$ with the spectral function $A(\omega)$ which we want to extract. Then the MEM seeks the *most* *probable* spectral function (or *image*) using the properties of the non-negativity and the normalizablity of the spectral function.

For our problem, therefore, we can directly apply the MEM to obtain the diagonal part of the spectral function $[\mathbf{A}(\omega)]_{11}$ from the QMC data $[\mathbf{G}_d(\tau)]_{11}$; i.e.,

$$[\mathbf{G}_d(\tau)]_{11} = \int_0^\infty d\omega \frac{e^{-\tau\omega} + e^{-(\beta-\tau)\omega}}{1 + e^{-\beta\omega}} [\mathbf{A}(\omega)]_{11}\,, \tag{3.26}$$

where we imposed the symmetry of $[\mathbf{A}(\omega)]_{11}$ from the particle-hole symmetry (i.e., $[\mathbf{A}(-\omega)]_{11} = [\mathbf{A}(\omega)]_{11}$) on $K(\tau,\omega)$.

Similarly, we may have

$$[\mathbf{G}_d(\tau)]_{12} = \int_0^\infty d\omega \frac{e^{-\tau\omega} - e^{-(\beta-\tau)\omega}}{1 + e^{-\beta\omega}} [\mathbf{A}(\omega)]_{12}\,. \tag{3.27}$$

Note that the symmetry imposed on $K(\tau,\omega)$ is $[\mathbf{A}(-\omega)]_{12} = -[\mathbf{A}(\omega)]_{12}$ since $[\mathbf{G}_d(\beta-\tau)]_{12} = -[\mathbf{G}_d(\tau)]_{12}$. However, since the off-diagonal part of the spectral function $[\mathbf{A}(\omega)]_{12}$ is not positive definite, we cannot apply directly the MEM to analytically continue $[\mathbf{G}_d(\tau)]_{12}$.

To maintain the non-negativity of the image in the MEM, we add a positive definite constant b to the integrand $[\mathbf{A}(\omega)]_{12}$ in Eq. (3.27). Then Eq. (3.27) becomes

$$[\mathbf{G}_d(\tau)]_{12} + b\int_0^\infty d\omega \frac{e^{-\tau\omega} - e^{-(\beta-\tau)\omega}}{1 + e^{-\beta\omega}} = \int_0^\infty d\omega \frac{e^{-\tau\omega} - e^{-(\beta-\tau)\omega}}{1 + e^{-\beta\omega}} [[\mathbf{A}(\omega)]_{12} + b]\,. \tag{3.28}$$

Thus new image $[\mathbf{A}(\omega)]_{12} + b$ is obtained from the shifted data of the left hand side in Eq. (3.28), and hence we obtain $[\mathbf{A}(\omega)]_{12}$. In practice, we introduce the cut-off frequency ω_c assuming that $[\mathbf{A}(\omega)]_{12}$ is well bounded for high frequencies.

Then the retarded fully-dressed impurity Green's function $\mathbf{G}_d(\omega)$ is easily obtained from the following relation:

$$\mathbf{G}_d(\omega) = \int_{-\infty}^{\infty} d\omega' \frac{\mathbf{A}(\omega')}{\omega - \omega' + i\eta} \tag{3.29}$$

with $0 < \eta \ll 1$.

3.4.2 Host Green's Function

In order to obtain the density of states $N(\omega)/N_0$, we need to analytically continue the host Green's function $\mathbf{G}(i\omega_n)$ to the retarded Green's function $\mathbf{G}_R(\omega)$; i.e., we need to find the functions $\Delta(\omega)$ and $Z(\omega)$ from the solutions of Eq. (3.21) and Eq. (3.22). Given the solutions $\Delta(i\omega_n)$ and $Z(i\omega_n)$ of Eq. (3.11) and Eq. (3.12), Marsiglio *et al.* [14] presented a formally exact analytic continuation method to obtain $\Delta(\omega)$ and $Z(\omega)$. We apply this method to our problem including the impurity contributions.

Here we present a Freericks's [56] alternative derivation for the formally exact analytic continuation method. From Eq. (3.13) and Eq. (3.20), we have the self-energy $\mathbf{\Sigma}(i\omega_n)$ in Matsubara frequencies

$$\mathbf{\Sigma}(i\omega_n) = cV^2\mathbf{G}_d(i\omega_n) - \frac{T}{N_0}\sum_{m=-\infty}^{\infty}\int_{-\infty}^{\infty} dz \frac{\alpha^2 F(z)}{i\omega_n - i\omega_m - z}\boldsymbol{\tau}_3\mathbf{G}(i\omega_m)\boldsymbol{\tau}_3 \,. \qquad (3.30)$$

The retarded function $\mathbf{\Sigma}(\omega)$ is obtained by replacing $\mathbf{G}_d(i\omega_n)$ by the retarded impurity Green's function $\mathbf{G}_d(\omega)$ from Eq. (3.29), $i\omega_n$ by $\omega + i\eta$ and $\mathbf{G}$ by $\mathbf{G}_R$:

$$\mathbf{\Sigma}(\omega) = cV^2\mathbf{G}_d(\omega) - \frac{T}{N_0}\sum_{m=-\infty}^{\infty}\int_{-\infty}^{\infty} dz \frac{\alpha^2 F(z)}{\omega - i\omega_m - z + i\eta}\boldsymbol{\tau}_3\mathbf{G}_R(i\omega_m)\boldsymbol{\tau}_3 + \mathbf{h}(\omega) \,. \qquad (3.31)$$

Note that the matrix function $\mathbf{h}(\omega)$ is introduced so that the properties of the retarded function $\mathbf{\Sigma}(\omega)$ are satisfied, and this analytic continuation is guaranteed to be unique by a theorem of Baym and Mermin [57]; i.e., We know that the retarded function $\mathbf{\Sigma}(\omega)$ is an analytic function in the upper half plane, so we must choose $\mathbf{h}(\omega)$ to cancel the poles in $\mathbf{\Sigma}(\omega)$ at $\omega = z + i\omega_n$. Also $\mathbf{h}(\omega)$ must be bounded as $|\omega| \to \infty$ in the upper half plane and $\mathbf{h}(i\omega_n) = 0$.

Consider a function $\frac{1}{2T}\left[\tanh\frac{\omega - z}{2T} + \coth\frac{z}{2T}\right]$, which has poles at $\omega = z + i\omega_m$ with unit residue. It also vanishes when $\omega = i\omega_m$. Therefore we can construct $\mathbf{h}(\omega)$ with this function; i.e.,

$$\mathbf{h}(\omega) = \frac{1}{2N_0}\int_{-\infty}^{\infty} dz \alpha^2 F(z)\boldsymbol{\tau}_3\mathbf{G}_R(\omega - z + i\eta)\boldsymbol{\tau}_3\left[\tanh\frac{\omega - z}{2T} + \coth\frac{z}{2T}\right] \,, \qquad (3.32)$$

where $\mathbf{G}_R(\omega)$ is given by, similarly in Eq. (C.12),

$$\begin{aligned}\mathbf{G}_R(\omega) &= N_0 \int_{-\infty}^{\infty} d\epsilon [\omega Z(\omega)\mathbf{I} - \epsilon\boldsymbol{\tau}_3 - \phi(\omega)\boldsymbol{\tau}_1 + i\eta]^{-1} \\ &= -i\pi N_0 \frac{\omega\mathbf{I} + \Delta(\omega)\boldsymbol{\tau}_1}{\sqrt{\omega^2 - \Delta^2(\omega)}}. \end{aligned} \tag{3.33}$$

Thus we obtain the retarded function $\boldsymbol{\Sigma}(\omega)$:

$$\begin{aligned}\boldsymbol{\Sigma}(\omega) = cV^2\mathbf{G}_d(\omega) + \frac{T}{N_0}\sum_{m=-\infty}^{\infty} \lambda(\omega - i\omega_m)\boldsymbol{\tau}_3\mathbf{G}(i\omega_m)\boldsymbol{\tau}_3 \\ + \frac{1}{2N_0}\int_{-\infty}^{\infty} dz\alpha^2 F(z)\boldsymbol{\tau}_3\mathbf{G}_R(\omega - z + i\eta)\boldsymbol{\tau}_3 \left[\tanh\frac{\omega - z}{2T} + \coth\frac{z}{2T}\right]. \end{aligned} \tag{3.34}$$

Therefore we have self-consistent equations for $\Delta(\omega)$ and $Z(\omega)$ from Eq. (3.34) in the same way as we obtain the Eliashberg equations in Appendix C:

$$Z(\omega) = 1 - \frac{cV^2[\mathbf{G}_d(\omega)]_{11}}{\omega} + \frac{i\pi T}{\omega} \sum_{n=-\infty}^{\infty} \lambda(\omega - i\omega_n) \frac{\omega_n}{\sqrt{\omega_n^2 + \Delta^2(i\omega_n)}}$$
$$+ \frac{i\pi}{2\omega} \int_{-\infty}^{\infty} dz \frac{\alpha^2 F(z)(\omega - z)}{\sqrt{(\omega - z)^2 - \Delta^2(\omega - z)]}} \left[\tanh \frac{\omega - z}{2T} + \coth \frac{z}{2T}\right] \qquad (3.35)$$

and

$$\Delta(\omega) Z(\omega) = -cV^2[\mathbf{G}_d(\omega)]_{12} + \pi T \sum_{n=-\infty}^{\infty} \lambda(\omega - i\omega_n) \frac{\Delta(i\omega_n)}{\sqrt{\omega_n^2 + \Delta^2(i\omega_n)}}$$
$$+ \frac{i\pi}{2} \int_{-\infty}^{\infty} dz \frac{\alpha^2 F(z)\Delta(\omega - z)}{\sqrt{(\omega - z)^2 - \Delta^2(\omega - z)}} \left[\tanh \frac{\omega - z}{2T} + \coth \frac{z}{2T}\right] \qquad (3.36)$$

with

$$\lambda(\omega) = - \int_{-\infty}^{\infty} d\omega' \frac{\alpha^2 F(\omega')}{\omega - \omega' + i\eta} \,. \qquad (3.37)$$

We solve these self-consistent equations to obtain $\Delta(\omega)$ and $Z(\omega)$ from $\Delta(i\omega_n)$ and $Z(i\omega_n)$ which are the solutions of Eq. (3.21) and Eq. (3.22), and from $\mathbf{G}_d(\omega)$ in the analytic continuation of $\mathbf{G}_d(i\omega_n)$ by the MEM. However, note that Eqs. (3.35) and (3.36) have singularities in the integrations, which should be taken care of properly [56] in the numerical calculations.

The integrations in Eqs. (3.35) and (3.36) have the following form:

$$\int_{-\infty}^{\infty} dz \alpha^2 F(\omega - z) \mathbf{G}_R(z) \left[\tanh \frac{z}{2T} + \coth \frac{\omega - z}{2T} \right] , \tag{3.38}$$

where $\mathbf{G}_R(z)$ has a singularity in the form of $1/\sqrt{z^2 - \Delta^2(z)}$. If we define the gap parameter Δ_0 in the same way as in the pure superconductors, i.e.,

$$\Delta_0 = \mathrm{Re}[\Delta(\Delta_0)] , \tag{3.39}$$

then, for instance, for pure superconductors $\mathbf{G}_R(z)$ has a singularity when $z \leq |\Delta_0|$.

This singularity may be removed by the following mapping:

$$\begin{cases} z = \Delta_0 \sin\theta \quad \text{for } z \leq |\Delta_0| \\ z = \Delta_0 \sec\theta \quad \text{for } z > |\Delta_0| . \end{cases} \tag{3.40}$$

Then Eq. (3.38) becomes

$$
\begin{aligned}
&\int_0^{\pi/2} d\theta \left\{ \frac{\alpha^2 F(\omega - \Delta_0 \sin\theta)\tilde{\mathbf{G}}_R(\Delta_0 \sin\theta)\left[\tanh\frac{\Delta_0\sin\theta}{2T} + \coth\frac{\omega-\Delta_0\sin\theta}{2T}\right]}{i\sqrt{1+\frac{\Delta^2(\Delta_0\sin\theta)-\Delta_0^2}{\Delta_0^2\cos^2\theta}}} \right. \\
&\qquad\qquad\qquad \left. + (\Delta_0 \to -\Delta_0) \vphantom{\frac{a}{b}} \right\} \\
&+ \int_0^{\pi/2} d\theta \sec\theta \left\{ \frac{\alpha^2 F(\omega - \Delta_0 \sec\theta)\tilde{\mathbf{G}}_R(\Delta_0 \sec\theta)\left[\tanh\frac{\Delta_0\sec\theta}{2T} + \coth\frac{\omega-\Delta_0\sec\theta}{2T}\right]}{\sqrt{1-\frac{\Delta^2(\Delta_0\sin\theta)-\Delta_0^2}{\Delta_0^2\tan^2\theta}}} \right. \\
&\qquad\qquad\qquad \left. + (\Delta_0 \to -\Delta_0) \vphantom{\frac{a}{b}} \right\}, \qquad (3.41)
\end{aligned}
$$

where $\tilde{\mathbf{G}}_R(z) = \sqrt{z^2 - \Delta^2}\mathbf{G}_R$ and $\Delta_0 \to -\Delta_0$ denotes that for the second part in the parenthesis $-\Delta_0$ should be substituted instead of Δ_0 in the first part. Thus we can evaluate the integration numerically without difficulties in the form of Eq. (3.41).

Once we obtain $\Delta(\omega)$ and $Z(\omega)$ from Eq. (3.35) and Eq. (3.36), then the superconducting density of states $N(\omega)/N_0$ is readily obtained from Eq. (3.14).

3.5 Results

3.5.1 Pure Host Superconductors ($c = 0$)

First of all we calculate the density of states $N(\omega)/N_0$ and the transition temperature T_{c0} for the pure superconductors given the electron-phonon spectrum function $\alpha^2 F(\omega)$

in Eq. (3.23) for the various values of $\lambda(0)$, ω_0 and ω_L. Through this procedure, we examine the formally exact analytic continuation method [14] and determine a set of parameters for the dilute magnetic alloy superconductors. From this analysis of the results, we will be also able to distinguish the effect of the impurities in the dilute magnetic alloy superconductors from the case of the pure superconductors.

For example, when $\lambda(0) = 3.5$, $\omega_0 = 0.75$ and $\omega_L = 0.25$, we obtain $T_{c0} = 0.20$ and we evaluate Δ_{00} as well as the complex functions $\Delta(\omega)$ and $Z(\omega)$. Fig. 3.13 shows the dependence of $\Delta_{00}(T)$ on the temperature. Note that when $T = 0.05$ (solid circle), Δ_{00} is still 95% of the maximum value $\Delta_{00}(0)$. Since the computer time used by the QMC simulation for the dilute magnetic alloy superconductors scales L^3, where L is the number of imaginary time slices (i.e., $\beta = 1/T = L\Delta\tau$), we try to avoid lower temperaure but maintain the superconductivity close at zero temperature given the parameters.

At this temperature, we plot $N(\omega)/N_0$ with the corresponding $\alpha^2F(\omega)$ shifted by Δ_{00}, $\Delta(\omega)$ and $\Sigma_{11}(\omega)$ in Fig. 3.14. Here the diagonal part of the self-energy $\Sigma_{11}(\omega)$ is easily obtained from $Z(\omega)$ by Eq. (C.6). Note that we plot $N(\omega)/N_0$ for only positive frequencies since $N(\omega)$ is symmetric. Within the gap Δ_{00}, we find that $\mathrm{Re}\Delta(\omega) \simeq \Delta_{00}$, $\mathrm{Im}\Delta(\omega) \simeq 0$ and $\mathrm{Im}\Sigma_{11}(\omega) \simeq 0$, which corresponds to the existence of the Cooper pairs and the absence of the quasi-particle excitations. Also the features appearing at high frequencies above Δ_{00} are consistent with the typical properties [2]

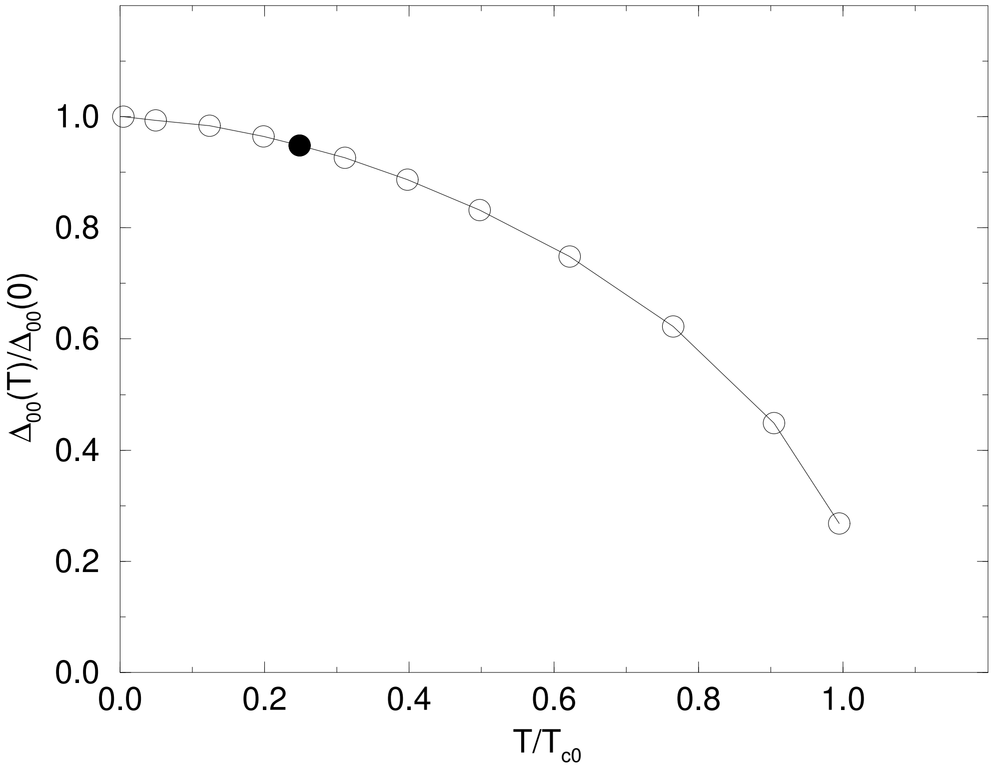

Figure 3.13: $\Delta_{00}(T)/\Delta_{00}(0)$ *vs.* T *when* $\lambda(0) = 3.5$, $\omega_0 = 0.75$, $\omega_L = 0.25$ *and* $T_{c0} = 0.20$. *When* $T = 0.05$ *(solid circle),* Δ_{00} *is 95% of the maximum value* $\Delta_{00}(0)$.

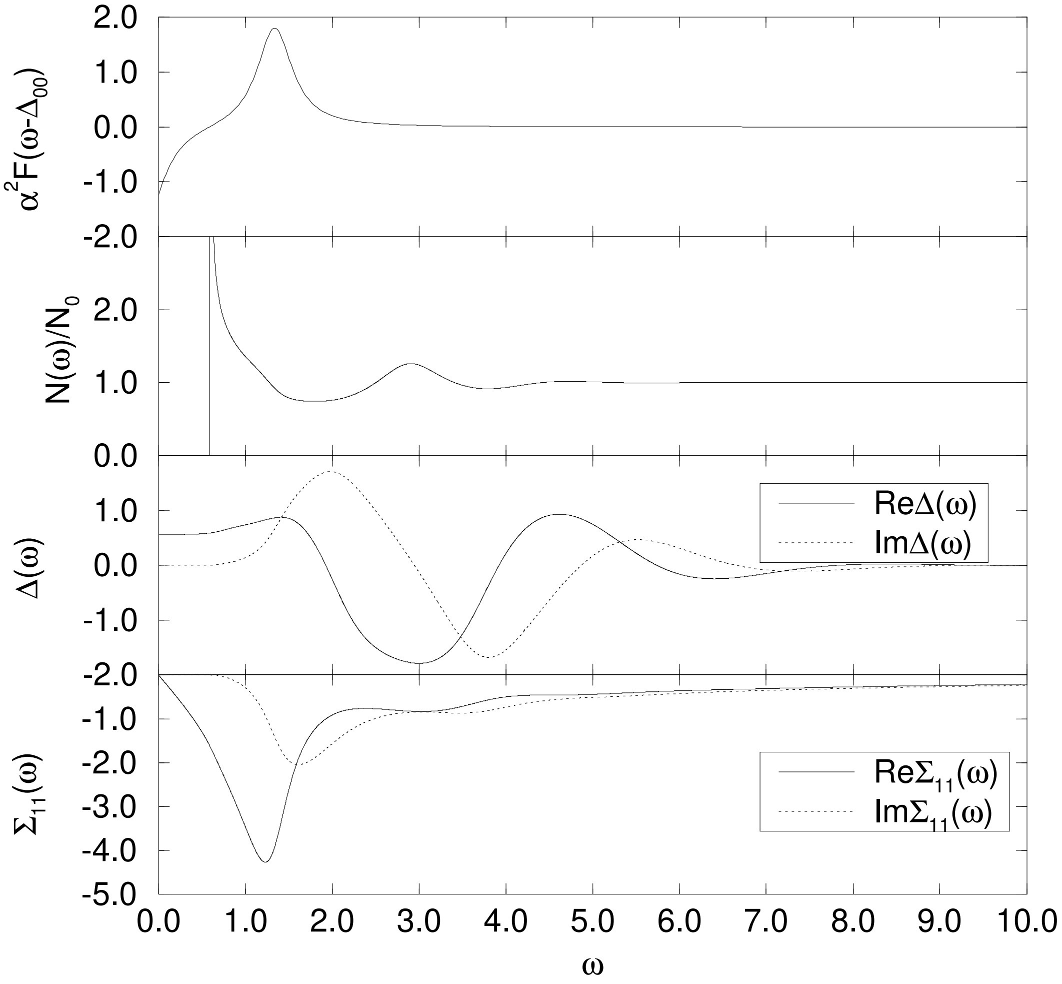

Figure 3.14: $\alpha^2F(\omega - \Delta_{00})$, $N(\omega)/N_0$, $\Delta(\omega)$ *and* $\Sigma_{11}(\omega)$ *for a pure superconductor when* $\lambda(0) = 3.5$, $\omega_0 = 0.75$, $\omega_L = 0.25$ *and* $T = 0.05$. *Here* $T_{c0} = 0.20$ *and* $\Delta_{00} = 0.59$.

of the strong-coupling superconductors associated with the retardation and damping effects of the effective electron-electron interaction.

3.5.2 Parameters

In the self-consistent QMC simulations for the dilute magnetic alloy superconductors, we choose $\Delta\tau = 0.25$ and $\beta = 20$ (i.e., $T = 0.05$). We also choose $2 < U < 10$ with $\Gamma = 0.5$, 1.0 or 1.5 and maintain the measured local moment $\mu^2 \gtrsim 0.75$, where μ^2 is defined by

$$\mu^2 = \langle (n_{d,\uparrow} - n_{d,\downarrow})^2 \rangle \,, \tag{3.42}$$

so that the Kondo temperature T_0 is well defined by Eq. (3.8).

As described in Section 3.5.1, the paremeters for the host superconductors are chosen so that the gap parameter at given temperature is maintained above 90% of the maximum value. Thus, with the given choices for the QMC simulations, we choose relatively large T_{c0} and hence $\lambda(0)$ or ω_0.

3.5.3 Magnetic Impurity Susceptibility $\chi_{\rm imp}$

Now consider a single impurity in a superconductor and the magnetic impurity susceptibility $\chi_{\rm imp}$ defined by

$$\chi_{\rm imp} = \int_0^\beta d\tau \langle [n_{d,\uparrow}(\tau) - n_{d,\downarrow}(\tau)][n_{d,\uparrow}(0) - n_{d,\downarrow}(0)] \rangle \,. \tag{3.43}$$

Since the self-consistency is not required for a single impurity, $\chi_{\rm imp}$ can be obtained easily from the QMC simulation without iterations at different values of temperature. Again we choose $T_{c0} = 0.20$ with $\lambda(0) = 3.5$, $\omega_0 = 0.75$ and $\omega_L = 0.25$.

First we study the universality of $\chi_{\rm imp}$ for the parameters Γ and U. Fig. 3.15 shows our results with the Krishna-murthy's NRG result [40] for a normal magnetic alloy case. For the values of Γ used 0.5 and 1.0 with different values of U given T_0. We obtain $\chi_{\rm imp}$ at various values of temperature below T_{c0} given the parameters for T_0. It is shown that $\chi_{\rm imp}$ is universal like a normal magnetic alloy case, but it is also a function of T/T_{c0}; i.e., as expected, $\chi_{\rm imp}$ is a function of both T/T_0 and T/T_{c0}, but still universal for the parameters Γ and U.

We may also infer the form of $\chi_{\rm imp}$ for small T based on Matsuura's [52] observation regarding the crossover between a doublet and a singlet ground state. Fig. 3.16 shows the schematic representation of the the ground state and the first excited state (gap state) for two different cases, where "$\uparrow$ or $\downarrow$" denotes the doublet state and "$\emptyset$"

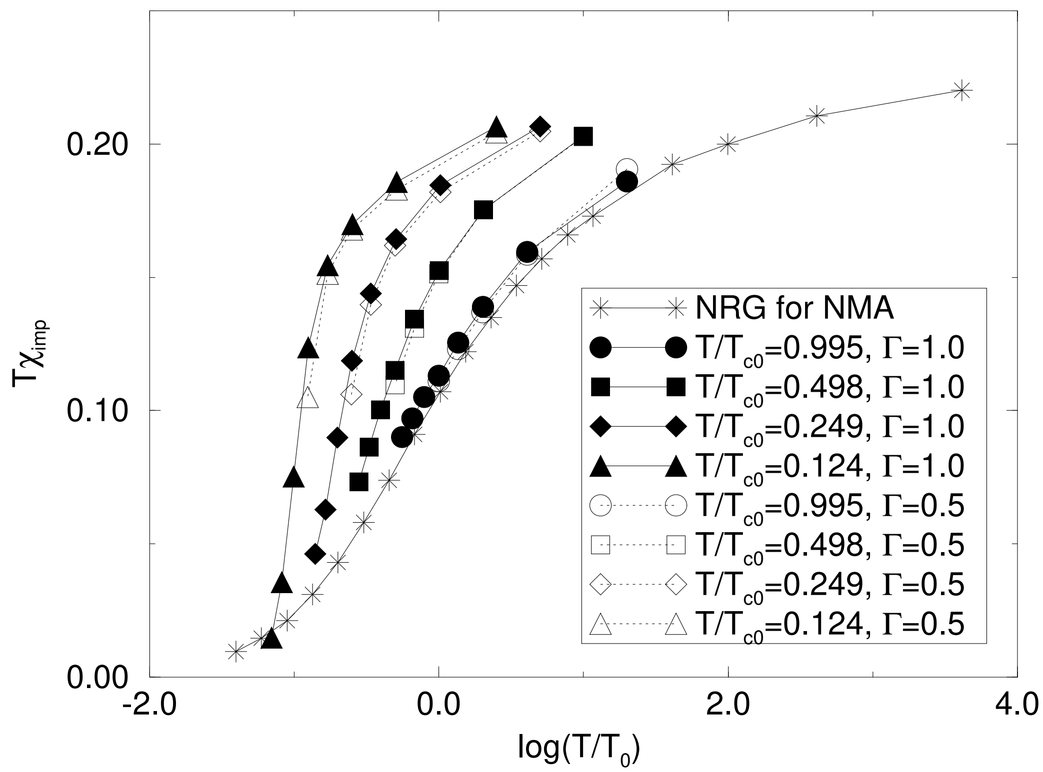

Figure 3.15: *Universality of the magnetic impurity susceptibility* $\chi_{\rm imp}$. *Here the star(*)-solid line is obtained from the Krishna-murthy's NRG result [40] for a Normal Magnetic Alloy (NMA) case.*

singlet. Here δ is the energy difference between the ground state and the gap state. Thus we obtain χ_{imp}^{-1} for small T from this configuration:

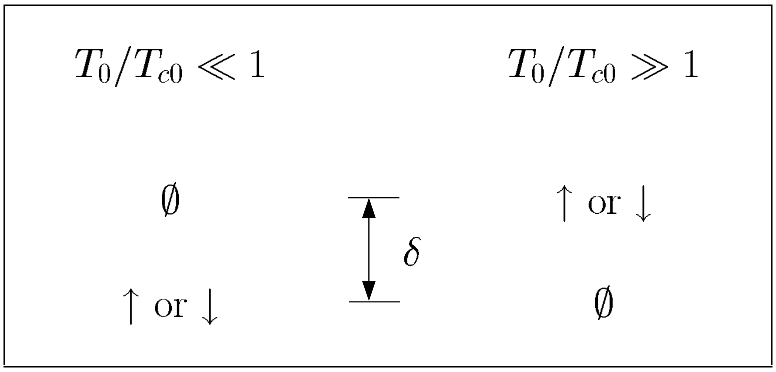

Figure 3.16: *Schematic representation of the the ground state and the first excited state (gap state) for $T_0/T_{c0} \ll 1$ and $T_0/T_{c0} \gg 1$. Here "$\uparrow$ or $\downarrow$" denotes the doublet state and "$\emptyset$" the singlet. Also δ is the energy difference between the ground state and the gap state.*

$$\lim_{T\to 0} \chi_{\text{imp}}^{-1} \approx \begin{cases} T & \text{for a doublet ground state} \\ Te^{\delta/T} & \text{for a singlet ground state} \end{cases} . \tag{3.44}$$

Meanwhile, our QMC results for $\chi_{\text{imp}}^{-1}(T)$ are shown in Fig. 3.17 for various values of T_0/T_{c0}. With extrapolation to $T \to 0$, χ_{imp}^{-1} has zero intercepts when $T_0/T_{c0} \lesssim 1$ (the open symbols) but not when $T_0/T_{c0} \gtrsim 1$ (the filled symbols). With Eq. (3.44), this implies that the doublet ground state is favorable for $T_0/T_{c0} \lesssim 1$ and singlet for $T_0/T_{c0} \gtrsim 1$. It should be possible to see this behavior in NMR measurements of $1/T_2 \propto \chi_{\text{imp}}$.

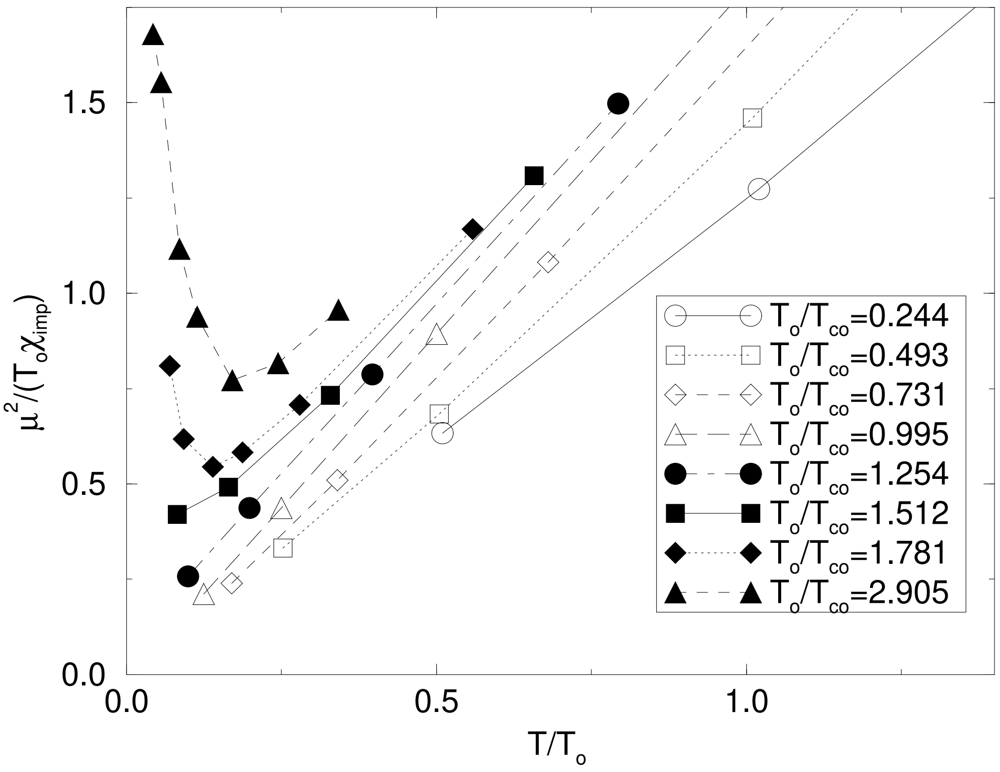

Figure 3.17: *The inverse magnetic impurity susceptibility* χ_{imp}^{-1} *vs.* T/T_0 *for various values of* T_0/T_{c0}. χ_{imp}^{-1} *is normalized with the magnetic moment* μ^2 *and* T_0.

3.5.4 Impurity Spectral Function $\mathbf{A}(\omega)$

Here we present the impurity spectral function, $\mathbf{A}(\omega) = -\frac{1}{\pi}\mathrm{Im}\mathbf{G}_d(\omega)$, obtained by MEM (see Section 3.4.1). In Fig. 3.18, we plot $\mathbf{A}(\omega)$ both for a single impurity embedded in a normal metal ($T_{c0} = 0.0$) and for one in a superconductor ($T_{c0} = 0.2$), when $T = 0.05$ and $T_0 = 0.05$ with $\Gamma = 0.5$ and $U = 4.09$.

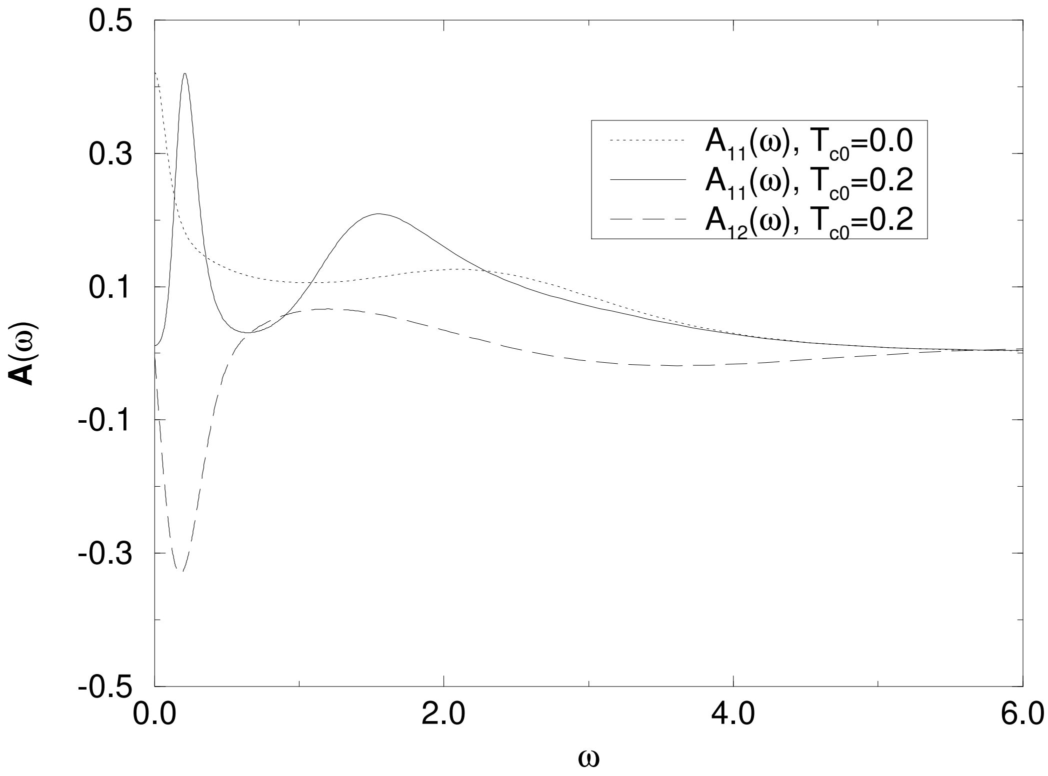

Figure 3.18: *The spectral function,* $\mathbf{A}(\omega) = -\frac{1}{\pi}Im\mathbf{G}_d(\omega)$*, both for a single impurity embedded in a normal metal (*$T_{c0} = 0.0$*) and for one in a superconductor (*$T_{c0} = 0.2$*), when* $T = 0.05$ *and* $T_0 = 0.05$ *with* $\Gamma = 0.5$ *and* $U = 4.09$*.*

For the single impurity embedded in a metallic host, $A_{11}(\omega)$ (dotted line) has a central peak at $\omega = 0$ associated with Kondo resonance and a high-frequency peak associated with charge transfer on the impurity site, while $A_{12}(\omega) = 0$. In a superconducting host, however, a gap may open in $A_{11}(\omega)$ as shown in Fig. 3.18 (solid line). The reason is that within the superconducting gap Δ_{00} the conduction electrons form Cooper pairs, and the pair-breaking process would cost an energy associated with δ. Thus for a finite δ a gap is developed. Also note that $A_{12}(\omega)$ has a peak associated with the first peak in $A_{11}(\omega)$, as shown in Fig. 3.18 (dashed line).

However, we also found that, when $T_0 \gtrsim T_{c0}$ (Fig. 3.19), $A_{12}(\omega)$ has opposite sign from when $T_0 \lesssim T_{c0}$ (Fig. 3.18), while it becomes zero through $T_0 \sim T_{c0}$. Fig. 3.19 shows $\mathbf{A}(\omega)$ for $T_0 \gtrsim T_{c0}$, where we have chosen $T = 0.05$, $T_{c0} = 0.2$ and $T_0 = 0.58$ with $\Gamma = 1.5$ and $U = 6.46$. We will discuss the effect of this sign change of $A_{12}(\omega)$ in Section 3.5.7

3.5.5 Superconducting Density of States $N(\omega)/N_0$

When the concentration of the impurities is small but finite, their effects can be seen in the dynamics of the problem. As a result, before further study in detail, we present the superconducting density of states for various values of T_0/T_{c0} in Fig. 3.20. Here we have chosen $c^* = c/[(2\pi)^2 N_0 T_{c0}] = 0.03$, $T = 0.05$ and $T_{c0} = 0.20$ with $\lambda(0) = 3.5$,

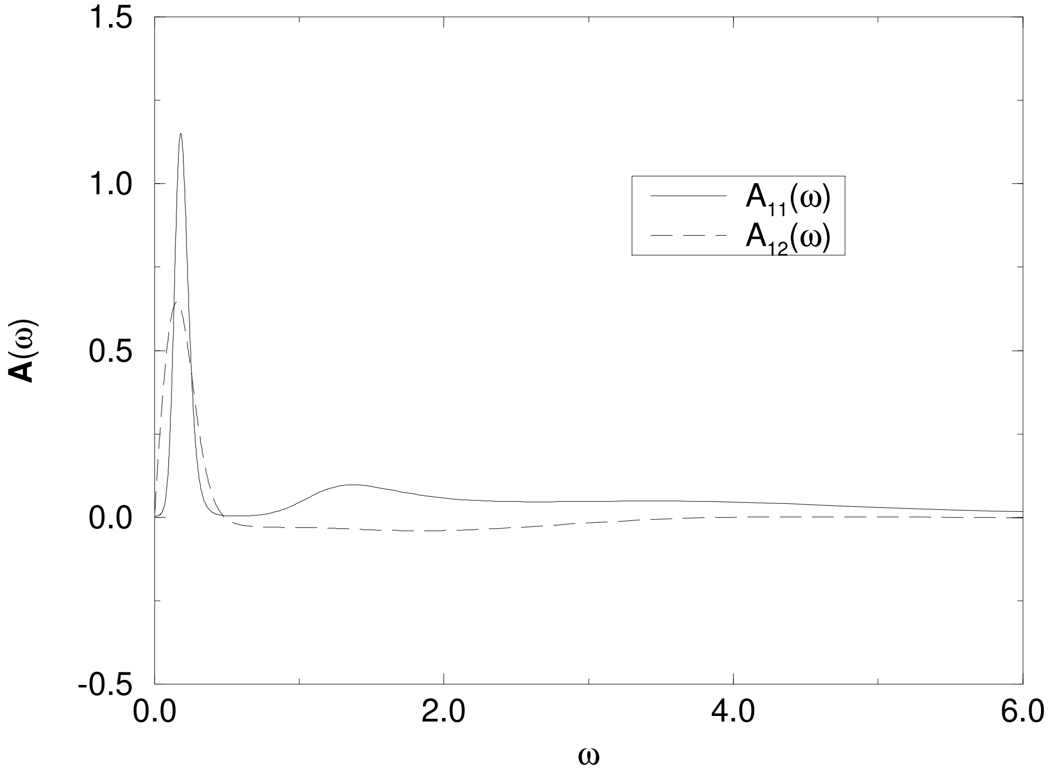

Figure 3.19: *The spectral function* $\mathbf{A}(\omega)$ *for* $T_0 \gtrsim T_{c0}$*, where* $T = 0.05$*,* $T_{c0} = 0.2$ *and* $T_0 = 0.58$ *with* $\Gamma = 1.5$ *and* $U = 6.46$*.*

$\omega_0 = 0.75$ and $\omega_L = 0.25$. Also the energy is scaled by the gap parameter Δ_{00} of the pure superconductor.

As shown in Fig. 3.20, for energies above the gap the phonon induced structure in the density of states is the same as for the pure superconductor (dotted line) but there is also structure in the gap. As T_0 increases through T_{c0}, the gap states move toward the center of the gap and move back to the gap edge. At $T_0/T_{c0} \simeq 1$, the gap states form at the center of the gap as expected from the study in Section 3.5.3; i.e., at $T_0/T_{c0} \simeq 1$, the crossover between doublet and singlet ground state occurs, so $\delta = 0$. Then due to this degeneracy, the pair-breaking rate by the magnetic impurities would be largest at $T_0/T_{c0} \simeq 1$. Also notice that the gap Δ_0 and the integrated weight of the gap states change with T_0/T_{c0}. In the following sections, we will discuss these problems in detail.

3.5.6 Location of the Gap States y

Before we study the location of the gap states as a function of T_0/T_{c0}, we examine the universality of the location of the gap states for different parameters given T_0/T_{c0}. Here the location δ of the gap states is measured by the energy difference between the center of the gap and the peak of the gap states. Then we normalize δ by Δ_0; i.e., $y = \delta/\Delta_0$.

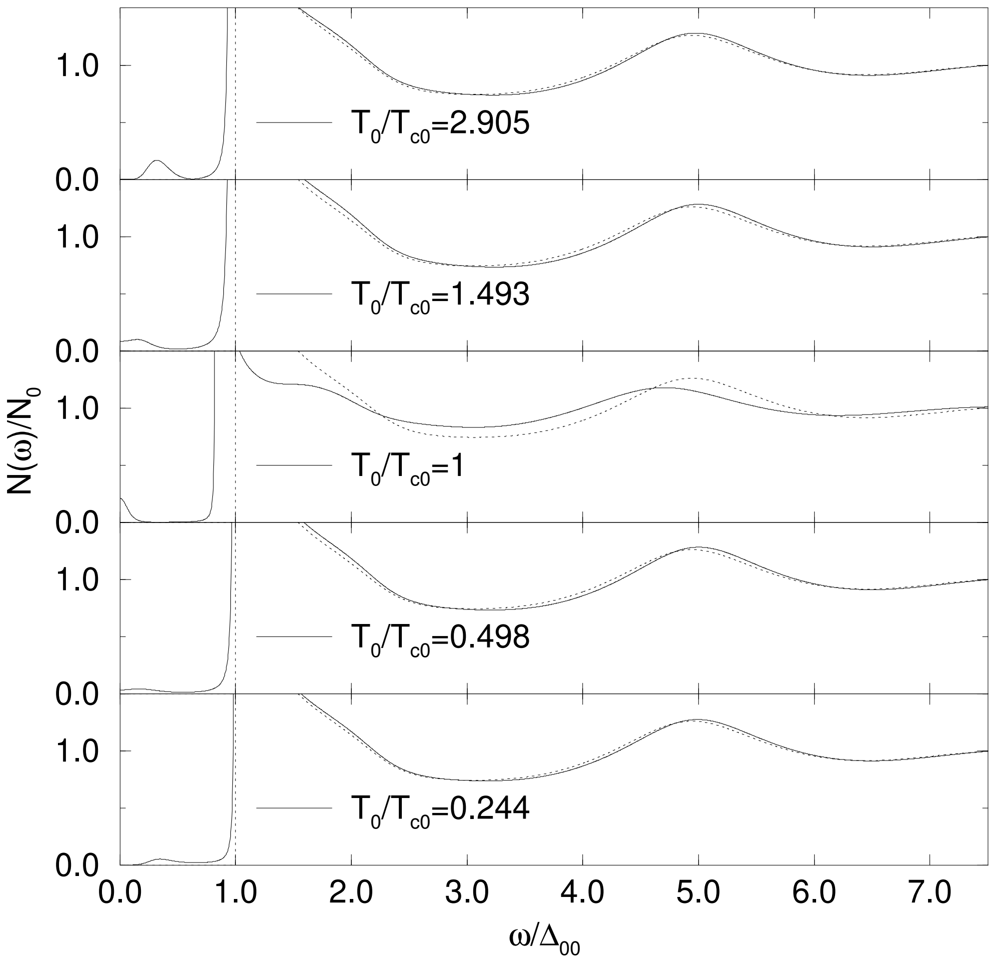

Figure 3.20: *Superconducting density of states $N(\omega)/N_0$ for various values of T_0/T_{c0} when $c^* = c/[(2\pi)^2 N_0 T_{c0}] = 0.03$. Since $N(\omega)$ is symmetric, only positive frequencies are plotted. The dotted line is for the pure superconductor with $T_{c0} = 0.20$ and $T = 0.05$. Δ_{00} is the superconducting gap parameter for the pure superconductor.*

In Fig. 3.21, we plot the gap states for different values of Γ and U, while fixed values of T_0 and parameters for the host. Even though the gap states are broaden for large value of Γ, Fig. 3.21 clearly shows the universality of y for Γ and U within the numerical errors.

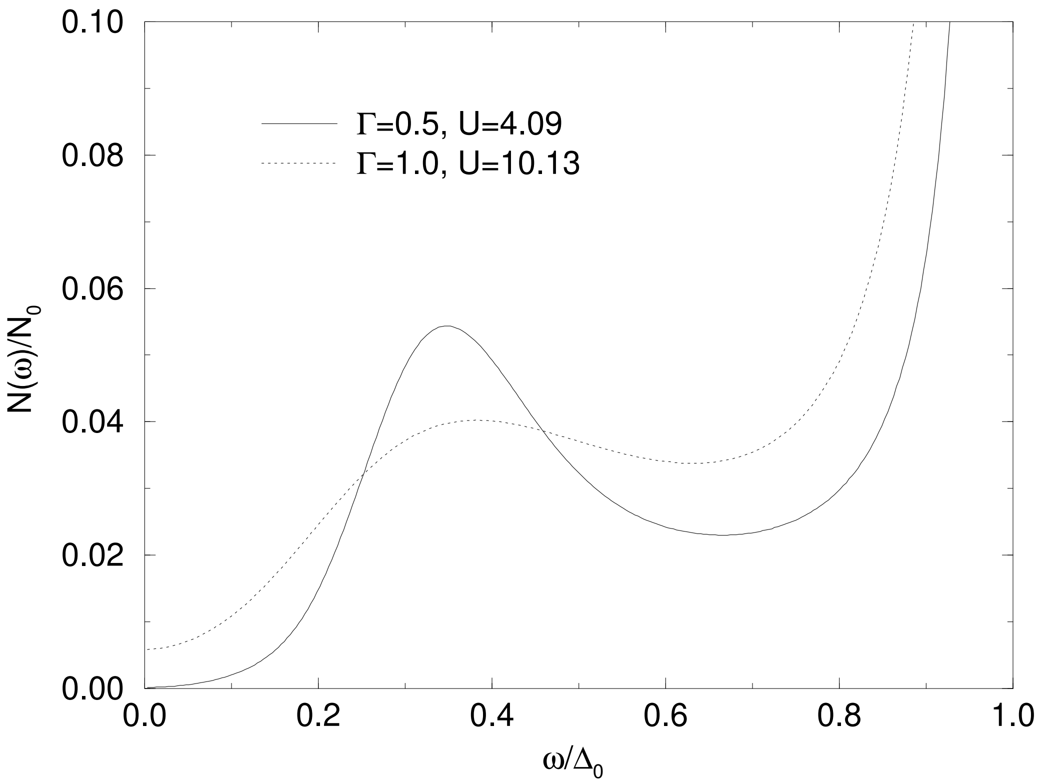

Figure 3.21: *Gap states for different values of* Γ *and* U *when* $T_0 = 0.50$, $T_{c0} = 0.2$ *and* $c^* = 0.03$.

Now examine the universality of y for $\lambda(0)$ and ω_0. In Fig. 3.22, we plot the gap states for different values of $\lambda(0)$ and ω_0 while fixed values of T_0 and T_{c0}. Again y is universal for different values of $\lambda(0)$ and ω_0 within numerical errors. But also note that the integrated weight of the gap states is increasing with decreasing $\lambda(0)$.

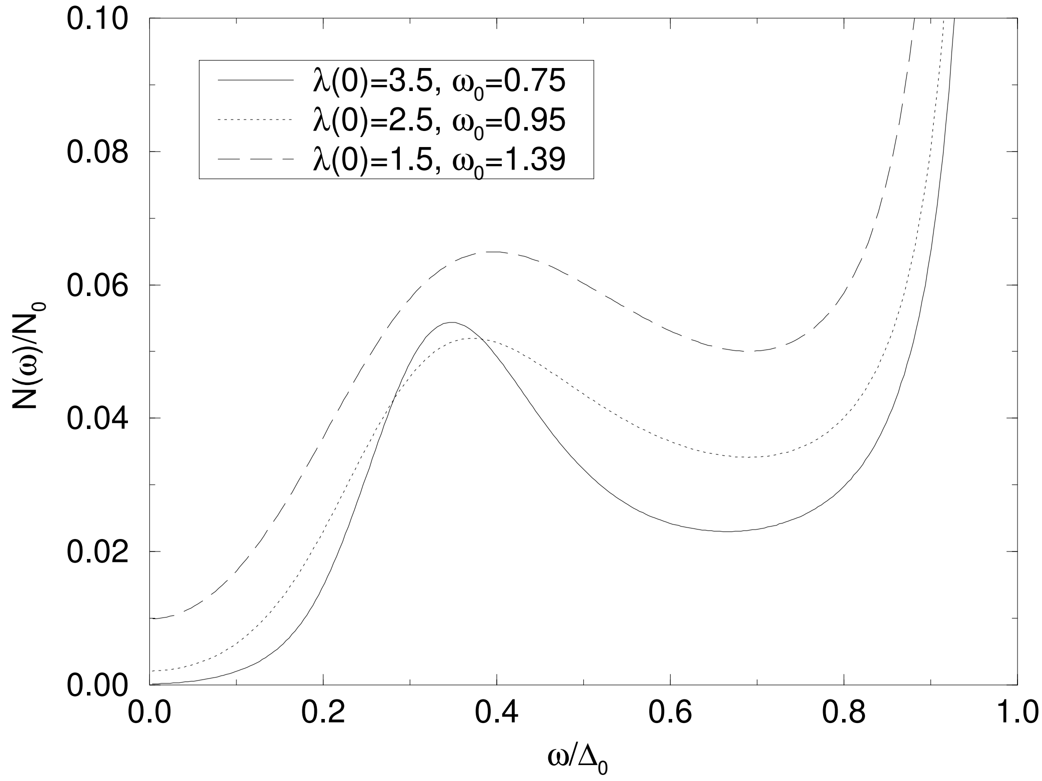

Figure 3.22: *Gap states for different values of* $\lambda(0)$ *and* ω_0 *when* $T_0 = 0.50$, $T_{c0} = 0.2$ *and* $c^* = 0.03$.

Fig. 3.23 shows the normalized location y of gap states for various values of T_0/T_{c0} and the corresponding ZBM [50] results[1] (see Eq. (3.16) and Fig. 3.9). There is a much better fit if we use T_0 instead of T_K in their formula. This is, in fact, the

[1]Here we show their results for only $T = T_{c0}$ limit. Their results for $T = 0$ limit have much more deviation quantitatively from our results.

parameterization chosen when their formula was fit to different experiments [47]. Even so, for $T_0/T_{c0} \lesssim 1$, the gap states move faster than ZBM's as a function of T_0/T_{c0}, which also agrees with experiments [47]. Note that multiple points appear in

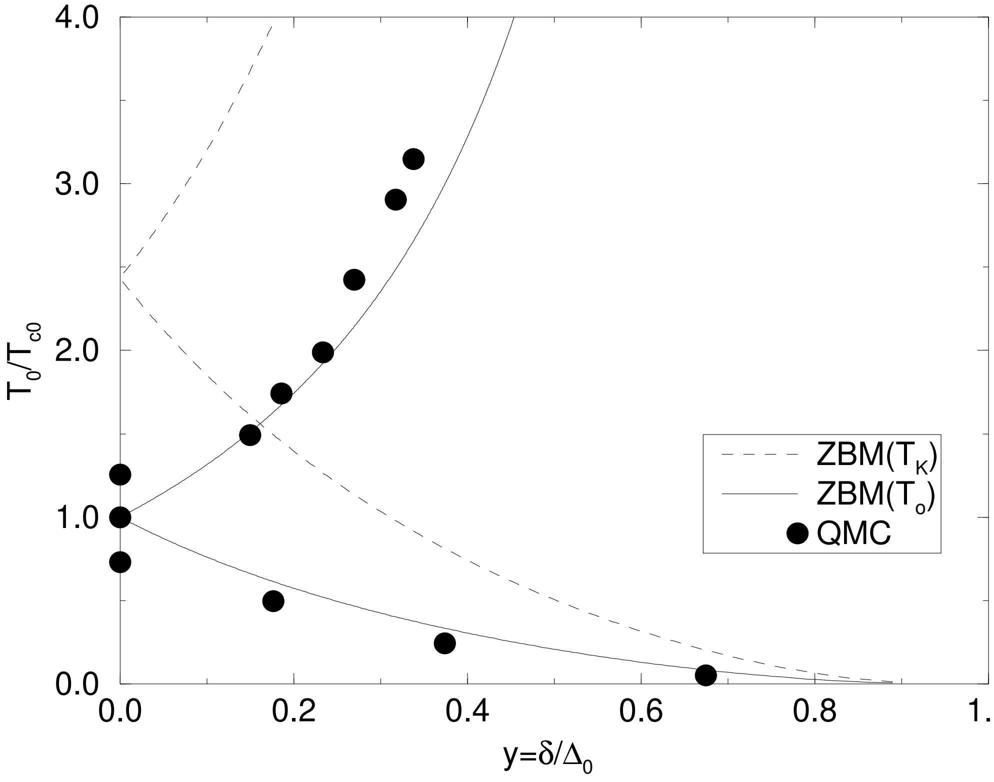

Figure 3.23: *Normalized location of gap states, $y = \delta/\Delta_0$, for various values of T_0/T_{c0} when $c^* = c/[(2\pi)^2 N_0 T_{c0}] = 0.01$. δ is the energy difference between the center of the gap and the peak of the gap states, and Δ_0 is the superconducting gap parameter. The filled circles are our QMC results. The dashed line is the ZBM result with T_K and the solid line with T_0. Multiple points appear when $y = 0$ since when $T_0 \simeq T_{c0}$ the distributions of gap states for positive and negative ω combine into a single peak centered at $\omega = 0$.*

our results when $y = 0$. The reason is that when $T_0 \simeq T_{c0}$ the distributions of the gap states for positive and negative ω combine into a single peak centered at $\omega = 0$. This would occur even for a single impurity case ($c^* = 0$), since the Kondo resonance peak of $A_{12}(\omega)$ has finite width even for $c^* = 0$ as shown Figs. 3.18, 3.19 and 3.24. Thus we obtain a *intrinsic gapless superconductor* for arbitrarily low concentration

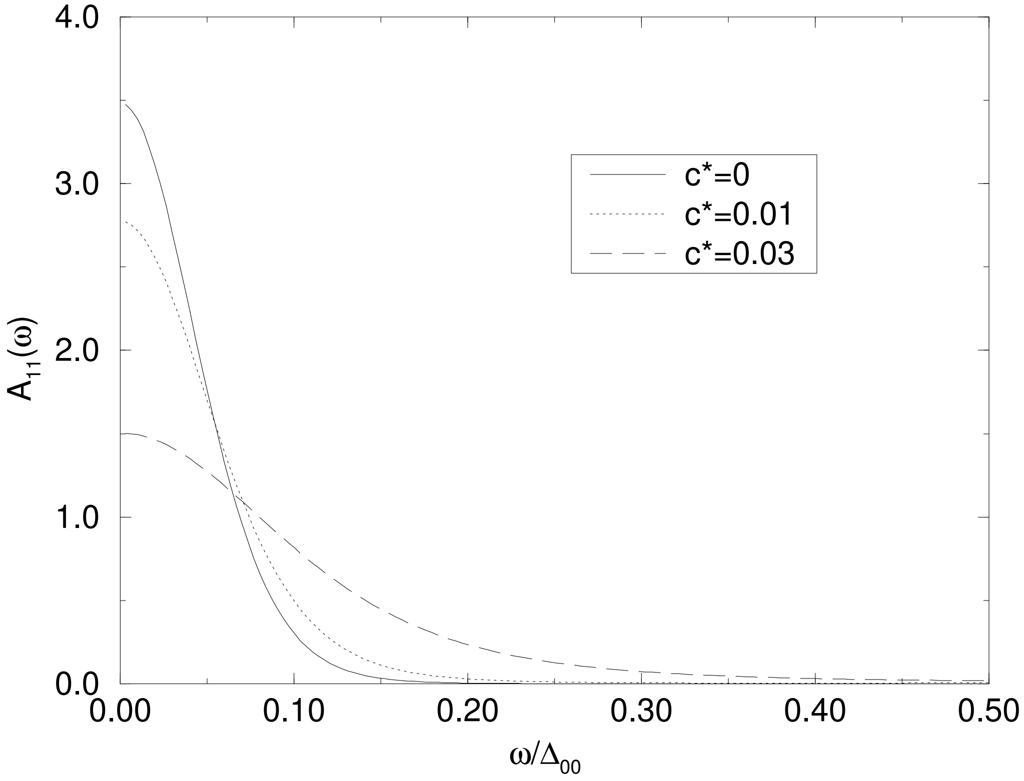

Figure 3.24: *The impurity spectral function* $\mathbf{A}_{11}(\omega)$ *for different values of* c^* *when* $T_0/T_{c0} = 1.254$ *and* $T = 0.05$.

of the impurities when $T_0 \simeq T_{c0}$. This is consistent with ZBM result (even though there is severe quantitative deviation from our results), but is inconsistent with the

NRG result [55], where all states are discrete and it is therefore difficult to represent a resonance of finite width.

3.5.7 Spectral Weight of the Gap States W

Now consider the spectral weight W of the gap states. Fig. 3.25 shows the dependence of the W on c^* for different values of T_0/T_{c0}. We find that W is linearly increases monotonically with c^*, which is consistent with the experiments [47] and the ZBM result.

However, while the location of the gap states is a universal function of T_0/T_{c0}, the spectral weight also depends upon the coupling $\lambda(0)$; i.e., it increases with decreasing $\lambda(0)$ (see Fig. 3.22). A similiar feature was found in calculations of $T_c(c)$ and $(dT_c/dc)_{c=0}$ [58], where both functions always appeared as a function of $1/\lambda(0)$ for small $\lambda(0)$.

Furthermore, as shown in Fig. 3.26, for fixed $\lambda(0)$ the spectral weight of the gap states as a function of T_0/T_{c0} is not constant as one would expect from Eq. (3.17). This is in agreement with the NRG results [55]. In Fig. 3.26, we plotted W/c^* as a function of T_0/T_{c0} from the results for various values of Γ and c^*, and it showes that the weight increases with T_0/T_{c0}.

To understand this increase of $W/c*$ with T_0/T_{c0}, note from Eq. (3.14) that any contribution to $\mathrm{Im}\Delta(\omega)$ at frequencies lower than the gap, will yield states in the

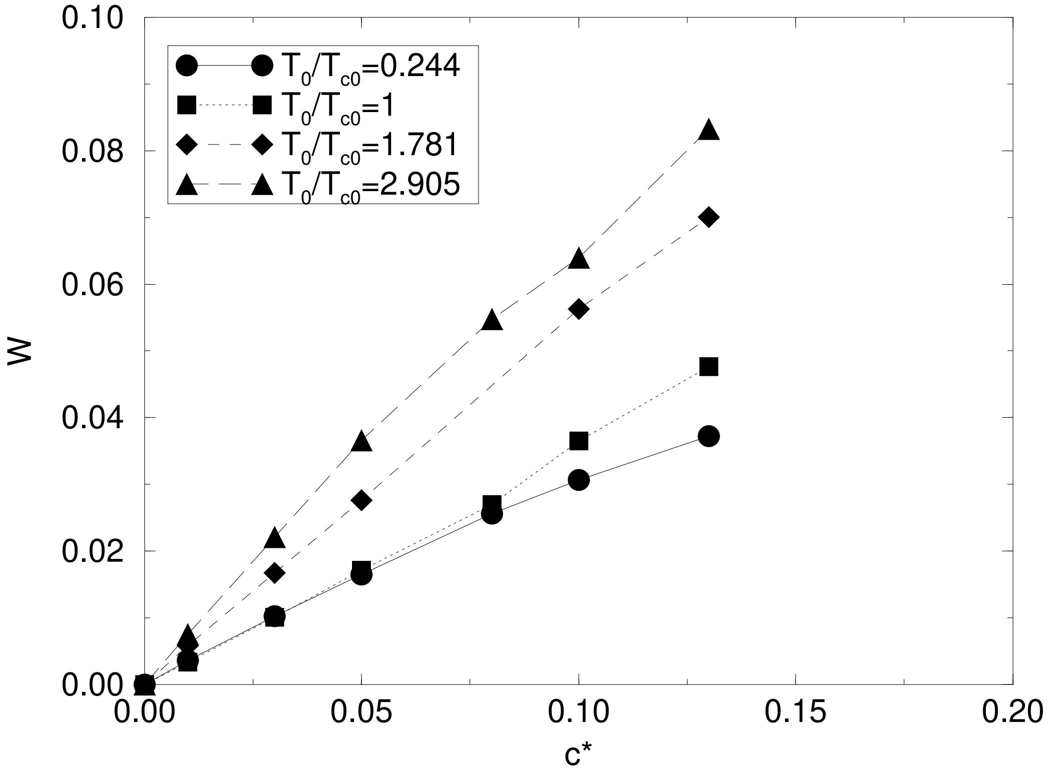

Figure 3.25: *The Spectral weight of the gap states vs.* c^* *for different values of* T_0/T_{c0}.

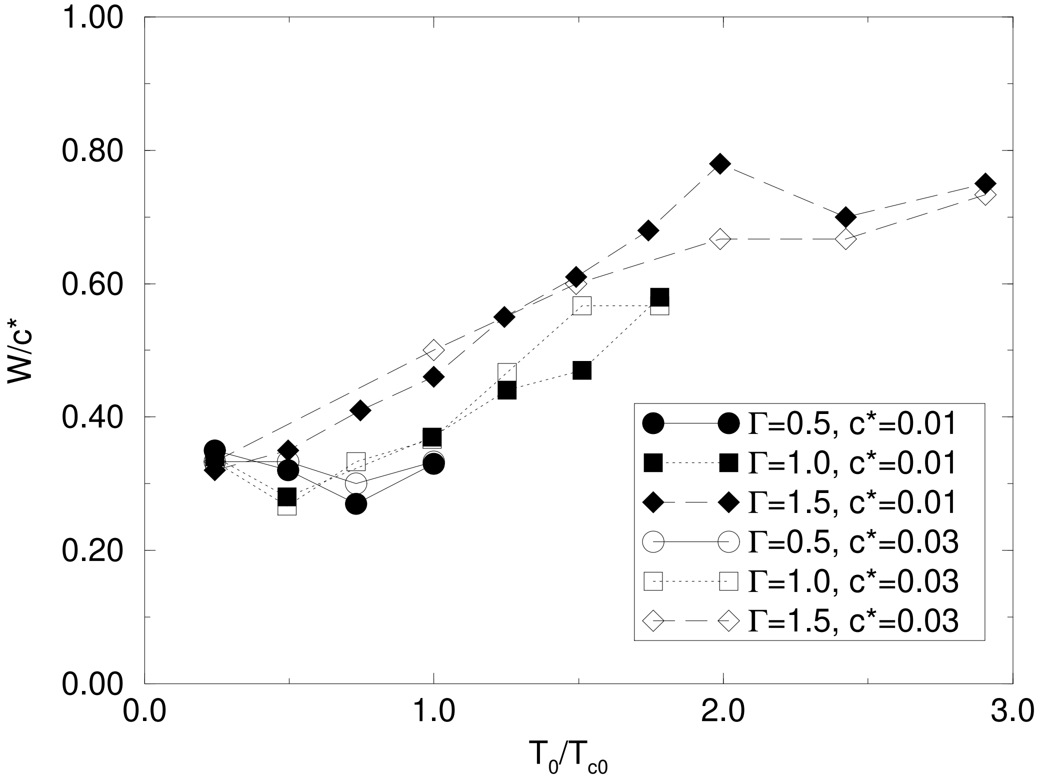

Figure 3.26: *Spectral weight W of the gap states vs. T_0/T_{c0} for different values of Γ and c^*.*

gap, whether this contribution is from the impurity (i.e. $-cV^2[\mathbf{G}_d(\omega)]_{12}$), or the remaining host portion of Eq. (3.36). In Figs. 3.27 and 3.28 we plot both the off-diagonal impurity Green's function $[\mathbf{G}_d(\omega)]_{12}$ and the host $\mathbf{G}_{12}(\omega)$ for $T_0/T_{c0} < 1$ and $T_0/T_{c0} > 1$ each.

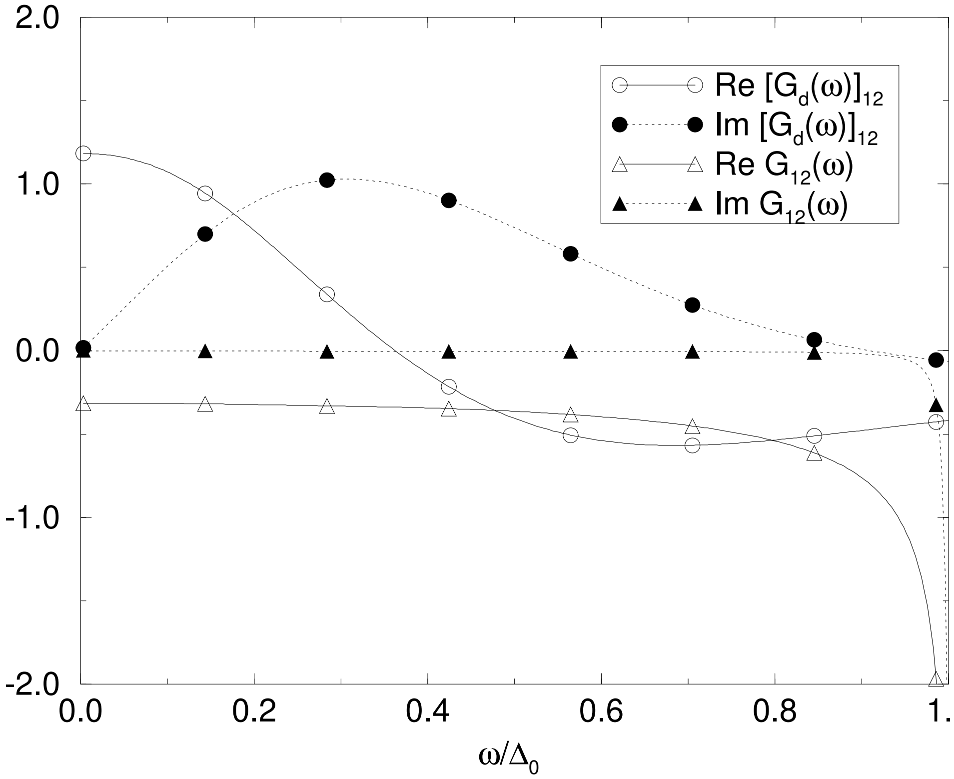

Figure 3.27: *The off-diagonal Green's functions of the impurity ($[\mathbf{G}_d(\omega)]_{12}$) and the host ($[\mathbf{G}(\omega)]_{12}$) when $T_0/T_{c0} = 0.244$.*

At low frequencies when $T_0/T_{c0} < 1$ in Fig. 3.27, both the real and imaginary parts of $[\mathbf{G}_d(\omega)]_{12}$ have opposite sign compared to $\mathbf{G}_{12}(\omega)$; i.e., the real and imaginary parts of the impurity gap function are out of phase with the host result. Hence the

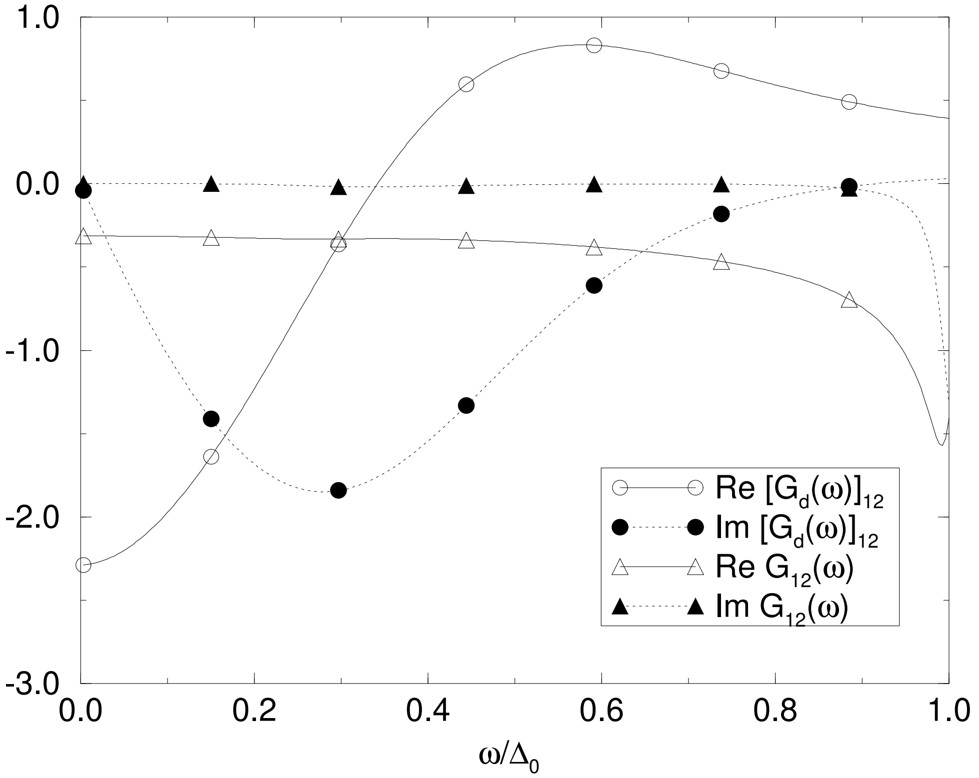

Figure 3.28: *The off-diagonal Green's functions of the impurity ($[\mathbf{G}_d(\omega)]_{12}$) and the host ($[\mathbf{G}(\omega)]_{12}$) when $T_0/T_{c0} = 2.905$.*

impurity and host contributions to the gap states tend to cancel. When $T_0/T_{c0} > 1$ in Fig. 3.28, they have the same sign and tend to add. Thus, when the impurity ground state crosses over from a doublet to a singlet, it is accompanied by a phase shift of the impurity order parameter[2] (see also Section 3.5.4) and an asymmetry in the weight of the gap states.

3.5.8 Gap Parameter Δ_0

As c^* increases, the superconducting gap parameter Δ_0 and the transition temperature T_c for the magnetic alloy superconductors are reduced from the values for the pure superconductor Δ_{00} and T_{c0} respectively. Fig. 3.20 shows that for small c^* the initial reduction of Δ_0 is largest when $T_0/T_{c0} \simeq 1$. In Fig. 3.29, we plot Δ_0/Δ_{00} *vs.* c^* for different values of T_0/T_{c0}. The steepest slope of Δ_0/Δ_{00} is obtained at larger concentration of impurities for $T_0/T_{c0} \lesssim 1$ and at smaller concentration of impurities for $T_0/T_{c0} \gtrsim 1$. This may be understood as follows: For larger c^* the reduction of Δ_0 is again largest for $T_0/T_c \simeq 1$, where T_c is the transition temperature at that value of c^*. When $T_0/T_{c0} < 1$, increasing c^* decreases T_c and thus increases T_0/T_c toward 1, and hence increases the pair-breaking rate. Therefore, when $T_0/T_{c0} < 1$, the curvature of Δ_0/Δ_{00} is initially negative. In the other regime, $T_0/T_{c0} > 1$, the initial curvature of Δ_0/Δ_{00} is positive.

[2]We note that this phase shift may be observable in Josephson tunneling through a magnetic impurity, since the impurity order parameter vanishes when $T_0 \simeq T_{c0}$.

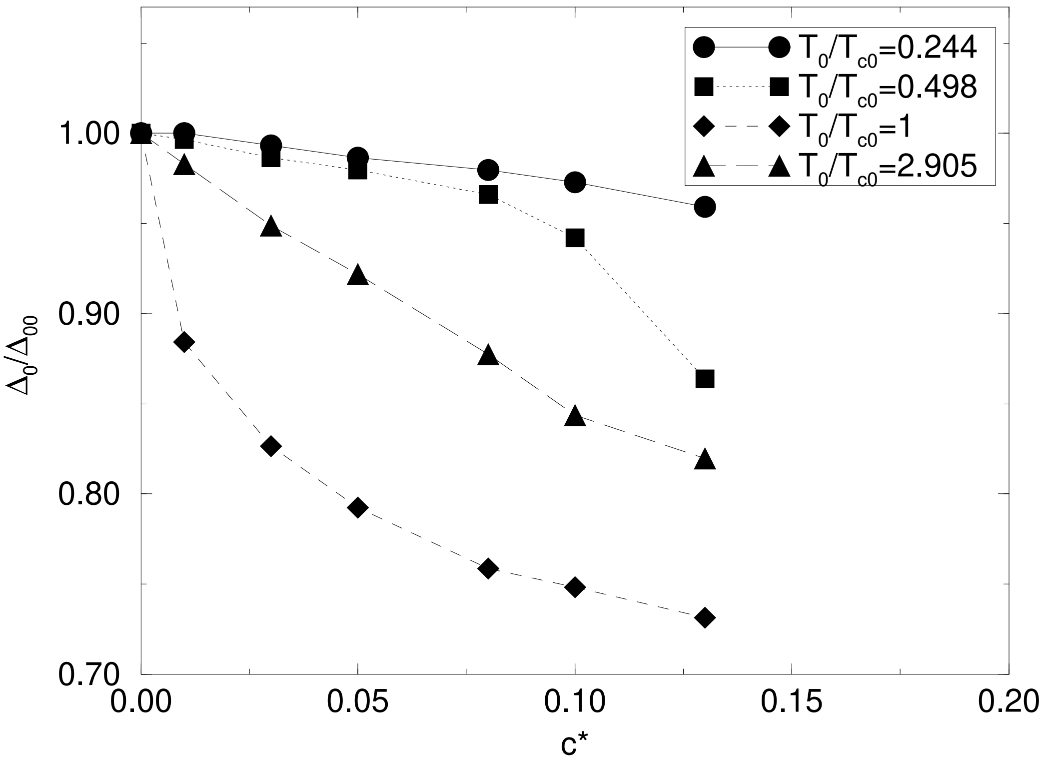

Figure 3.29: Δ_0/Δ_{00} *vs.* c^* *for different values of* T_0/T_{c0}*.* Δ_0 *is the superconducting gap parameter for the magnetic alloy superconductors and* Δ_{00} *is for the pure superconductor when* $T = 0.05$*.*

Note that the maximum initial slope $|(\partial\Delta_0/\partial c)_{c=0}|$ occurs when $T_0 \simeq T_{c0}$, but the maximum initial slope $|(\partial T_c/\partial c)_{c=0}|$ occurs when $T_K \simeq T_{c0}$ [59]. These facts are independent of the coupling strength $\lambda(0)$. This implies that Δ_0 and T_c have different functional forms even to the first order in c; i.e., Δ_0/T_c is not constant.

3.6 Conclusion

We have developed a novel method to study the behavior of the gap states in dilute magnetic alloy superconductors. We used a combination of QMC, MEM and a formally exact analytic continuation method [14]. Since this approach deals with the impurity nonperturbatively and produces the superconducting density of states with fine resolution, we have been able to study the problem systematically. The main results in summary are following:

We calculated the magnetic impurity susceptibility, and notice that it has different characteristics for $T_0 \lesssim T_{c0}$ and $T_0 \gtrsim T_{c0}$ due to the crossover between a doublet and a singlet impurity ground state. As T_0 increases through T_{c0}, the gap states move toward the center of the gap and move back to the gap edge. The gap states form at the center of the gap at T_0 (not T_K) $\simeq T_{c0}$, where the crossover between the doublet and singlet ground state occurs. We also found that there is intrinsic gaplessness for arbitrarily low concentration of the impurities when $T_0 \simeq T_{c0}$. Accompanying the crossover between the doublet and singlet ground state, there is a phase shift of the impurity order parameter. Hence this results in the increase of the spectral weight of the gap states with T_0/T_{c0}. As the concentration of the impurities increases, the superconducting gap parameter Δ_0 is reduced with different curvatures for $T_0 < T_{c0}$ and $T_0 \gtrsim T_{c0}$. We also find that Δ_0/T_c for fixed $\lambda(0)$ is not constant but a function of both the concentration of impurities and T_0/T_{c0} for a dilute magnetic alloy superconductor.

We would like to acknowledge useful discussions with H. Akhlaghpour, J. Deisz, J. R. Engelbrecht, J. K. Freericks, B. Goodman, M. Ma, P. Muzikar, and H. Pang. WC was supported by the Office of Naval Research (ONR N00014-95-1-0883), and MJ by NSF (DMR 94-06678) and the Ohio Supercomputing Center.

Appendix A

The Hybrid Monte Carlo Algorithm

In this appendix, we will detail the Hybrid Quantum Monte Carlo algorithm. Our fundamental objective is to calculate the expectation value of some operator A, $\langle A \rangle = (1/Z)\int D\phi A\{\phi\}e^{-S\{\phi\}}$. In the conventional Monte Carlo procedure, the expectation value of a physical quantity $\langle A \rangle$ is evaluated by generating a sequence of independent configurations of the scalar field ϕ_m, with probability $P\{\phi_m\}$. The computation of the expectation value is approximated by the weighted summation of M independent configurations,

$$\langle A \rangle \approx \bar{A} = \frac{\sum_{m=0}^{M} A\{\phi_m\} P^{-1}\{\phi_m\} e^{-S\{\phi_m\}}}{\sum_{m=0}^{M} P^{-1}\{\phi_m\} e^{-S\{\phi_m\}}}. \tag{A.1}$$

To insure that $P\{\phi_m\}$ converges towards the desired distribution, $e^{-S\{\phi_m\}}$, as the number of sampled configurations goes to infinity, $M \rightarrow \infty$, a Markov process is used for generating the sequence of configurations. A Markov process generates a new point in phase space $\phi_{m'}$ from its predecessor ϕ_m with the transition probability $P\{\phi_m \rightarrow \phi_{m'}\}$. To insure that the Markov process will converge to a unique distribution, it is sufficient to impose the detailed balance condition $P\{\phi_m\}P\{\phi_m \rightarrow \phi_{m'}\} = P\{\phi_{m'}\}P\{\phi_{m'} \rightarrow \phi_m\}$. Accepting the new configuration $\phi_{m'}$ with the acceptance-rejectance probability, P_{ar},

$$P_{ar} = Min(1, P\{\phi_{m'}\}P\{\phi_{m'} \rightarrow \phi_m\}/P\{\phi_m\}P\{\phi_m \rightarrow \phi_{m'}\}) \tag{A.2}$$

or rejecting it and keeping the old configuration ϕ_m, satisfies detailed balance for any transition probability $P\{\phi_m \rightarrow \phi_{m'}\}$.

In the Metropolis procedure, the most natural choice for the probability is made, that is $P\{\phi_m\} \propto e^{-S\{\phi_m\}}$. As commonly employed, the sampling of phase space is diffusive. That is, the proposed configuration of the field variables is generated by making only local, random changes to the fields variables of the present configuration. For this motion of the ϕ fields, the quotient of the transition probabilities is unity, $P\{\phi_{m'} \rightarrow \phi_m\}/P\{\phi_m\}P\{\phi_m \rightarrow \phi_{m'}\} = 1$. This proposed configuration $\{\phi_{m'}\}$ is therefore accepted or rejected with the acceptance-rejectance probability, P_{ar},

$$P_{ar} = Min(1, e^{\delta S}) \tag{A.3}$$

where

$$\delta S \equiv S\{\phi'_m\} - S\{\phi_m\}. \tag{A.4}$$

The computation of the expectation values reduces to the arithmetic average,

$$\langle A \rangle \approx \bar{A} = (1/M) \sum_{m=1}^{M} A\{\phi_m\}. \tag{A.5}$$

Strong correlations can exist between consecutive configurations of the field variables in a diffusive Monte Carlo algorithm. For example, the propagation can become trapped in the vicinity of a local minimum of the action and therefore confine the sampling to a non-representative region of phase space.

In the Hybrid Method, to allow the field variables ϕ to evolve globally, a pseudo-momenta π is assigned to each of the ϕ. The pseudo-Hamiltonian, of the new system is written as

$$H_p\{\pi(t), \phi(t)\} = \pi^2(t)/2 + S\{\phi(t)\} \tag{A.6}$$

The field variables evolve globally for a pseudo-time (or along a pseudo-path length) t under the Hamilton-Jacobi equations of motion derived from the pseudo-Hamiltonian

H_p.

$$d\phi_k(t)/dt = \partial H_p\{\pi(t), \phi(t)\}/\partial\pi_k(t) = \pi_k(t) \tag{A.7}$$

and

$$d\pi_k(t)/dt = -\partial H_p\{\pi(t), \phi(t)\}/\partial\phi_k(t) = -\partial S\{\phi(t)\}/\partial\phi_k(t) \tag{A.8}$$

The pseudo-partition function associated with the pseudo-Hamiltonian is $Z_p = \int D\pi \int D\phi e^{-\beta H_p\{\pi(t),\phi(t)\}}$. Since the integrand for each of the pseudo-momenta is Gaussian, the integration over these pseudo-momenta is easily performed to yield $Z_p = (2\pi\mu)^{(V/2)}Z$. The pseudo-partition function differs from the true partition function only by a multiplicative constant, thus the expectation values of the physical observables will have identical values for both the true and pseudo-system.

In order to perform the simulation, the integration in imaginary time τ in Eq. (3) is discretized into N_τ steps of size Δ_τ where $\beta \equiv N_\tau\Delta_\tau$. The action $S\{\phi\}$ is expressed in terms of the field variables $\phi_{i,j,n}$,

$$\begin{aligned} S\{\phi\} = \sum_{i,j,n} \quad & [\frac{1}{\Delta_\tau\epsilon_C}\{1 - \cos(\phi_{i,j,n+1} - \phi_{i,j,n})\} \\ & + \Delta_\tau\epsilon_J\{2 \quad - \cos(\phi_{i+1,j,n} - \phi_{i,j,n} - \psi_{i,i+1} \\ & \qquad\qquad - \cos(\phi_{i,j+1,n} - \phi_{i,j,n} - \psi_{j,j+1})\}] \,. \end{aligned} \tag{A.9}$$

The subscripts i, j and n are the labels for the x, y (spatial) and the τ (imaginary-time) dimensions, respectively.

Following Duane *et al.*[4], a Gaussian distribution for the pseudo-momenta $\pi_{i,j,n}(0)$ is generated, and then both the $\phi_{i,j,n}(t)$ and $\pi_{i,j,n}(t)$ evolve *globally* for a pseudo-time t under the Hamilton-Jacobi equations of motion

$$d\phi_{i,j,n}(t)/dt = \pi_{i,j,n}(t) \tag{A.10}$$

and

$$\begin{aligned} \frac{d\pi_{i,j,n}(t)}{dt} = & -\frac{1}{\Delta_\tau \epsilon_C}\{\sin(\phi_{i,j,n+1} - \phi_{i,j,n}) + \sin(\phi_{i,j,n-1} - \phi_{i,j,n})\} \\ & -\Delta_\tau \epsilon_J \quad \{\sin(\phi_{i+1,j,n} - \phi_{i,j,n} - \psi_{i,i+1}) \\ & \qquad + \sin(\phi_{i-1,j,n} - \phi_{i,j,n} - \psi_{i,i-1}) \\ & \qquad + \sin(\phi_{i,j+1,n} - \phi_{i,j,n} - \psi_{j,j+1}) \\ & \qquad + \sin(\phi_{i,j-1,n} - \phi_{i,j,n} - \psi_{j,j-1})\}. \end{aligned} \tag{A.11}$$

We approximate the solutions of Eqs. (5 and 6) by using the leapfrog algorithm[23].

We probed several possibilities for the choices of the fictitious time $t = N_t\Delta_t$, the number of pseudo-time steps N_t, and the size of the pseudo-time step Δ_t. Because of the errors associated with any numerical integration scheme, the pseudo-energy will begin to deviate from its initial value after some time. The resulting configuration at the end of the Hamilton-Jacobi evolution $\{\phi'_m\}$ is therefore accepted or rejected with the probability $minimum(1, e^{\delta H_p})$, where $\delta H_p \equiv H\{\phi'_m\} - H_p\{\phi_m\}$. Thus in the hybrid method [4] errors associated with the finite-size Δ_t are only of importance in that they change the acceptance rate of the Monte Carlo configurations, and hence limit the time scale over which a configuration can evolve microcannonically before it has a high probability of being rejected. The pseudo-time step Δ_t was chosen such that the deviation from energy conservation yielded a Monte-Carlo acceptance rate of approximately 95%. Within this constraint, for separate simulations, the number of pseudo-time steps N_t was varied such that the pseudo-time t spanned several orders of magnitude.

Appendix B

The Action Renormalization Procedure

We now present the procedure we used to derive the renormalized classical action we used to describe our quasiclassical JJA shown in Fig. 2.1. In this array we have two types of superconducting grains. For reasons presented in the main text, we want to treat the large grains as classical and the small ones quantum. To derive our renormalized classical action we need only consider a system consisting of a single small quantum grain whose two nearest neighbors are large classical grains.

The partition function for this three grain system is

$$Z = \frac{N_\tau}{2\pi\beta\epsilon_C}^{\frac{3N_\tau}{2}} \int_0^{2\pi} \cdots \int_0^{2\pi} \quad d\phi_1 d\phi_2^1 \cdots d\phi_2^n \cdots d\phi_2^{N_\tau} d\phi_3 \\ e^{-A(\phi_1,\phi_2^1,\cdots,\phi_2^n\cdots\phi_2^{N_\tau},\phi_3)}, \tag{B.1}$$

where 1 and 3 denote the classical grains and 2 the quantum grains. The corresponding action is

$$A(\phi_1,\phi_2^1,\cdots,\phi_2^n\cdots\phi_2^{N_\tau},\phi_3) = \sum_{n=1}^{N_\tau} \quad \Delta_\tau\epsilon_J[\{1-\cos(\phi_3-\phi_2^n)\} \\ +\{1-\cos(\phi_2^n-\phi_1)\} \\ +\frac{1}{\Delta_\tau\epsilon_C}\{1-\cos(\phi_2^{n+1}-\phi_2^n)\}]. \tag{B.2}$$

In order to integrate out the the degrees of freedom associated with the quantum grain we consider only a part of the action; that which contains all of the ϕ_2^n terms.

$$F_1(\phi_1,\phi_2^{n-1},\phi_2^n,\phi_2^{n+1},\phi_3) = \\ \frac{1}{\Delta_\tau\epsilon_C}[\{1-\cos(\phi_2^{n-1}-\phi_2^n)\}+\{1-\cos(\phi_2^n-\phi_2^{n+1})\}] \\ +\Delta_\tau\epsilon_J[\{1-\cos(\phi_3-\phi_2^n)\}+\{1-\cos(\phi_2^n-\phi_1)\}] \tag{B.3}$$

and the corresponding integral

$$F_2(\phi_1, \phi_2^{n-1}, \phi_2^{n+1}, \phi_3) \quad = \quad \frac{N_\tau}{2\pi\beta\epsilon_C}^{\frac{N_\tau}{2}} \int_0^{2\pi} d\phi_2^n e^{-F_1(\phi_1, \phi_2^{n-1}, \phi_2^n, \phi_2^{n+1}, \phi_3)} \tag{B.4}$$

The general form of Eq. 26 allows us two advantages to exploited. First, if N_τ is taken to be a power of 2, 2^m, then only $m+1$ integrations need to be performed to derive the renormalized classical action. Our, numerical task is therefore tractable Second, Although quite tedious the integration can be done analytically.

Taking N_τ to be a power of 2 allows us the following advantage. We first recognize that all of integrations of the F_1 integrand over ϕ_2^n where $n = 2, 4, 6, \cdots, N_\tau - 2$ are the same. These result in the function $F_2(\phi_1, \phi_2^{n-1}, \phi_2^{n+1}, \phi_3)$ of which we do not know the general function but we can certainly make a table of it. We now can perform integrations of the F_2 integrand over ϕ_2^n where $n = 3, 7, 11, \cdots, N_\tau - 3$ are the same. These result in a table of the function $F_3(\phi_1, \phi_2^{n-2}, \phi_2^{n+2}, \phi_3)$. Continuing this procedure until we have a table of some function $F_m(\phi_1, \phi_2^1, \phi_2^{N_\tau}, \phi_3)$ we need only to perform the final integration.

A tedious analytical integration can be performed as follows. We use the following substitution

$$e^{z\cos(\phi)} = \sum_{j=-\infty}^{\infty} I_j(z)\cos(k\phi) \tag{B.5}$$

and obtain

$$
\begin{aligned}
&H(\phi_1, \phi_2^{n-1}, \phi_2^{n+1}, \phi_3) = \\
&\quad \frac{N_\tau}{2\pi\beta\epsilon_C}^{\frac{N_\tau}{2}} e^{-\frac{2}{\Delta_\tau\epsilon_C}} e^{-2\Delta_\tau\epsilon_J} \sum_{j,k,l,m=-\infty}^{\infty} I_j(\frac{1}{\Delta_\tau\epsilon_C}) I_k(\frac{1}{\Delta_\tau\epsilon_C}) I_l(\Delta_\tau\epsilon_J) I_m(\Delta_\tau\epsilon_J) \\
&\quad \int_0^{2\pi} d\phi_2^n \cos(j(\phi_2^{n-1} - \phi_2^n)) \cos(k(\phi_2^n - \phi_2^{n+1})) \cos(l(\phi_3 - \phi_2^n)) \cos(m(\phi_2^n - \phi_1))
\end{aligned}
\tag{B.6}
$$

These Fourier integrals are all well defined.

Appendix C

Nambu Formalism and Eliashberg Equations

In the Nambu [16] formalism, a two-component electron field operator $\Psi_{\vec{k}}$ and its adjoint $\Psi^{\dagger}_{\vec{k}}$ are introduced:

$$\Psi_{\vec{k}} = \begin{pmatrix} c_{\vec{k},\uparrow} \\ c^{\dagger}_{-\vec{k},\downarrow} \end{pmatrix}, \ \Psi^{\dagger}_{\vec{k}} = \begin{pmatrix} c^{\dagger}_{\vec{k},\uparrow} & c_{-\vec{k},\downarrow} \end{pmatrix} \tag{C.1}$$

such that

$$\{\Psi_{\vec{k}}, \Psi^{\dagger}_{\vec{k}'}\} = \delta_{\vec{k},\vec{k}'}\mathbf{I}\,, \ \{\Psi_{\vec{k}}, \Psi_{\vec{k}'}\} = \{\Psi^{\dagger}_{\vec{k}}, \Psi^{\dagger}_{\vec{k}'}\} = 0\,, \tag{C.2}$$

where $\mathbf{I}$ is a 2×2 unit matrix.

Then the one-particle thermodynamic Green's function $\mathbf{G}(\vec{k},\tau)$ is defined by 2×2 matrix:

$$\begin{aligned}\mathbf{G}(\vec{k},\tau) &= -\left\langle T_\tau \Psi_{\vec{k}}(\tau)\Psi^\dagger_{\vec{k}}(0)\right\rangle \\ &= \begin{pmatrix} \langle T_\tau c_{\vec{k},\uparrow}(\tau)c^\dagger_{\vec{k},\uparrow}(0)\rangle & \langle T_\tau c_{\vec{k},\uparrow}(\tau)c_{-\vec{k},\downarrow}(0)\rangle \\ \langle T_\tau c^\dagger_{-\vec{k},\downarrow}(\tau)c^\dagger_{\vec{k},\uparrow}(0)\rangle & \langle T_\tau c^\dagger_{-\vec{k},\downarrow}(\tau)c_{-\vec{k},\downarrow}(0)\rangle \end{pmatrix},\end{aligned} \tag{C.3}$$

where T_τ represents time-ordered product. Here the diagonal parts $\mathbf{G}_{11}$ and $\mathbf{G}_{22}$ are the conventional Green's functions for spin-up electrons and spin-down holes respectively, while the off-diagonal parts $\mathbf{G}_{12}$ and $\mathbf{G}_{21}$ are the anomalous Green's functions which describe the pairing correlations. Note that pairing is assumed to be limited to time reversed electronic states $|\vec{k}\uparrow\rangle$ and $|-\vec{k}\downarrow\rangle$.

The advantage of the Nambu formalism is that one can use the familiar Feynman-Dyson rules for the perturbation theory. From the Dyson equation in Matsubara frequencies $\omega_n = (2n+1)\pi T$, we can express $\mathbf{G}(\vec{k},i\omega_n)$ with a 2×2 matrix self-energy $\mathbf{\Sigma}(\vec{k},i\omega_n)$ as

$$\mathbf{G}^{-1}(\vec{k},i\omega_n) = i\omega_n\mathbf{I} - \epsilon_{\vec{k}}\boldsymbol{\tau}_3 - \mathbf{\Sigma}(\vec{k},i\omega_n)\,, \tag{C.4}$$

where $\boldsymbol{\tau_1}$ and $\boldsymbol{\tau_3}$ are Pauli matrices. Meanwhile the most general form for $\mathbf{\Sigma}(\vec{k}, i\omega_n)$ may be given by

$$\mathbf{\Sigma}(\vec{k}, i\omega_n) = [1 - Z(\vec{k}, i\omega_n)]i\omega_n \mathbf{I} + \phi(\vec{k}, i\omega_n)\boldsymbol{\tau}_1 + \phi'(\vec{k}, i\omega_n)\boldsymbol{\tau}_1 + \chi(\vec{k}, i\omega_n)\boldsymbol{\tau}_3 \,. \quad \text{(C.5)}$$

We are free to choose phases so that $\phi' = 0$. Rescaling the energy of electrons as $\epsilon_{\vec{k}} + \chi(\vec{k}, i\omega_n) \to \epsilon_{\vec{k}}$, $\mathbf{\Sigma}(\vec{k}, i\omega_n)$ has the form

$$\mathbf{\Sigma}(\vec{k}, i\omega_n) = [1 - Z(\vec{k}, i\omega_n)]i\omega_n \mathbf{I} + \phi(\vec{k}, i\omega_n)\boldsymbol{\tau}_1 \,. \quad \text{(C.6)}$$

Therefore the canonical form of $\mathbf{G}(\vec{k}, i\omega_n)$ is obtained by combining Eq. (C.6) with Eq. (C.4):

$$\begin{aligned} \mathbf{G}(\vec{k}, i\omega_n) &= [i\omega_n Z(\vec{k}, i\omega_n)\mathbf{I} - \epsilon_{\vec{k}}\boldsymbol{\tau}_3 - \phi(\vec{k}, i\omega_n)\boldsymbol{\tau}_1]^{-1} \\ &= -\frac{i\omega_n Z(\vec{k}, i\omega_n)\mathbf{I} + \epsilon_{\vec{k}}\boldsymbol{\tau}_3 + \phi(\vec{k}, i\omega_n)\boldsymbol{\tau}_1}{\omega_n^2 Z^2(\vec{k}, i\omega_n) + \epsilon_{\vec{k}}^2 + \phi^2(\vec{k}, i\omega_n)} \,. \end{aligned} \quad \text{(C.7)}$$

The Green's function in the superconducting state can be determined by applying the Migdal [44] method for the normal state with the Nambu formalism. Migdal showed that the vertex correction of the electron-phonon interaction is of order $\omega_D/E_F \sim \sqrt{m/M}$ where ω_D/E_F is the ratio of the Debye energy to the Fermi energy and m/M is the electron-ion mass ratio. Thus the self-energy due to the electron-phonon interaction can be evaluated in the Migdal limit from the diagram in Fig. C.1, and this leads to the self-consistent Eliashberg [15] equations.

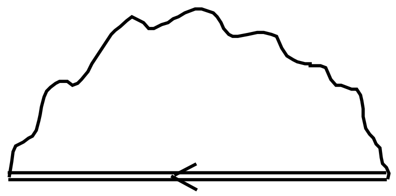

Figure C.1: *Electron self-energy diagram to lowest order in electron-phonon interaction.*

The self-energy $\mathbf{\Sigma}(\vec{k}, i\omega_n)$ corresponding to the diagram in Fig. C.1 is given by

$$\mathbf{\Sigma}(\vec{k}, i\omega_n) = -T \sum_{m=-\infty}^{\infty} \int \frac{d^3\vec{k}'}{(2\pi)^3} \alpha^2(\vec{k}, \vec{k}') D(\vec{k} - \vec{k}', i\omega_n - i\omega_m) \boldsymbol{\tau}_3 \mathbf{G}(\vec{k}', i\omega_m) \boldsymbol{\tau}_3 \,, \quad \text{(C.8)}$$

where α is the electron-phonon coupling constant averaged over polarization directions of the phonons and $D(\vec{k}, i\omega_n)$ is the phonon Green's function given by

$$D(\vec{k}, i\omega_n) = \int d\omega' \frac{B(\vec{k}, \omega')}{i\omega_n - \omega'} \quad \text{(C.9)}$$

with the spectral function $B(\vec{k}, \omega')$ for phonon. Since we are interested in the phase space where the energy transfer is of order ω_D and the momentum transfer is of order k_F, the momentum integration can be evaluated about the Fermi surface and $\mathbf{\Sigma}(\vec{k}, i\omega_n)$ is approximated as a function of only frequency. For an isotropic system, the self-energy $\mathbf{\Sigma}(i\omega_n)$ is determined by averaging $\mathbf{\Sigma}(\vec{k}, i\omega_n)$ over the Fermi surface.

Then we have

$$\mathbf{\Sigma}(i\omega_n) = \frac{T}{N_0} \sum_{m=-\infty}^{\infty} \lambda(i\omega_n - i\omega_m)\boldsymbol{\tau}_3 \mathbf{G}(i\omega_m)\boldsymbol{\tau}_3\,, \tag{C.10}$$

where N_0 is the density of states at the Fermi energy and the λ-function is defined by

$$\lambda(i\omega_n) = -\int_{-\infty}^{\infty} d\omega' \frac{\alpha^2 F(\omega')}{i\omega_n - \omega'} \tag{C.11}$$

with the electron-phonon spectrum function $\alpha^2 F(\omega)$. Also $\mathbf{G}(i\omega_m)$ is evaluated with Eq. (C.7):

$$\begin{aligned} \mathbf{G}(i\omega_m) &= N_0 \int_{-\infty}^{\infty} d\epsilon_k \mathbf{G}(k, i\omega_m) \\ &= -\pi N_0 \frac{i\omega_m Z(i\omega_m)\mathbf{I} + \phi(i\omega_m)\boldsymbol{\tau}_1}{\sqrt{\omega_m^2 Z^2(i\omega_m) + \phi^2(i\omega_m)}}\,. \end{aligned} \tag{C.12}$$

By introducing the gap function

$$\Delta(i\omega_m) = \frac{\phi(i\omega_m)}{Z(i\omega_m)} \tag{C.13}$$

and comparing Eq. (C.10) and Eq. (C.12) with Eq. (C.6), we get the self-consistent Eliashberg equations:

$$Z(i\omega_n) = 1 + \frac{\pi T}{\omega_n} \sum_{m=-\infty}^{\infty} \lambda(i\omega_n - i\omega_m) \frac{\omega_m}{\sqrt{\omega_m^2 + \Delta^2(i\omega_m)}} \tag{C.14}$$

and

$$\Delta(i\omega_n)Z(i\omega_n) = \pi T \sum_{m=-\infty}^{\infty} \lambda(i\omega_n - i\omega_m)\frac{\Delta(i\omega_m)}{\sqrt{\omega_m^2 + \Delta^2(i\omega_m)}}\,. \tag{C.15}$$

The Coulomb interactions can be also included by introducing the Coulomb pseudo-potential μ^* ,which renormalizes the screened Coulomb interaction, such that Eq. (C.15) may be modified as

$$\Delta(i\omega_n)Z(i\omega_n) = \pi T \sum_{m=-\infty}^{\infty} [\lambda(i\omega_n - i\omega_m) - \mu^*]\frac{\Delta(i\omega_m)}{\sqrt{\omega_m^2 + \Delta^2(i\omega_m)}}\,. \tag{C.16}$$

Appendix D

Derivation of the QMC Algorithm

We derive the QMC Algorithm for the symmetric Anderson model [38] in the superconducting state, applying the Hirsch-Fye method [60] in the Nambu [16] formalism. The Hamiltonian may be written as

$$H = H_0 + H_1 \,, \tag{D.1}$$

where

$$H_0 = \sum_{\vec{k},s} \epsilon_{\vec{k}} c^\dagger_{\vec{k},s} c_{\vec{k},s} + \sum_{\vec{k},s} \Delta_{\vec{k}} (c_{\vec{k},\uparrow} c_{-\vec{k},\downarrow} + c^\dagger_{-\vec{k},\downarrow} c^\dagger_{\vec{k},\uparrow}) + \sum_{\vec{k},s} V (c^\dagger_{\vec{k},s} d_s + d^\dagger_s c_{\vec{k},s}) + \epsilon_d (n_{d,\uparrow} + n_{d,\downarrow}) \tag{D.2}$$

and

$$H_1 = U(n_{d,\uparrow} - \frac{1}{2})(n_{d,\downarrow} - \frac{1}{2})\,. \tag{D.3}$$

In a discrete path-integral formulation the partition function $\mathcal{Z}$ is

$$\mathcal{Z} = \mathrm{Tr}\, e^{-\beta H} = \mathrm{Tr} \prod_{l=1}^{L} e^{-\Delta\tau H} \approx \mathrm{Tr} \prod_{l=1}^{L} e^{-\Delta\tau H_0} e^{-\Delta\tau H_1} + \mathcal{O}(\Delta\tau^2) \tag{D.4}$$

with $\beta = 1/T = L\Delta\tau$. One can decouple the interaction term H_1 by introducing auxiliary time-dependent field (Hubbard-Stratonovich field) σ_l:

$$e^{-\Delta\tau H_1} = \frac{1}{2} e^{-\frac{\Delta\tau U}{4}} \sum_{\sigma_l = \pm 1} e^{\alpha\sigma_l(n_{d,\uparrow} - n_{d,\downarrow})} \tag{D.5}$$

with $\cosh\alpha = e^{\frac{\Delta\tau U}{2}}$. Then, using the Nambu [16] formalism, the partition function may be rewritten as

$$\mathcal{Z} = \sum_{\{\sigma_l\}} \mathrm{Tr} \prod_{l=1}^{L} e^{-\Delta\tau H_l'} \tag{D.6}$$

with

$$\begin{aligned} H_l' \;=\; & \sum_{\vec{k}} \epsilon_{\vec{k}} (\Psi_{\vec{k}}^\dagger \boldsymbol{\tau}_3 \Psi_{\vec{k}}) + \sum_{\vec{k}} \Delta_{\vec{k}} \Psi_{\vec{k}}^\dagger \boldsymbol{\tau}_1 \Psi_{\vec{k}} + V \sum_{\vec{k}} (\Psi_d^\dagger \boldsymbol{\tau}_3 \Psi_{\vec{k}} + \Psi_{\vec{k}}^\dagger \boldsymbol{\tau}_3 \Psi_d) \\ & + \Psi_d^\dagger (\epsilon_d \boldsymbol{\tau}_3 - \frac{\alpha}{\Delta\tau} \sigma_l \mathbf{I}) \Psi_d + \frac{\alpha}{\Delta\tau} \sigma_l\,, \end{aligned} \tag{D.7}$$

where we ignored irrelevant constant terms.

A functional integral representation is obtained using coherent states $|\eta\rangle$ and $|\xi\rangle$ with corresponding Grassman [61] variables $\{\eta_{\vec{k}},\, \eta^\dagger,\, \xi,\, \xi^\dagger\}$:

$$\Psi_{\vec{k}}|\eta\rangle = \eta_{\vec{k}}|\eta\rangle\,,\ \ \langle\eta|\Psi^\dagger_{\vec{k}} = \langle\eta|\eta^\dagger_{\vec{k}}\,,\ \ \langle\xi|\Psi^\dagger_d = \langle\xi|\xi^\dagger \text{ and } \Psi_d|\xi\rangle = \xi|\xi\rangle \tag{D.8}$$

such that

$$\begin{aligned}
\mathcal{Z} &= \sum_{\{\sigma_l\}} e^{-\alpha\sum_{l=1}^{L}\sigma_l} \iint \prod_{l=1}^{L}\prod_{\vec{k}} d\eta^\dagger_{\vec{k},l}\, d\eta_{\vec{k},l}\, d\xi^\dagger_l\, d\xi_l \\
&\times \exp\left\{-\sum_{l,l'=1}^{L}\sum_{\vec{k}}\left[\eta^\dagger_{\vec{k},l}\left(\mathbf{G}^{-1}_{\vec{k}}\right)_{l,l'}\eta_{\vec{k},l'} + \Delta\tau V\left(\eta^\dagger_{\vec{k},l}\,(\boldsymbol{\tau}_3\xi_l) + (\boldsymbol{\tau}_3\xi_l)^\dagger\eta_{\vec{k},l}\right)\right]\right\} \\
&\times \exp\left\{-\sum_{l=1}^{L}\left[\xi^\dagger_l(\xi_{\vec{k},l} - \xi_{\vec{k},l-1}) + \Delta\tau\xi^\dagger_l(\epsilon_d\boldsymbol{\tau}_3 - \frac{\alpha}{\Delta\tau}\sigma_l\mathbf{I})\eta_{\vec{k},l-1}\right]\right\}
\end{aligned} \tag{D.9}$$

with the Green's function of the host $\mathbf{G}_{\vec{k}}$

$$\left(\mathbf{G}^{-1}_{\vec{k}}\right)_{l,l'} = \delta_{l.l'}\mathbf{I} - \delta_{l-1,l'}\left(\mathbf{I} - \Delta\tau\epsilon_{\vec{k}}\boldsymbol{\tau}_3 + \Delta_{\vec{k}}\boldsymbol{\tau}_1\right) \tag{D.10}$$

which is the direct product of $L\times L$ matrix and 2×2 matrices. Using the following identity

$$\int\prod_{i=1} d\eta^*_i\, d\eta_i e^{\sum_{i,j}\left(-\eta^*_i\mathbf{M}_{ij}\eta_j + \zeta^*_i\eta_i + \zeta_i\eta^*_i\right)} = [\det\mathbf{M}]e^{\sum_{ij}\zeta^*_i\mathbf{M}^{-1}_{ij}\zeta_j}\,, \tag{D.11}$$

where $\mathbf{M}$ is any Hermitian matrix and $\{\eta_i,\, \eta_i^*,\, \zeta_i,\, \zeta_i^*\}$ are Grassmann variables, we may integrate out the fermion degrees of freedom

$$\mathcal{Z} = \sum_{\{\sigma_l\}} e^{-\alpha \sum_{l=1}^{L} \sigma_l} \prod_{\vec{k}} \det\left(\mathbf{G}_{\vec{k}}^{-1}\right) \int \prod_{l=1}^{L} d\xi_l^\dagger \, d\xi_l e^{-\sum_{l,l'=1}^{L} \xi_l^\dagger \left(\mathbf{G}_d^{-1}\right)_{l,l'} \xi_{l'}} \tag{D.12}$$

with the Green's function of the impurity $\mathbf{G}_d$

$$\left(\mathbf{G}_d^{-1}\right)_{l,l'} = \delta_{l.l'}\mathbf{I} - \delta_{l-1,l'}\left(\mathbf{I} - \Delta\tau\epsilon_d\boldsymbol{\tau}_3 + \alpha\sigma_l\mathbf{I}\right) - \Delta\tau^2 V^2\left(\boldsymbol{\tau}_3\mathbf{G}_{\vec{k}}\boldsymbol{\tau}_3\right)_{l,l'}. \tag{D.13}$$

Therefore, ignoring the overall constants, the partition function may be expressed in terms of Hubbard-Stratonovich field $\{\sigma_l\}$ by which the fermions are scattered at the impurity site:

$$\mathcal{Z} = \sum_{\{\sigma_l\}} e^{-\alpha \sum_{l=1}^{L} \sigma_l} \det \mathbf{G}_d^{-1}\left(\{\sigma_l\}\right). \tag{D.14}$$

Denoting a potential $\mathbf{V}_l$ acting only at the impurity site as

$$\mathbf{V}_l = -\Delta\tau\left(\epsilon_d\boldsymbol{\tau}_3 - \frac{\alpha}{\Delta\tau}\sigma_l\mathbf{I}\right), \tag{D.15}$$

Green's functions for two different potentials $\mathbf{V}_l$ and $\mathbf{V'}_l$ are related each other by the following equation

$$(\mathbf{G'}_d)_{l,l'} = (\mathbf{G}_d)_{l,l'} + [(\mathbf{G}_d)_{l,l''} - \delta_{l,l''}](e^{\mathbf{V'}_{l''} - \mathbf{V}_{l''}} - \mathbf{I})(\mathbf{G'}_d)_{l'',l}. \tag{D.16}$$

The ratio of $\det \mathbf{G}_d^{-1}(\{\sigma_l\})$ for changing field σ_l to σ_l' is given by

$$\frac{\det \mathbf{G}_d^{-1}(\{\sigma_l'\})}{\det \mathbf{G}_d^{-1}(\{\sigma_l\})} = \det\left\{\mathbf{I} - [(\mathbf{G}_d)_{l,l} - \mathbf{I}](e^{\mathbf{V}'_l - \mathbf{V}_l} - \mathbf{I})\right\} . \tag{D.17}$$

Thus the relative weight in the partition function for two different configurations at time slice l is

$$R = e^{-\alpha(\sigma_l' - \sigma_l)} \det\left\{\mathbf{I} - [(\mathbf{G}_d)_{l,l} - \mathbf{I}](e^{\mathbf{V}'_l - \mathbf{V}_l} - \mathbf{I})\right\} . \tag{D.18}$$

When this change is accepted, $\mathbf{G}_d$ is updated following the relation

$$\begin{aligned}(\mathbf{G}_d')_{l,l'} &= (\mathbf{G}_d)_{l,l'} + [(\mathbf{G}_d)_{l,l''} - \delta_{l,l''}](e^{\mathbf{V}'_{l''} - \mathbf{V}_{l''}} - \mathbf{I}) \\ &\quad \times \left\{\mathbf{I} - [(\mathbf{G}_d)_{l'',l''} - \mathbf{I}](e^{\mathbf{V}'_{l''} - \mathbf{V}_{l''}} - \mathbf{I})\right\}^{-1} (\mathbf{G}_d)_{l'',l'} . \end{aligned} \tag{D.19}$$

Appendix E

Maximum Entropy Method (MEM)

Here we summarize very briefly the basic idea of the MEM based on the review by Jarrell and Gubernatis [13]. Details of the MEM should be referred to the reference [13] where the related references are also found.

We want to extract the dynamical spectral functions $A(\omega)$ from the data (one- and two- particle Green's functions) $G(\tau)$ generated by the QMC simulations. For a one-particle fermion Green's function $G(\tau)$, for instance, the equation is given by

$$G(\tau) = \int_{-\infty}^{\infty} d\omega \frac{e^{-\tau\omega}}{1 + e^{-\beta\omega}} A(\omega) \,. \tag{E.1}$$

Then the retarded Green's function $G(\omega)$ is associated with $A(\omega)$ by

$$G(\omega) = \int_{-\infty}^{\infty} d\omega' \frac{A(\omega')}{\omega - \omega' + i\eta} \tag{E.2}$$

with $0 < \eta \ll 1$, and

$$A(\omega) = -\frac{1}{\pi}\mathrm{Im}G(\omega)\,. \tag{E.3}$$

Formally the extraction in Eq. (E.1) requires the inverse integral transform between the data $G(\tau)$ and the spectral function $A(\omega)$ with the given form of the kernel $K(\tau, \omega)$:

$$K(\tau, \omega) = \frac{e^{-\tau\omega}}{1 + e^{-\beta\omega}}\,. \tag{E.4}$$

This transform is much like the inverse Laplace transform which is a well-known ill-posed problem. Not only this problem but the necessarily noisy and incomplete QMC data make such inversions difficult, and an infinite number of solutions exists. The MEM seeks the most probable spectral function from these solutions with the methods of Bayesian statistical inference. Note that, since the spectral function here is non-negative and normalizable, it can be regarded as a probability function in the MEM.

Based upon Bayesian statistics, we maximize the *posterior probability* $\Pr[A|G]$ given by

$$\Pr[A|G] \propto \Pr[G|A] \Pr[A] , \tag{E.5}$$

where $\Pr[a]$ is the probability of a and $\Pr[a|b]$ is the conditional probability of a given b. $P[G|A]$ is called the *likelihood function* given by $P[G|A] \propto e^{-\frac{1}{2}\chi^2}$ with

$$\chi^2 = \sum_i \left(\frac{G_i - K_{ij} A_j}{\sigma_i} \right)^2 , \tag{E.6}$$

where $G_i = G(\tau_i)$, $K_{ij} = K(\tau_i, \omega_j)$ and $A_i = A(\omega_i)\Delta\omega_i$ with discrete values of τ and ω; σ_i is the standard errors; and here every quantities are defined in the rotated coordinate where the covariance of the data is diagonal. The *prior probability*, $\Pr[A] \propto e^{\alpha S}$, is associated with the parameter α and the entropy S defined by

$$S = \sum_i [A_i - m_i - A_i \ln(A_i/m_i)] , \tag{E.7}$$

where m is called *default model* and it gives the maximum entropy when there is no data.

Thus we have $\Pr[A|G] \propto e^Q$ with

$$Q = \alpha S - \frac{1}{2}\chi^2 , \tag{E.8}$$

and we maximize Q with respect to $A(\omega)$. Since this result will depend on α, we choose as our solution $A(\omega)$ defined by

$$A(\omega) = \int d\alpha \hat{A}_\alpha(\omega) \Pr[\alpha|G], \tag{E.9}$$

where $\hat{A}_\alpha(\omega)$ is the value of $A(\omega)$ for fixed α at which Q is maximum and $\Pr[\alpha|G]$ is the posterior distribution of α given the data $G(\tau)$. $\Pr[\alpha|G]$ may be also obtained from Bayesian statistics, and hence we find the *most probable* spectral function (or *image*) from the QMC data $G(\tau)$.

Bibliography

[1] See, for example, J. R. Schrieffer, *Theory of Superconductivity* (Benjamin/Cummings, New York, 1964).

[2] See, for example, D. J. Scalapino, in *Superconductivity*, edited by R. D. Parks (Dekker, New York, 1969), Vol. 1, Chap. 10.

[3] S. Duane, Nucl. Phys. B **257**, 652 (1985); S. Duane and J. B. Kogut, Nucl. Phys. B **275**, 398 (1986).

[4] S. Duane, A. D. Kennedy, B. J. Pendleton, and D. Roweth, Phys. Lett. B **195**, 216 (1986).

[5] J. E. Gubernatis, D. K. Campbell and X. Wang, in *Computational Approaches in Condensed Matter Physics*, (edited by S. Miyashita, M. Imada, and H. Takayama Springer-Verlag, Berlin, 1992), pg. 162; X. Wang, D. K. Campbell, and J. E. Gubernatis, to be published.

[6] E. Simanek, Solid State Commun. **31**, 419 (1979).

[7] J. V. Jose Phys. Rev. B **29**, 2836 (1984).

[8] L. Jacobs, J. V. Jose and M. A. Novotny, Phys. Rev. Lett. **53**, 2177 (1984).

[9] L. Jacobs, J. V. Jose, M. A. Novotny and A. Goldman, Europhys. Lett. **3**, 1295 (1987).

[10] L. Jacobs, J. V. Jose, M. A. Novotny and A. Goldman, Phys. Rev. B **38**, 4562 (1988).

[11] See, for example, A. C. Hewson, *The Kondo Problem to Heavy Fermions* (Cambridge University Press, 1993).

[12] M. Jarrell, D. S. Sivia, and B. Patton, Phys. Rev. B **42**, 4804 (1990).

[13] For a review of the Maximum Entropy Method of analytic continuation, see M. Jarrell and J. E. Gubernatis, Phys. Rep. **269**, 133 (1996).

[14] F. Marsiglio, M. Schossmann, and J. P. Carbotte, Phys. Rev. B **37**, 4965 (1988).

[15] G. M. Eliashberg, Zh. Eksp. Teor. Fiz. **38**, 966 (1960) [Sov. Phys. JETP **11**, 696 (1960)].

[16] Y. Nambu, Phys. Rev. **117**, 648 (1960).

[17] P. W. Anderson, in *Lectures on the Many Body Problem*, (edited by E. R. Caianello, Academic Press, New York, 1964) Vol. 2, p.127.

[18] B. Abeles, Phys. Rev. B **15**, 2828 (1977).

[19] E. Granato, J. M. Kosterlitz, J. Lee, and M. P. Nightingale, Phys. Rev. Lett. **66**, 1090 (1991); J. Lee, J. M. Kosterlitz, and E. Granato, Phys. Rev. B **43**, 11531 (1991); J. Lee, E. Granato, and J. M. Kosterlitz, Phys. Rev. B **44**, 4819 (1991).

[20] J. R. Lee, Phys. Rev. B, submitted.

[21] A. Kampf and G. Schön, Phys. Rev. B **36**, 3651 (1987).

[22] J. M. Houlrik and M. A. Novotny, Physica C **153-155**, 312 (1988).

[23] W. F. Ames, *Numerical Methods for Partial Differential Equations*, 2nd ed. (Academic Press, New York, 1964).

[24] Note the misprint in Eq. (4.3) in reference L. Jacobs, J. V. José, M. A. Novotny and A. Goldman, Phys. Rev. B **38**, 4562 (1988).

[25] D. J. Scalapino, S. R. White and S. Zhang, Phys. Rev. B **47**, 7995 (1993).

[26] M. Sarachik, E. Corenzwit, and L. D. Longinotti, Phys. Rev. **135**, A1041 (1964).

[27] A. M. Clogston, B. T. Matthias, m. Peter, H. J. Williams, E. Corenzwit, and R. C. Sherwood, Phys. Rev. **125**, 541 (1962).

[28] J. Kondo, Prog. Theor. Phys. **32**, 37 (1964).

[29] K. Samwer, and K. Winzer, Z. Phys. B **25**, 269 (1976).

[30] See, for example, J. Kondo, in *Solid State Physics* **23**, edited by F. Seitz, D. Turnbull, and H. Ehrenreich (Academic Press, New York, 1969).

[31] Y. Nagaoka, Phys. Rev. A **138**, 1112 (1965).

[32] H. Suhl, Phys. Rev. **138**, A515 (1965).

[33] D. R. Hamann, Phys. Rev. **158**, 570 (1967).

[34] K. Yosida, Phys. Rev. **147**, 223 (1966).

[35] P. Nozieres, J. Low Temp. Phys. **17**, 31 (1974).

[36] K. G. Wilson, Rev. Mod. Phys. **47**, 773 (1975).

[37] N. Andrei, and J. H. Lowenstein, Phys. Rev. Lett. **46**, 356 (1981).

[38] P. W. Anderson, Phys. Rev. **124**, 41 (1961).

[39] J. R. Schrieffer, and P. A. Wolff, Phys. Rev. **149**, 491 (1966).

[40] H. R. Krishna-murthy, J. W. Wilkins, and K. G. Wilson, Phys. Rev. B **21**, 1003 & 1044 (1980).

[41] J. Bardeen, L. N. Cooper, and J. R. Schrieffer, Phys. Rev. **108**, 1175 (1957).

[42] I. Giaever, Phys. Rev. Lett. **5**, 147, 464 (1960).

[43] J. M. Rowell, and L. Kopf, Phys. Rev. **137**, 907 (1965).

[44] A. B. Migdal, Zh. Eksp. Teor. Fiz. **34**, 1438 (1958) [Sov. Phys. JETP **7**, 996 (1958)].

[45] C. S. Owen and D. J. Scalapino, Physica **55**, 691 (1971).

[46] See, for example, D. M. Ginssberg, Phys. Rev. B **13**, 2895 (1976), and references therein.

[47] L. Dumoulin, E. Guyon, and P. Nedellec, Phys. Rev. Lett. **34**, 264 (1975); Phys. Rev. B **16**, 1086 (1977).

[48] A. A. Abrikosov and L. Gorkov, Zh. Eksp. Teor. Fiz. **39**, 1781 (1960) [Sov. Phys. JETP **12**, 1243 (1961)].

[49] H. Shiba, Prog. Theor. Phys. **40**, 435 (1968).

[50] J. Zittartz, A. Bringer, and E. Müller-Hartmann, Solid State Commun. **10**, 513 (1971).

[51] See, E. Müller-Hartmann, *Magnetism*, Ed. H. Suhl, (Academic, 1973), Vol. 5, p. 353.

[52] T. Matsuura, Prog. Theor. Phys. **57**, 1823 (1976).

[53] A. B. Kaiser, Phys. Rev. B **22**, 2323 (1980); L. S. Borkowski and P. J. Hirschfeld, Phys. Rev. B **46**, 9274 (1992), *etc.*

[54] J. Simonin and R. Allub, Phys. Rev. Lett. **74**, 466 (1995).

[55] K. Satori, H. Shiba, O. Sakai, and Y. Shimizu, J. Phys. Soc. Jpn. **61**, 3239 (1992); O. Sakai, Y. Shimizu, H. Shiba, and K. Satori, J. Phys. Soc. Jpn. **62**, 3181 (1993).

[56] J. K. Freericks, private communication.

[57] G. Baym and D. Mermin, J. Math. Phys. **2**, 232 (1961).

[58] M. Jarrell, Phys. Rev. B, Rapid Comm. **41**, 4815 (1990).

[59] M. Jarrell, Phys. Rev. Lett. **61**, 2612 (1988).

[60] J. E. Hirsch and R. M. Fye, Phys. Rev. Lett. **56**, 2521 (1986).

[61] See, for example, J. W. Negele and H. Orland, *Quantum Many-Particle Systems* (Addison-Wesley, New York, 1988).